Applied Computational Electromagnetics Society

# Journal

October 2011 Vol. 26 No. 10

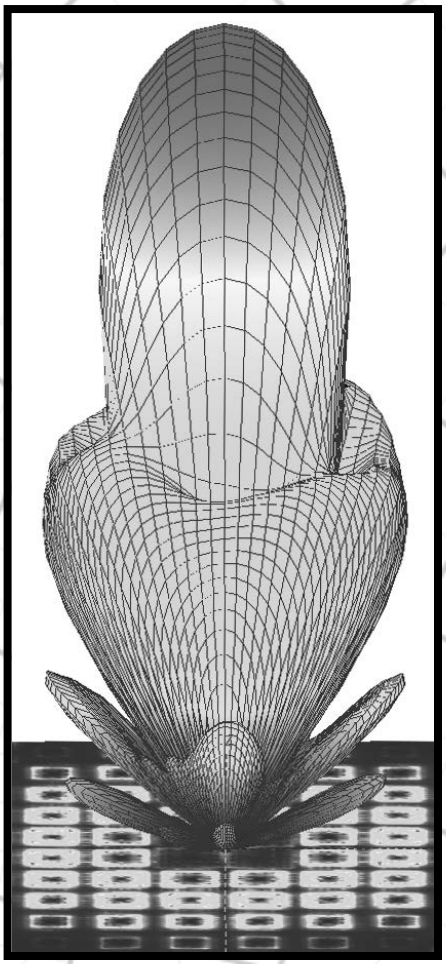

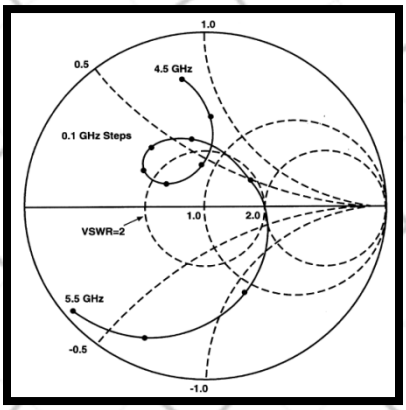


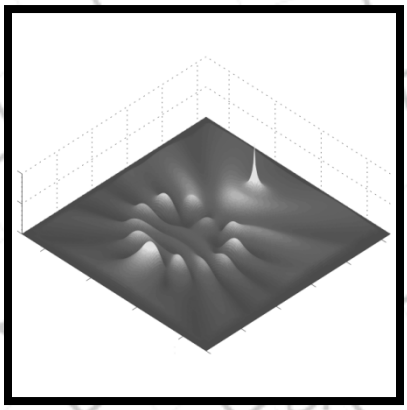

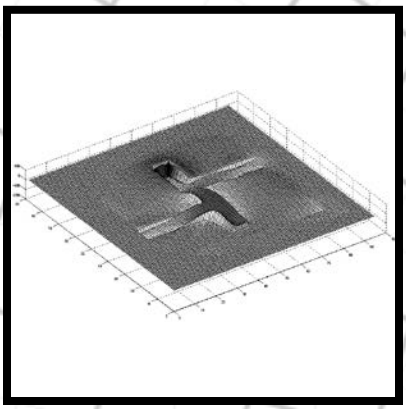

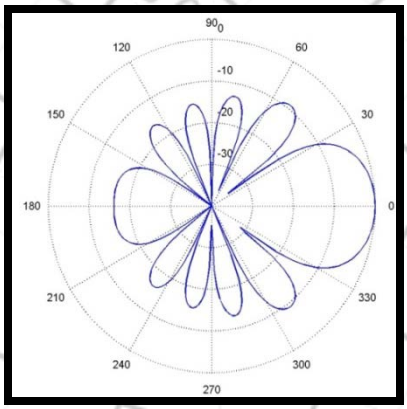


ISSN 1054-4887

**GENERAL PURPOSE AND SCOPE:** The Applied Computational Electromagnetics Society ***(ACES)*** Journal hereinafter known as the ***ACES Journal*** is devoted to the exchange of information in computational electromagnetics, to the advancement of the state-of-the art, and the promotion of related technical activities. The primary objective of the information exchange is to inform the scientific community on the developments of new computational electromagnetics tools and their use in electrical engineering, physics, or related areas. The technical activities promoted by this publication include code validation, performance analysis, and input/output standardization; code or technique optimization and error minimization; innovations in solution technique or in data input/output; identification of new applications for electromagnetics modeling codes and techniques; integration of computational electromagnetics techniques with new computer architectures; and correlation of computational parameters with physical mechanisms.

**SUBMISSIONS:** The ***ACES Journal*** welcomes original, previously unpublished papers, relating to applied computational electromagnetics. Typical papers will represent the computational electromagnetics aspects of research in electrical engineering, physics, or related disciplines. However, papers which represent research in applied computational electromagnetics itself are equally acceptable.

Manuscripts are to be submitted through the upload system of ***ACES*** web site http://aces.ee.olemiss.edu See "Information for Authors" on inside of back cover and at ***ACES*** web site. For additional information contact the Editor-in-Chief:


**Dr. Atef Elsherbeni**
Department of Electrical Engineering
The University of Mississippi
University, MS 386377 USA
Phone: 662-915-5382
Email: atef@olemiss.edu


**SUBSCRIPTIONS:** All members of the Applied Computational Electromagnetics Society are entitled to access and download the ***ACES Journal*** any published journal article available at http://aces.ee.olemiss.edu. Printed issues of the ***ACES Journal*** are delivered to institutional members. Each author of published papers receives a printed issue of the ***ACES Journal*** in which the paper is published.

**Back issues**, when available, are $50 each. Subscription to ***ACES*** is through the web site. Orders for back issues of the ***ACES Journal*** and change of address requests should be sent directly to ***ACES*** office at:


Department of Electrical Engineering
The University of Mississippi
University, MS 386377 USA
Phone: 662-915-7231
Email: aglisson@olemiss.edu


Allow four weeks advance notice for change of address. Claims for missing issues will not be honored because of insufficient notice, or address change, or loss in the mail unless the ***ACES*** office is notified within 60 days for USA and Canadian subscribers, or 90 days for subscribers in other countries, from the last day of the month of publication. For information regarding reprints of individual papers or other materials, see "Information for Authors".

***LIABILITY.*** Neither ***ACES***, nor the ***ACES Journal*** editors, are responsible for any consequence of misinformation or claims, express or implied, in any published material in an ***ACES Journal*** issue. This also applies to advertising, for which only camera-ready copies are accepted. Authors are responsible for information contained in their papers. If any material submitted for publication includes material which has already been published elsewhere, it is the author's responsibility to obtain written permission to reproduce such material.

# APPLIED COMPUTATIONAL ELECTROMAGNETICS SOCIETY JOURNAL

October 2011
Vol. 26 No. 10
ISSN 1054-4887

**The ACES Journal is abstracted in INSPEC, in Engineering Index, DTIC, Science Citation Index Expanded, the Research Alert, and to Current Contents/Engineering, Computing & Technology.**

The illustrations on the front cover have been obtained from the research groups at the Department of Electrical Engineering, The University of Mississippi.

## OCTOBER 2011 REVIEWERS

**Ahmed Abdelrahman**
**Ercument Arvas**
**Ali Azarbar**
**Mohamed Bakr**
**Ahmed Boutejdar**
**William Coburn**
**Jorge Costa**
**Yiming Deng**
**Christophe Fumeaux**
**Julie Huffman**
**Shambhu Jha**
**Chenhui Jiang**
**Hai Jiang**
**Yasushi Kanai**
**Fadi Khalil**
**Gordon MacDonald**
**Ricardo Matias**
**Joseph Mautz**
**Ivor Morrow**
**Arash Nejadpak**
**Kurt Oughstun**
**Ali Ozmetin**
**Andrew Peterson**
**Qinjiang Rao**
**Randall Reeves**
**Alain Reineix**
**Vince Rodriguez**
**Harvey Schuman**
**Yuan Sun**
**Hossein Torkaman**
**Christopher Trueman**
**Karl Warnick**
**Taeyoung Yang**
**Pasi Yia-Oijala**
**John Young**

# THE APPLIED COMPUTATIONAL ELECTROMAGNETICS SOCIETY

## JOURNAL

Vol. 26 No. 10 October 2011


## TABLE OF CONTENTS

# Axisymmetric Electromagnetic Resonant Cavity Solution by a Meshless Local Petrov-Galerkin Method

**Ramon D. Soares[1], Renato C. Mesquita[2], and Fernando J. S. Moreira[1]**

[1] Department of Electronics Engineering
Federal University of Minas Gerais (UFMG), Belo Horizonte, MG 31270-901, Brazil
ramon_dornelas@yahoo.com.br, fernandomoreira@ufmg.br

[2] Department of Electrical Engineering
Federal University of Minas Gerais (UFMG), Belo Horizonte, MG 31270-901, Brazil
renato@ufmg.br

***Abstract*** ― This work describes a meshless approach to obtain resonant frequencies and field distributions in axisymmetric electromagnetic cavities. The meshless local Petrov-Galerkin is used with shape functions generated by moving least squares. Boundary conditions are imposed by a collocation method that does not require integrations. The proposed analysis has simple implementation and reduced computational effort. Results for TE and TM modes of cylindrical and spherical cavities are presented and compared with analytical solutions.

***Index Terms*** ― BOR (bodies of revolution), electromagnetic cavities, LBIE (local boundary integral equation), and MLPG (meshless local Petrov-Galerkin).

## I. INTRODUCTION

Meshless methods are a class of numerical methods able to solve problems governed by partial differential equations (PDE), as other methods vastly used by the computational electromagnetic (CEM) community like the finite element method (FEM) and the finite difference method (FDM). The FDM is usually employed to solve problems in time domain, generating the well-known finite difference time domain (FDTD) [1]. FEM, on the other hand, is generally used to solve electromagnetic problems in frequency domain. Both methods need a mesh (FEM) or a grid (FDTD) to attain a numerical solution.

A mesh generation with strict quality restrictions required by numerical methods is a very demanding task, especially for very complicated geometries and for three-dimensional (3D) problems. For this reason, alternative numerical techniques without meshes or grids are sought. In meshless methods, the numerical solution is obtained without setting up any kind of grid or mesh. From a computational perspective, FEM requires more time in its mesh setup, while meshless methods demand on its matrix computation due to the complexity of their shape function construction.

Meshless methods can be classified in two categories: methods based on strong forms and those based on weak formulations. In strong-form methods, the governing partial differential equations (PDEs) are directly discretized using simple collocation techniques. These methods are computationally efficient and have simple implementation; but they are often unstable, not robust, and inaccurate [2]. Meshless methods based on collocation are generally implemented using smoothed particle hydrodynamics for electromagnetics (SPEM) formulations [3] or radial basis functions [4, 5, and 6].

In order to use methods based on weak formulations, it is necessary to construct a weak equation, which is obtained by applying the residual method to the PDE [2]. Galerkin or Petrov-Galerkin methods can be used to discretize the weak equation, resulting in methods more

*Submitted On: May 31, 2011*
*Accepted On: October 16, 2011*

robust, stable, and with higher convergence rates than collocation techniques [2].

The element free Galerkin method (EFGM) is a global weak formulation, which has been successfully applied in the solution of wave scattering problems [7]. The main drawback of the EFGM is that it requires a background mesh to perform numerical integrations. Recently, meshless local Petrov-Galerkin (MLPG), which is a local weak-form method and does not use a mesh even for integration, has been used to solve wave propagation [8] and 3D static problems [9].

The present work extends the MLPG procedures presented in [8 and 9] to determine the resonant frequencies and field distributions inside axisymmetric cavities. Similar problems have been solved in [4 and 5] using meshless collocation methods. Our work adopts MLPG, which is a weak-form method that, in principle, has better precision and numerical stability when compared with collocation methods [2].

## II. PROBLEM FORMULATION

The vectorial Helmholtz equation for a source-free region containing a material characterized by its relative permittivity $\epsilon_r$ and permeability $\mu_r$ is given by [10]

$$\nabla \times \left(\frac{1}{\epsilon_r} \nabla \times \vec{H}\right) - {k_0}^2 \mu_r \vec{H} = 0, \qquad (1)$$

where $k_0^2 = \omega^2 \epsilon_0 \mu_0$ and $k_0$ is the free-space wavenumber.

We first make the assumption that the field distribution is also axisymmetric, i.e., the magnetic field in (1) has only the $\phi$-component and varies only in $\rho$ and $z$ directions ($\vec{H} = H_\phi(\rho, z)\hat{\phi}$). This assumption is applied in (1) and results in a TM scalar formulation:

$$\frac{\partial}{\partial \rho}\left[\frac{1}{\rho\epsilon_r}\frac{\partial(\rho H_\phi)}{\partial \rho}\right] + \frac{\partial}{\partial z}\left[\frac{1}{\rho\epsilon_r}\frac{\partial(\rho H_\phi)}{\partial z}\right] + k_0^2 \mu_r H_\phi = 0. \qquad (2)$$

The weak form is then obtained by the weighted residual method, multiplying (2) by a test function $\psi(\rho, z)$ and integrating the result over the domain $\Omega$:

$$\iint_\Omega \frac{\partial}{\partial \rho}\left[\frac{1}{\rho\epsilon_r}\frac{\partial(\rho H_\phi)}{\partial \rho}\right]\psi + \frac{\partial}{\partial z}\left[\frac{1}{\rho\epsilon_r}\frac{\partial(\rho H_\phi)}{\partial z}\right]\psi dA + k_0^2 \iint_\Omega \mu_r H_\phi \psi dA = 0. \qquad (3)$$

After some mathematical manipulations [10], the weak form for the TM solution is obtained:

$$\oint_{\partial\Omega} \frac{\psi}{\rho\epsilon_r}\frac{\partial(\rho H_\phi)}{\partial n} dl - \iint_\Omega \frac{\nabla\psi \cdot \nabla(\rho H_\phi)}{\epsilon_r \rho} dA + k_0^2 \iint_\Omega \frac{\mu_r \psi(\rho H_\phi)}{\rho} dA = 0. \qquad (4)$$

The TE weak formulation is obtained from duality. A single equation mathematically expressing both TE and TM cases is written as

$$\oint_{\partial\Omega} \frac{\psi}{\rho f}\frac{\partial u}{\partial n} dl - \iint_\Omega \frac{\nabla\psi \cdot \nabla u}{f\rho} dA + k_0^2 \iint_\Omega \frac{g\psi u}{\rho} dA = 0, \qquad (5)$$

where, for TM modes, $u = \rho H_\phi$ , $f$ is the relative electric permittivity $\epsilon_r$, and $g$ is the relative magnetic permeability $\mu_r$ inside the cavity. For TE modes, $u = \rho E_\phi$, $f = \mu_r$, and $g = \epsilon_r$.

## III. THE MESHLESS APPROACH

Equation (5) is numerically evaluated by a meshless approach, which begins by spreading nodes (field nodes) over the problem domain $\Omega$ and its boundary $\partial\Omega$ (see Fig. 1). Every node $x_I$ has an associated shape function $\phi_I$, which is different from zero only in a small region around the node I. This region is known as node I's influence domains $\Omega_{F_I}$, as illustrated in Fig. 1. The influence domain can be of any shape (generally circular, square, or rectangular forms are adopted), as long as their union covers all the problem domain $\Omega$. In this work, circular influence domains are employed. The local approximation of $u$ at a point x is then given by:

$$u^h(x) = \sum_I^N \phi_I(x) u_I, \qquad (6)$$

where $I = 1, \ldots, N$ represents the nodes whose influence domains include point x and $u_I$ are the nodal values. The set of N nodes is known as the support domain $\Omega_x$ (Fig. 1). To build the shape function we have adopted the moving least squares (MLS) method, which begins by

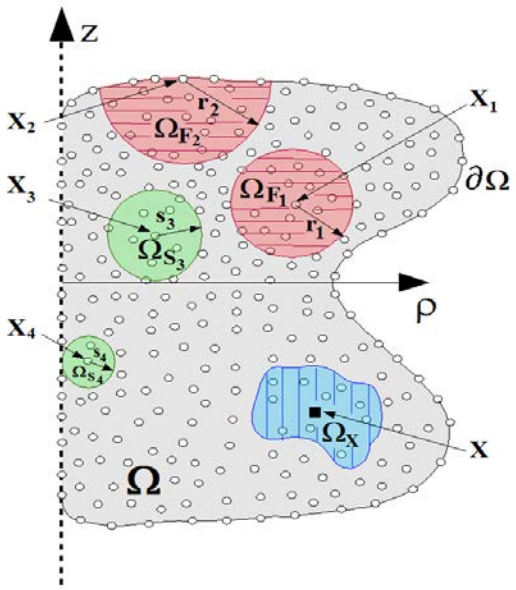


Fig. 1. A computational domain $\Omega$ and its boundaries $\partial\Omega$. The horizontal striped regions are influence domains $\Omega_{F_1}$ and $\Omega_{F_2}$ of the nodes $x_1$ and $x_2$, respectively. The non-striped regions are test domains $\Omega_{S_3}$ and $\Omega_{S_4}$ of the nodes $x_3$ and $x_4$, respectively. The vertical striped region is the support domain $\Omega_x$ of a point x.

expressing $u^h$ as [2]

$$u^h(\mathrm{x}) = \mathbf{p}^{\mathrm{T}}(\mathrm{x})\mathbf{a}(\mathrm{x}), \qquad \forall\, \mathrm{x} \in \Omega_{\mathbf{x}}, \quad (7)$$

where $\mathbf{p}^{\mathrm{T}}(\mathrm{x}) = [p^1(\mathrm{x}), p^2(\mathrm{x}), \ldots, p^m(\mathrm{x})]$ is a complete monomial basis with $m$ terms and $\mathbf{a}(\mathrm{x})$ is a vector containing the coefficients $a^j(\mathrm{x})$, $j = 1, 2, \ldots, m$, which are functions of the space co-ordinates $\mathrm{x} = [\rho,\ z]^{\mathrm{T}}$. For example, using a first order polynomial, $\mathbf{p}^{\mathrm{T}}(\mathrm{x})$ is given by:

$$\mathbf{p}^{\mathrm{T}}(\mathrm{x}) = [1, \rho, z], \quad \text{for } m = 3. \qquad (8)$$

The coefficient vector $\mathbf{a}(\mathrm{x})$ is determined by minimizing a weight discrete $L_2$-norm defined as:

$$J = \sum_{\mathrm{I}=1}^{N} w(\mathrm{d_I})\,[\mathbf{p}^{\mathrm{T}}(\mathrm{x_I})\mathbf{a}(\mathrm{x}) - \mathrm{u_I}]^2, \qquad (9)$$

where $N$ is the number of nodes in the support domain of x and $\mathrm{x_I}$ are the coordinates of node I. The chosen weighting function is a third order spline function expressed by [2]:

$$w(d_I) = \begin{cases} \frac{2}{3} - 4{d_\mathrm{I}}^2 + 4{d_\mathrm{I}}^3 & \text{if } d_I \le \frac{1}{2} \\ \frac{4}{3} - 4d_\mathrm{I} + 4{d_\mathrm{I}}^2 - \frac{4}{3}{d_\mathrm{I}}^3 & \text{if } \frac{1}{2} < d_\mathrm{I} \le 1 \\ 0 & \text{otherwise,} \end{cases} \qquad (10)$$

where $d_\mathrm{I} = |\mathrm{x} - \mathrm{x_I}|/r_\mathrm{I}$ and $r_\mathrm{I}$ is the radius of the influence domain associated to node I, as shown in Fig. 1. The $r_\mathrm{I}$ values are obtained in a two step preprocess: (i) a small set of $N_{ini}$ neighbor nodes for each node I is selected; (ii) the distance between node I and its furthest neighbor node ($dist_\mathrm{I}$) is evaluated and multiplied by the dimensionless size parameter $\alpha_\mathrm{I}$, defining $r_I = dist_I \cdot \alpha_I$.

The minimization of $J$ results in [2]

$$\mathbf{a}(\mathrm{x}) = \mathbf{A}^{-1}(\mathrm{x})\mathbf{B}(\mathrm{x})\mathbf{U}, \qquad (11)$$

where $\mathbf{A}$ is the moment matrix, given by

$$\mathbf{A}(\mathrm{x}) = \sum_{\mathrm{I}=0}^{N} w(\mathrm{x} - \mathrm{x_I})\mathbf{p}(\mathrm{x_I})\mathbf{p}^{\mathrm{T}}(\mathrm{x_I}), \qquad (12)$$

the matrix $\mathbf{B}$ has the form $\mathbf{B}(\mathrm{x}) = [\boldsymbol{B_1}, \boldsymbol{B_2}, \ldots, \boldsymbol{B_N}]$, with column elements $\boldsymbol{B}_\mathrm{I}$ defined by

$$\boldsymbol{B}_\mathrm{I} = \mathrm{w(d_I)}\mathbf{p}(\mathrm{x_I}), \qquad (13)$$

and $\mathbf{U}$ is the vector that contains all fictitious nodal values of support domain $\Omega_\mathrm{x}$, $\mathbf{U} = \{\mathrm{u_1}, \ldots, \mathrm{u_N}\}^{\mathrm{T}}$.

Equation (7) can be rewritten using (11) as follows [2]:

$$u^h(\mathrm{x}) = \mathbf{p}^{\mathrm{T}}(\mathrm{x})\mathbf{A}^{-1}(\mathrm{x})\mathbf{B}(\mathrm{x})\mathbf{U} = \boldsymbol{\Phi}^{\mathrm{T}}(\mathrm{x})\mathbf{U}, \quad (14)$$

where $\boldsymbol{\Phi}(\mathrm{x})$ is the matrix of MLS shape functions corresponding to $N$ nodes of $\Omega_\mathrm{x}$, written as:

$$\boldsymbol{\Phi}^{\mathrm{T}}(\mathrm{x}) = [\phi_1(\mathrm{x}), \phi_2(\mathrm{x}), \ldots, \phi_N(\mathrm{x})], \qquad (15)$$

where $\phi_\mathrm{I}(\mathrm{x})$ is the shape function of the Ith node of $\Omega_\mathrm{x}$. Equation (14) indicates that shape functions and, consequently, the MLS approximation depend on $\mathbf{A}^{-1}$. A well-conditioned $\mathbf{A}$ matrix is guaranteed using $\mathrm{N} \gg \mathrm{m}$ and avoiding certain singular node distributions (e.g., a collinear node distribution) [2]. Equation (14) is the matrix form of (6).

The partial derivatives of $\boldsymbol{\Phi}$ with respect to $\rho$ are obtained as:

$$\boldsymbol{\Phi}^{\mathrm{T}}_{,\rho} = \mathbf{p}_{,\rho}{}^{\mathrm{T}}\mathbf{A}^{-1}\mathbf{B} + \mathbf{p}^{\mathrm{T}}\mathbf{A}^{-1}_{,\rho}\mathbf{B} + \mathbf{p}^{\mathrm{T}}\mathbf{A}^{-1}\mathbf{B}_{,\rho}, \quad (16)$$

where the subscript $,\rho$ denotes the parcial derivative with respect to $\rho$. Derivatives of the

shape function with respect to $z$ are obtained in a similar way [2].

Figure 2 illustrates a MLS shape function for a node located at $\mathrm{x}^{\mathrm{T}} = [0,0]$, obtained using 25 nodes uniformly spread over Ω. Each node in the domain will have a similar function associated to it and the final approximation will be given by (6). The precision of the approximation depends on the node distribution, but if we define a FEM mesh and generate a MLS approximation using the FEM mesh nodes, the MLS approximation is typically more precise than FEM [2]. Figure 3 shows the first derivative of the MLS shape function with respect to $\rho$.

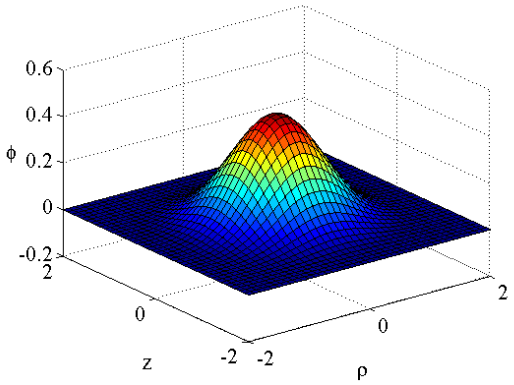


Fig. 2. Shape function, $\phi$.

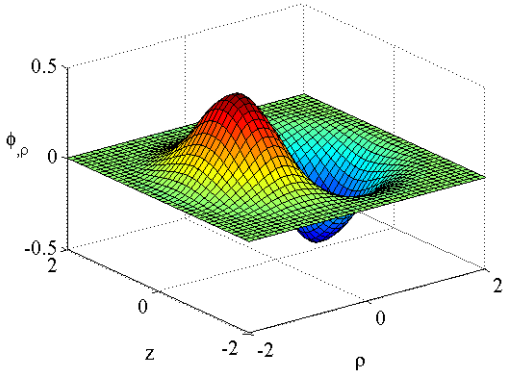


Fig. 3. First derivative of shape function, $\phi_{,\rho}$.

## IV. THE MLPG ANALYSIS

The MLS function approximation is now applied to describe $u$ in equation (5). The proposed analysis is similar to MLPG4/LBIE (local boundary integral equation) [2], but it differs in what concerns the imposition of boundary conditions, which follows the treatment of interface conditions discussed in [9]. For the MLPG method, it is necessary to spread nodes inside Ω (interior nodes) and over the global boundary $\partial\Omega$ (boundary nodes), as shown in Fig. 1. Interior nodes use the test function $\psi_{\mathrm{I}}$, which acts in a local region near node I (the node's test domain $\Omega_{\mathrm{S_I}}$) where the integrations are carried out. In LBIE, $\Omega_{\mathrm{S_I}}$ is generally a circle centered at the interior node I and the corresponding test function $\psi_{\mathrm{I}}$ must satisfy the following requirements:

$$\nabla^2\psi_{\mathrm{I}} = -\delta(\mathrm{x}-\mathrm{x_I}) \text{ , a delta function at } \mathrm{x_I}, \quad (17)$$

$$\psi_I = 0, \text{ at the test domain boundary } \Omega_{\mathrm{S}}. \quad (18)$$

Conditions (17) and (18) are satisfied by the following test function:

$$\psi_{\mathrm{I}}(\mathrm{x}) = \frac{1}{2\pi}\ln\left(\frac{s_{\mathrm{I}}}{|\mathrm{x}-\mathrm{x_I}|}\right), \quad (19)$$

where $s_{\mathrm{I}}$ is the radius of the circular domain $\Omega_{\mathrm{S_I}}$, chosen such that $\Omega_{\mathrm{S_I}}$ does not intersect the global boundary $\partial\Omega$ [9]. The local weak form can be obtained by replacing $\psi$ by $\psi_{\mathrm{I}}$ and $u$ by $u^h$ in (5), where the boundary integral vanishes due to (18), resulting in:

$$\iint_{\Omega_s}\frac{\nabla\psi_{\mathrm{I}}\cdot\nabla u^h}{f\rho}dA - k_0^2\iint_{\Omega_s}\frac{g\psi_{\mathrm{I}}u^h}{\rho}dA = 0. \quad (20)$$

This local formulation is versatile. For example, it can be used to analyze a layered medium of permissivities or permeabilities. In these cases, it is necessary to deal with the discontinuity between different media, which can be accomplished by using the techniques described in [11].

All boundary nodes are used to impose the boundary conditions and a simple technique (known as the meshless collocation scheme) that requires no integration is adopted [9]. Boundary conditions are expressed in a general form as:

$$b(\mathrm{x_I})u^h(\mathrm{x_I}) + c(\mathrm{x_I})\frac{\partial u^h(\mathrm{x_I})}{\partial n} = h(\mathrm{x_I}), \quad (21)$$

where $b = 1$ and $c = 0$ if $\mathrm{x_I}$ is at a Dirichlet boundary or $b = 0$ and $c = 1$ if it is at a Neumann boundary. $h$ is a known imposed value. In a cavity with a perfect electric conductor wall, for TE modes, the function $u$ satisfies a Dirichlet boundary condition over the wall (i.e. $E_\phi = 0$), while for TM modes a Neumann condition is imposed ($\partial H_\phi/\partial n = 0$). Over the axis of

symmetry (z-axis), the Dirichlet condition $u = 0$ is imposed for both modes, as $\rho = 0$.

The numerical solution of the problem is obtained by transforming (20) and (21) into a set of linear equations, resulting in:

$$(C - k_o^2 D)u_I = 0, \tag{22}$$

where, for interior nodes,

$$C_{\mathrm{IJ}} = \iint_{\Omega_S} \frac{\nabla\psi_{\mathrm{I}} \cdot \nabla\phi_{\mathrm{J}}}{f\rho}\, dA, \tag{23}$$

$$D_{\mathrm{IJ}} = \iint_{\Omega_S} \frac{g\psi_{\mathrm{I}}\phi_{\mathrm{J}}}{\rho}\, dA, \tag{24}$$

and, for boundary nodes, $C_{\mathrm{IJ}} = \phi_{\mathrm{J}}(\mathrm{x_I})$ (Dirichlet) or $C_{\mathrm{IJ}} = \partial\phi_{\mathrm{J}}(\mathrm{x_I})/\partial n$ (Neumann), and $D_{\mathrm{IJ}} = 0$. $C$ and D are sparse matrices, which reduce the memory requirements and computation time by eliminating operations on zero elements. The wavenumbers $k_0$ are obtained from the eigenvalues of (22).

## V. NUMERICAL RESULTS

Axially symmetric resonant cavities can be analyzed by the proposed technique. We present results for two cavities: a cylindrical and a spherical cavity. Only modes without $\phi$-variation are analyzed (n = 0).

In the first example, we analyze a cylindrical cavity with radius equal to 1m, height equal to 2m, and vacuum in its interior ($\varepsilon_r = \mu_r = 1$). Table 1 shows the first resonant wavenumbers evaluated analytically [12] and numerically, using 3321 uniformly spaced nodes over the domain and its boundary (node spacing of 2.5cm). Table 1 also shows the percentual relative errors. The maximum error is approximately 0.49% for TM and 0.05% for TE modes. We do not have an explanation for the larger TM error. The main difference between the TE and TM problems is the boundary conditions: the TE problem only uses Dirichlet boundary conditions while the TM one has a Neumann boundary at the cavity wall. However, this difference does not completely explain the larger TM error.

In order to evaluate the convergence of the proposed method, it is necessary to determine the best values for the parameters $\alpha_{\mathrm{I}}$, which were defined in Section III to determine the node's influence domain. Our study demonstrated that the numerical accuracy depends on this parameter, with small $\alpha_{\mathrm{I}}$ values leading to large errors because of the insufficient number of nodes to perform a precise MLS approximation. However, larger $\alpha_{\mathrm{I}}$ values result in larger number of nodes inside the support domains. This results in an increase in time to evaluate the shape functions and in less sparse matrices, which also require more computing time to determine the eigenvalues and eigenvectors.

Table 1: Resonant wavenumbers $k$ $(rad/m)$ and relative errors (%) for the cylindrical cavity

| $\mathbf{MODE_{npq}}$ | Analytical Solution | Numerical Solution | Error (%) |
|---|---|---|---|
| $\mathrm{TE}_{011}$ | 4.1411799 | 4.1423492 | 0.0282 |
| **$\mathbf{TE_{012}}$** | 4.9549545 | 4.9570499 | 0.0422 |
| $\mathrm{TE}_{013}$ | 6.0735970 | 6.0769282 | 0.0548 |
| $\mathrm{TM}_{010}$ | 2.4048255 | 2.4167237 | 0.4947 |
| $\mathrm{TM}_{011}$ | 2.8723835 | 2.8865461 | 0.4930 |
| $\mathrm{TM}_{012}$ | 3.9563607 | 3.9757341 | 0.4896 |

Figure 4 presents the relative error as a function of $\alpha_I$. This figure (obtained with $N_{ini} = 6$ and 1981 uniformly spaced nodes over the domain and its boundary, with a node spacing of 33 cm) shows that optimum values of $\alpha_I$ are between 1.3 and 2.0. The simulations suggest the optimum values $\alpha_I = 1.3$ and 1.6 for TE and TM modes, respectively.

Figure 5 presents the convergence results for the six modes present in Table 1. The node spacing is changed in the interval [0.333 m, 0.025 m] and the convergence rates are approximately 1.84 and 1.2 for TE and TM modes, respectively.

Figures 6 through 8 present the electrical and magnetic field distributions inside the cavity, which were obtained extracting the field components from the eigenvectors using 1891 uniformly spaced nodes over the domain and its boundary (node spacing of 33 cm). Figure 6 shows $\mathrm{TE}_{011}(E_\phi)$ and $\mathrm{TM}_{010}(H_\phi)$ modes, Fig. 7 shows $\mathrm{TE}_{012}(E_\phi)$ and $\mathrm{TM}_{011}(H_\phi)$ modes, and Fig. 8 shows $\mathrm{TE}_{013}(E_\phi)$ and $\mathrm{TM}_{012}(H_\phi)$ modes. These numerical field distributions are in agreement with analytical results [12].

The second test problem is a spherical cavity with radius equal to 1 m and vacuum in its interior ($\varepsilon_r = \mu_r = 1$). Table 2 shows analytical [12] and numerical resonant wavenumbers ($n = 0$, with

2705 nodes uniformly spaced over the domain and its boundary, with node spacing of 2.5cm). The maximum error is approximately 0.69% for TM and 0.066% for TE modes.

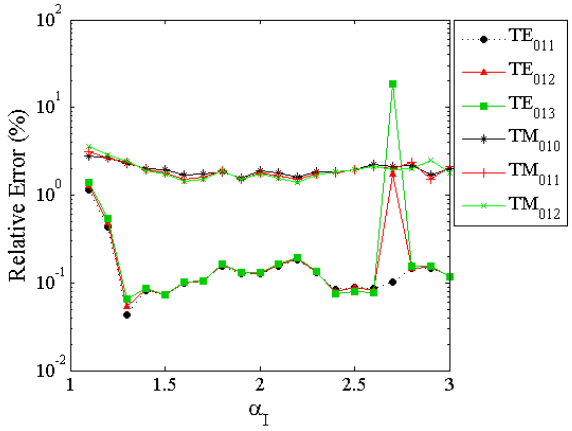


Fig. 4. Influence of the $\alpha_I$ values on the accuracy of the results for the cylindrical cavity.

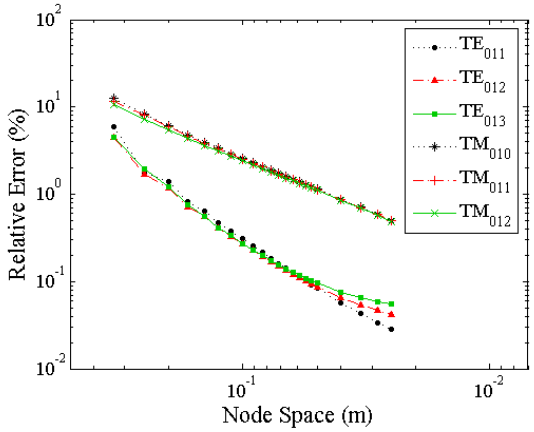


Fig. 5. Convergence of TE and TM modes for the cylindrical cavity.

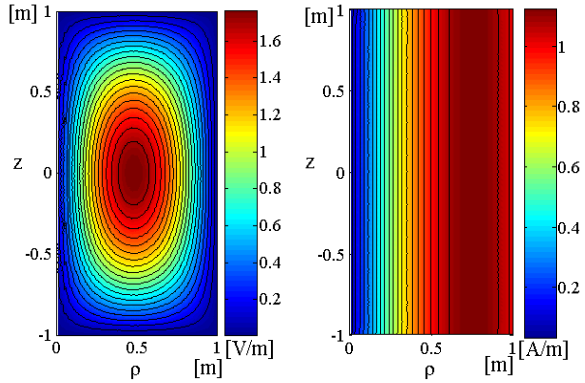


Fig. 6. Numerical field distribution in the cylindrical cavity: (a) $\mathrm{TE}_{011}(E_\phi)$ and $\mathrm{TM}_{010}(H_\phi)$.

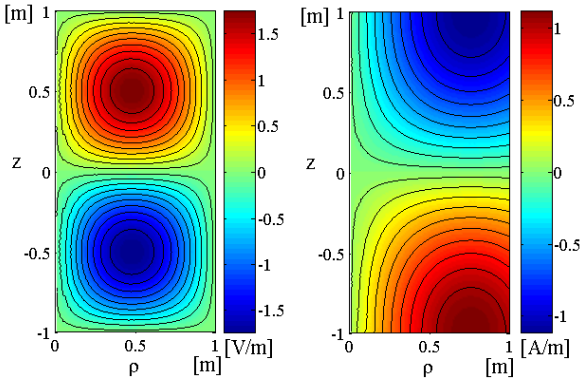


Fig. 7. Numerical field distribution in the cylindrical cavity: (a) $\mathrm{TE}_{012}(E_\phi)$ and $\mathrm{TM}_{011}(H_\phi)$.

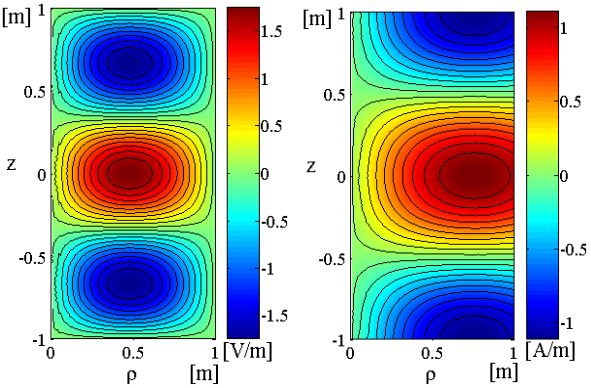


Fig. 8. Numerical field distribution in the cylindrical cavity: (a) $\mathrm{TE}_{013}(E_\phi)$ and $\mathrm{TM}_{012}(H_\phi)$.

Table 2: Resonant wavenumbers $k\ (rad/m)$ and relative errors (%) for the spherical cavity

| $\mathbf{MODE_{npq}}$ | **Analytical Solution** | **Numerical Solution** | **Error (%)** |
|---|---|---|---|
| $\mathrm{TE}_{011}$ | 4.4934095 | 4.4949440 | 0.0341 |
| **$\mathbf{TE_{012}}$** | 5.7634592 | 5.7664633 | 0.0521 |
| $\mathrm{TE}_{013}$ | 6.9879300 | 6.9925602 | 0.0662 |
| $\mathrm{TM}_{010}$ | 2.7437072 | 2.7579069 | 0.5175 |
| $\mathrm{TM}_{011}$ | 3.8702386 | 3.8929146 | 0.5859 |
| $\mathrm{TM}_{012}$ | 4.9734204 | 5.0077221 | 0.6897 |

Figure 9 presents the convergence results for the modes present in Table 1 (built with the same $N_{ini}$ and $\alpha_I$ values chosen for the cylindrical cavity). The convergence rates are approximately 2.0 and 1.4 for TE modes and TM modes, respectively.

Figures 10 through 11 present the numerical field distribution inside the spherical cavity, obtained using 1553 nodes uniformly spaced over the domain and its boundary (node spacing of

33cm). Figure 10 shows $\mathrm{TE}_{011}(E_\phi)$ and $\mathrm{TM}_{010}(H_\phi)$ modes, Fig. 11 shows $\mathrm{TE}_{012}(E_\phi)$ and $\mathrm{TM}_{011}(H_\phi)$ modes, and Fig. 12 shows $\mathrm{TE}_{013}(E_\phi)$ and $\mathrm{TM}_{012}(H_\phi)$ modes. Again, the field distributions are in perfect agreement with analytical results [12].

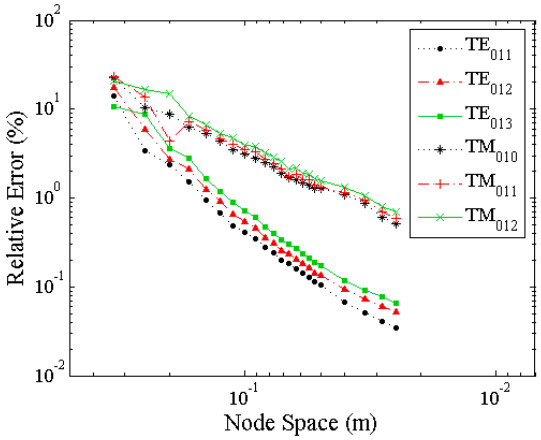


Fig. 9. Convergence of TE and TM modes for the spherical cavity.

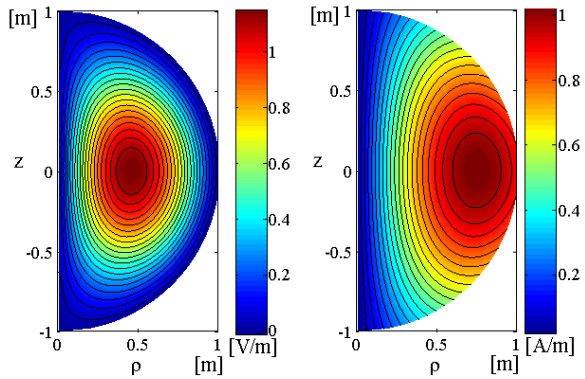


Fig. 10. Numerical field distribution in the spherical cavity: (a) $\mathrm{TE}_{011}(E_\phi)$ and $\mathrm{TM}_{010}(H_\phi)$.

## CONCLUSIONS

This work discussed the numerical analysis of axisymmetric resonant cavities by a Meshless Local Petrov-Galerkin (MLPG) method. The axisymmetric weak formulation is simple and versatile. The proposed MLPG analysis uses a collocation method to impose the boundary conditions, which simplifies the algorithm. The employed method is a local weak-form method and does not require a background mesh.

Two axially symmetric resonant cavities had their eigenvalues and field distributions numerically evaluated. The proposed method had its convergence rate determined, which for a cylindrical cavity are 1.84 and 1.2 for TE and TM modes, respectively. For a spherical cavity, the convergence rates are 2 and 1.4 for TE and TM modes, respectively. The method can be easily adaptable to different axially symmetric geometries.

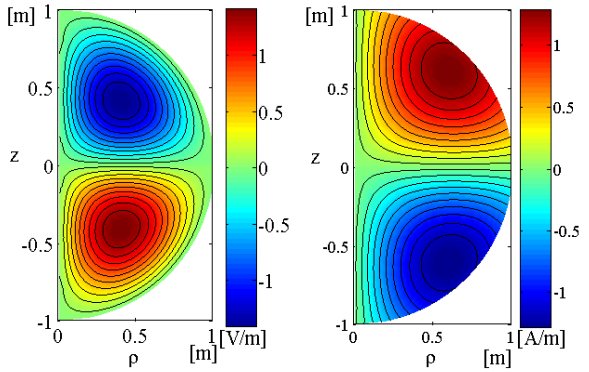


Fig. 11. Numerical field distribution in the spherical cavity: (a) $\mathrm{TE}_{012}(E_\phi)$ and $\mathrm{TM}_{011}(H_\phi)$.

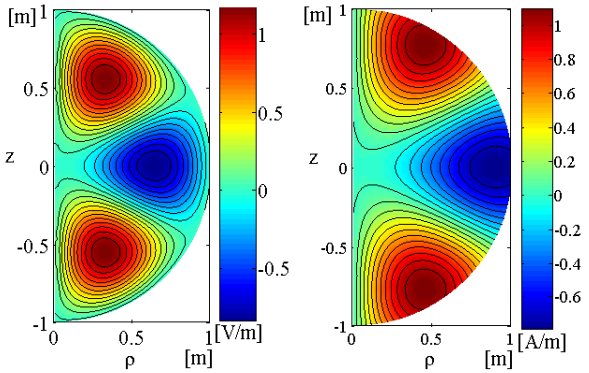


Fig. 12. Numerical field distribution in the spherical cavity: (a) $\mathrm{TE}_{013}(E_\phi)$ and $\mathrm{TM}_{012}(H_\phi)$.

## ACKNOWLEDGMENT

This work was partially supported by CAPES, CNPq, and FAPEMIG.

### REFERENCES

[1] A. Taflove and S. C. Hagness, *Computational Electrodynamics: The Finite-Difference Time-Domain Method, 3rd ed.* Norwood, MA: Artech House, 2005.

[2] G. Liu, *Mesh Free Methods: Moving Beyond the Finite Element Method*, CRC Press, 2nd Edition 2009.

[3] G. Ala, E. Francomano, A. Tortorici, E. Toscano, and F. Viola, "A Smoothed Particle Interpolation

Scheme for Transient Electromagnetic Simulation," *IEEE Trans. Magnetics*, vol. 42, no. 4, pp. 647-650, 2006.

[4] P. Jiang, S. Li, and C. Chan, "Analysis of Elliptical Waveguides by a Meshless Collocation Method with Wendland Radial Basis Functions," *Microwave and Optical Technology Letters*, vol. 32, no. 2, 2002.

[5] T. Kaufmann, C. Fumeaus, C. Engstrom, and R. Vahldieck, "Meshless Eigenvalue Analysis for Resonant Structures Based on the Radial Point Interpolation Method," *APMC 2009 Asia Pacific,* pp. 818-821, 2009.

[6] R. K. Gordon and W. E. Hutchcraft, "The Use of Multiquadric Radial Basis Functions in Open Region Problems," *Applied Computational Electromagnetic Society (ACES) Journal*, vol. 21, no. 2, pp. 127–134, July 2006.

[7] A. Manzin and O. Bottauscio, "Element-Free Galerkin Method for the Analysis of Electromagnetic-Wave Scattering," *IEEE Trans. Magnetics,* vol. 44, no. 6, pp. 1366-1369, 2008.

[8] B. Correa, E. Silva, A. Fonseca, D. Oliveira, and R. Mesquita, "Meshless Local Petrov-Galerkin in Solving Microwave Guide Problems," *IEEE Trans. Magnetics*, vol. 47, p. 1526-1529, 2011.

[9] W. Nicomendes, R. Mesquita, and F. Moreira, "A Meshless Local Petrov-Galerkin Method for Three-Dimensional Scalar Problems," *IEEE Trans. Magnetics*, vol. 47, pp. 1214-1217, 2011.

[10] A. Peterson, S. Ray, and R. Mittra, *Computational Methods for Electromagnetics*, IEEE Press, 1998, Sect. 8.8.

[11] Q. Li, S. Shen, Z. Han, and S. Atluri, "Application of Meshless Local Petrov-Galerkin (MLPG) to Problems with Singularities, and Material Discontinuities, in 3-D Elasticity," CMES, vol. 4, no. 5, pp. 571-585, 2003.

[12] R. F. Harrington, *Time-Harmonic Electromagnetic Fields*; McGraw-Hill, New York, 1961.

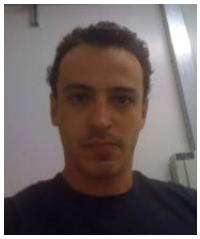

**Ramon Dornelas Soares** received his Bachelor's and Master's degrees from the National Institute of Telecommunication (INATEL), Santa Rita do Sapucai, Brazil, in 2002 and 2005. He is currently working towards his Doctor's degree in Electrical Engineering at the Federal University of Minas Gerais, Brazil. His main research interests are in the area of electromagnetic field computation.

**Renato Cardoso Mesquita** is a professor at the Electrical Engineering Department of the Federal University of Minas Gerais, Brazil. He received his B.E. and M.Sc. degrees from the Federal University of Minas Gerais, in 1982 and 1986, and his Ph.D from the Federal University of Santa Catarina, Brazil, in 1990. His main research interests are in the area of electromagnetic field computation.

**Fernando José da Silva Moreira** was born in Rio de Janeiro, Brazil, in 1967. He received the B.S. and M.S. degrees in Electrical Engineering from the Pontifical Catholic University of Rio de Janeiro, Brazil, in 1989 and 1992, and the Ph.D. degree in Electrical Engineering from the University of Southern California in 1997. Since 1998, he has been with the Department of Electronics Engineering of the Federal University of Minas Gerais, Brasil, where he is currently an Associate Professor. His research interests are in the areas of electromagnetics, antennas, and propagation.

# Optimization for Weighed Cooperative Spectrum Sensing in Cognitive Radio Network

**Xin Liu and Xuezhi Tan**

Communication Research Center
Harbin Institute of Technology, Harbin, 150080, P. R. China
liuxinstar1984@gmail.com, tanxzhit@gmail.com

***Abstract*** ─ In this paper, an optimal weighed cooperative spectrum sensing strategy based on data fusion is investigated in cognitive radio network. Cognitive radios sense the channels by energy detection independently and send their results to a fusion center, in which the observed data are fused by the specific weighing. The optimal sensing problem, which seeks to minimize interference and maximize throughput by keeping the probabilities of false alarm and detection within the allowable limit, is formulated. In particular, both the cooperative detections in single channel and multi-channels are analyzed, and the optimal weighed factors are obtained by Cauchy-inequality. Based on the weighing, we transform the non-convex optimal problem of multi-channel sensing with double parameters and nonlinear constraints into a convex problem with single parameter and linear constraints, which can be easily solved. The simulation shows that the proposed algorithm can achieve lower interference and higher throughput with less computing complexity, and the detected performance of each sub-channel can also be guaranteed. It also indicates that there is a conflict between improving throughput and decreasing interference, and the proposed algorithm can make better use of spectrum by balancing the conflict.

***Index Terms*** ─ Cognitive radio, cooperative spectrum sensing, data fusion, energy detection, signal processing.

## I. INTRODUCTION

Since wireless technologies continue to grow, more and more spectrum resources will be needed. Within the current spectrum allocation, all of the frequency bands are allocated to the legal user authorized by the government, which is called primary user (PU), and the unlicensed user is not permitted to access to the spectrum [1]. A survey of spectrum utilization made by the Federal Communications Commission (FCC) has indicated that 70% of the allocated spectrum in US has not been well-utilized, and in New York City, only 13.1% of the spectrum source from 30 MHz to 3 GHz is well used [2]. Moreover, the spectrum usage varies significantly in various time, frequency, and geographic locations, so it is difficult to reuse the spectrum according to the previous allocation principle [3].

Spectrum utilization can be improved significantly by allowing an unlicensed user to utilize a licensed band when the PU is absent, and therefore, a new intelligent unlicensed wireless communication system named cognitive radio (CR) is proposed to promote the efficient use of the spectrum [4]. A CR based on software radio, can reuse the temporarily unused radio spectrum allocated to PU, which is called idle spectrum, by sensing and adapting to the environment. Since the chief principle for CR to operate in the idle channel is that CR can't cause harmful interference to the PU, the CR must continuously sense the idle frequency band used by it, in order to detect the presence of the PU. Once the PU appears, CR should immediately vacate this band to search a new idle spectrum [5].

Presently, three schemes (namely, matched filter detection, energy detection and cyclo-stationary feature detection) have been presented for the single-user detection in CR networks. Matched filter detection can achieve high processing gain while cyclo-stationary feature detection can distinguish the primary signal under

*Submitted On: May 14, 2011*
*Accepted On: October 13, 2011*

low SNR. However, both of them need the prior information about the primary signal, which is difficult to get in the actual case [6]. Energy detection has been put forward as an optimal method for the occasion where CR cannot gather sufficient information about the primary signal [7]. However, unfortunately, the performance of energy detection could be degraded in the fading and shadow environment. In order to cope with this problem, the cooperative spectrum sensing has been proposed [8].

It has been proved that compared to the single-user detection, by allowing multiple CRs to cooperatively sense spectrum, the detected performance in the fading and shadow environment can be improved greatly [9]. In cooperative spectrum sensing, each CR makes a local decision by energy detection, and then reports its decision result to a fusion center in order to obtain the final decision on the presence of PU [10]. The fusion rule of the cooperative detection includes decision fusion and data fusion, and in this paper, we focus on data fusion which can achieve higher performance while more CRs are in deep fading [11].

Light-weight cooperative detection based on decision fusion is proposed in [12] to increase the detection probability under a specific false alarm probability. By its predominant nature as a data fusion scheme, an optimal linear cooperative spectrum sensing for CR network based on weighed data fusion is proposed by [13]. In [13], the detected performance is improved through the optimum weight vector obtained by the global solution of the objective function. However, the complexity brought by the solution of non-convex optimization problem is high. The linear combination weights for a global fusion center that together maximize global probability of detection [14]. However, the probability of false alarm which needs to be decreased for improving the spectrum utilization is lack of consideration. The researches in [12-14] are all about the cooperative detection in the single channel. An optimal multi-band joint detection for spectrum sensing in CR network is proposed in [15], and the spectrum sensing problem is formulated as a class of optimization problems which maximize the throughput of CR. However, the objective function and constraints in [15] are all nonlinear functions, and the interior-point method adopted to solve the problem is complex.

In this paper, the weighed cooperative detection based on data fusion is researched further and both the cooperative detections in single channel and multi-channel are considered. Our technical contributions are summarized as follows: (1) We respectively obtain the optimal weighed factors of the cooperative detection in single channel from the two aspects: minimizing interference and maximizing throughput, and the optimal problem can be further expressed as maximizing probability of detection and minimizing probability of false alarm subject to the constraints of throughput and interference respectively. The solution of the proposed optimal problem is based on the Cauchy-inequality which has less complexity. (2) By the research result of the detection in single channel, the non-convex optimal problem of the cooperative detection in multi-channel with double parameters and nonlinear constraints can be transformed into a convex optimal problem with single parameter and linear constraints, which can be solved easily. (3) Our simulation proves that there is an obvious conflict between improving throughput and decreasing interference, however the proposed algorithms can balance the conflict better.

The rest of the paper is organized as follows. In Section II, we describe the single-user energy detection. In Section III, we develop the weighed cooperative detection in single channel in order to minimize interference to PU and maximize throughput of CR. Based on the research result in Section III, the optimization of the cooperative detection in multi-channel is proposed and solved in Section IV. The advantages of the proposed cooperative spectrum sensing algorithm are then illustrated by the simulations in Section V, and lastly the conclusions are drawn in Section VI.

## II. SINGLE USER DETECTION

### A. Primary signal assumption

Suppose that there are $N$ users in the CR network, and the received signal of CR$i$ can be denoted by the binary assumption defined as (1). Hypothesis $H_1$ denotes the presence of PU while hypothesis $H_0$ denotes the absence of PU.

$$\begin{aligned} H_0 &: x_i(l) = n(l) \qquad i = 1,2,...,N \\ H_1 &: x_i(l) = h_i s(l) + n(l) \quad l = 1,2,...,M \end{aligned}, \tag{1}$$

where $x_i(l)$ is the received signal of CR$i$, and $l$ is the sampling node of the received signal. $s(l)$ is the primary signal which is assumed to be a uniform random process with zero mean and variance $\sigma_s^2$, while the noise $n(l)$ is assumed to be Gaussian random process with zero mean and variance $\sigma_n^2$, and $s(l)$ and $n(l)$ are completely independent. $h_i$ is the channel gain between the PU and CR$i$.

**B. Energy detection**

If prior knowledge of the primary signal is unknown, the energy detection method is optimal for detecting any zero-mean constellation signals.

In the energy detection approach, the radio-frequency (RF) energy in the channel or the received signal strength indicator is measured by CR to determine the presence of the PU. Firstly, the received signal is filtered through a band-pass filter to select the preferable bandwidth. The output signal is then squared and integrated over the observed interval. Finally, the output of the integrator is compared to a pre-set threshold for deciding the vacancy of the channel. The energy detection model is shown in Fig. 1.

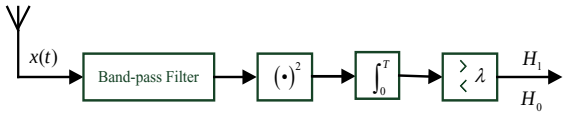


Fig. 1. Energy detection model.

Over an observed interval of $M$ samples, each CR calculates an energy statistic $T_i$ which is given by

$$T_i = \frac{1}{M}\sum_{l=1}^{M} x_i^2(l) \quad i = 1,2,...,N. \tag{2}$$

By comparing $T_i$ to the threshold $\lambda_i$, the presence of the PU can be estimated by

$$T_i \underset{H_0}{\overset{H_1}{\gtrless}} \lambda_i \ . \tag{3}$$

If $M$ is large enough, according to the center limit theorem (CLT), the probability distribution function (PDF) of $T_i$ can be approximated by a Gaussian distribution whose mean $u_{i,j}$ and variance $\sigma_{i,j}^2$ under the hypothesis $H_j$ ( $j$=0,1) are calculated respectively as follows

$$H_0 \begin{cases} u_{i,0} = \sigma_n^2 \\ \sigma_{i,0}^2 = \dfrac{2}{M}\sigma_n^4 \end{cases} \quad H_1 \begin{cases} u_{i,1} = (1+\gamma_i)\sigma_n^2 \\ \sigma_{i,1}^2 = \dfrac{2}{M}(2\gamma_i+1)\sigma_n^4 \end{cases}, \tag{4}$$

where the received SNR by CR$i$ is $\gamma_i = h_i^2\sigma_s^2/\sigma_n^2$. Therefore, according to (4), for a single CR, the probabilities of false alarm and detection are given respectively as follows

$$P_{f,i} = Q\left((\frac{\lambda_i}{\sigma_n^2} - 1)\sqrt{\frac{M}{2}}\right), \tag{5}$$

$$P_{d.i} = Q\left((\frac{\lambda_i}{\sigma_n^2} - \gamma_i - 1)\sqrt{\frac{M}{4\gamma_i + 2}}\right), \tag{6}$$

where function $Q(x) = \int_x^\infty \exp(-t^2/2)\mathrm{d}t \Big/ \sqrt{2\pi}$.

Probabilities of false alarm and detection represent the different characters of CR. The high probability of false alarm, which means the high error probability of deciding the presence of the PU, decreases the spectrum utilization, while the low probability of detection, which means the high error probability of deciding the absence of the PU, increases the interference to PU. The probability of miss detection is obtained by

$$P_{m,i} = 1 - P_{d,i}. \tag{7}$$

By setting the threshold $\lambda_i$ for a desired probability of false alarm $\tilde{P}_{f,i}$, according to (5) and (6), we obtain the probability of detection as

$$P_{d,i} = Q\left(\frac{Q^{-1}(\tilde{P}_{f,i})}{\sqrt{2\gamma_i+1}} - \gamma\sqrt{\frac{M}{4\gamma_i+2}}\right), \tag{8}$$

while by setting the threshold $\lambda_i$ for a desired probability of detection $\tilde{P}_{d,i}$, we can obtain the probability of false alarm as

$$P_{f,i} = Q\left(Q^{-1}(\tilde{P}_{d,i})\sqrt{2\gamma_i+1} + \gamma_i\sqrt{M/2}\right). \tag{9}$$

## III. COOPERATIVE DETECTION IN SINGLE CHANNEL

**A. Cooperative detection generalization**

The critical challenging issue in spectrum sensing of CR is the hidden terminal problem, which occurs when the CR is shadowed or in severe multipath fading. Figure 2 shows that CR3 is shadowed by a high building over its sensing channel, and therefore CR3 may falsely decide the

absence of the PU because of the weak primary signal power received by it. Thus, CR3 may access to the channel in spite of the interference to PU. To solve this problem, multiple CRs can be designed to collaborate in spectrum sensing. When one CR is in deep fading, the received signal may be too weak to be detected. However, by employing a CR located near by the PU as an assistant, the primary signal can be detected reliably by the infirm CR.

In this paper, we consider a cooperative spectrum sensing scenario where multiple CRs can be coordinated to enhance the performance of spectrum sensing as a whole, and by cooperative spectrum sensing, the probability of detection in fading channel can be greatly increased.

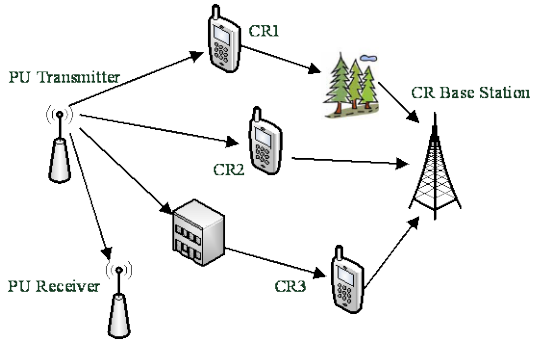


Fig. 2. Causes of unreliable detection.

In this subsection, we assume that one CR can only detect a single channel at one time and the CR network is composed of $N$ CRs, and a fusion center which manages the CR network and all the associated $N$ CRs.

In the network, cooperative detection can be defined by the following four steps

(1) Each CR performs local spectrum sensing by observing the primary signal independently, and its sensing result may be a 1-bit binary decision 0/1 which denotes $H_0$ / $H_1$ or an energy statistic of the primary signal.

(2) All the CRs transmit their sensing results to the fusion center through one dedicated control channel in an orthogonal manner.

(3) The fusion center fuses all the sensing results from the CRs in order to make the final decision to infer the presence of the PU.

(4) After getting the fusion decision, the fusion center reports its final decision to all the CRs through the dedicated control channel.

The cooperative detection model is showed in Fig. 3. It shows that cooperative spectrum sensing goes through two successive channels: the sensing channel (observed channel from PU to CR) and the reporting channel (dedicated control channel from CR to the fusion center).

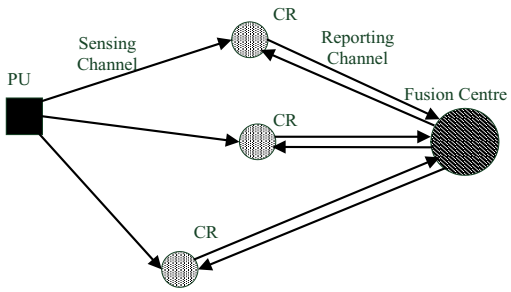


Fig. 3. Cooperative detection model in CR.

The fusion fashion by the fusion center includes the following two kinds

(1) Decision fusion: each CR makes a binary decision based on the local observation and then forwards 1-bit decision to the fusion center. At the fusion center, all the 1-bit decisions are combined together to make the final decision by a fusion rule such as OR logic, AND logic and K-OUT-N logic.

(2) Data fusion: instead of transmitting the 1-bit decision to the fusion center in the decision fusion, here each CR can just send its observed value directly to the fusion center. At the fusion center, all the observed values from CRs are accumulated and then compared to a global decision threshold for getting the final decision.

Compared to the 1-bit transmission of decision fusion, data fusion needs CR to transmit larger observed information, however, data fusion which gets less influence of the single CR, outperforms decision fusion while more CRs are shadowed or in deep fading.

### B. Cooperative detection based on weighing

Since the single detected performance of each CR is different, and the CRs with low detected performance can decrease the cooperative detected performance while those with high detected performance can increase the cooperative detected performance, in this paper, weighed factor is used to represent the contribution of the single CR to the cooperative detection. A weighed cooperative detection model based on data fusion is showed in Fig. 4.

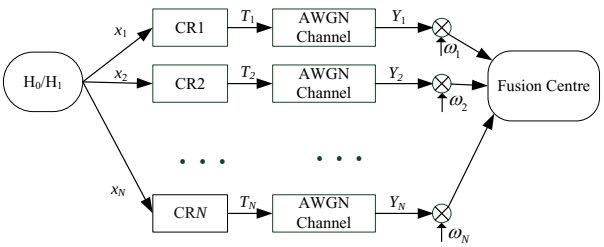


Fig. 4. Weighed cooperative detection model.

In Fig. 4, each CR sends its energy statistic $T_i$ for $i$=1, 2,…, $N$ to the fusion center which together combines all the statistics by the specific weighed factors, and gives the final decision by comparing the fusion statistic to the global threshold. The statistic received from CR$i$ by the fusion center is obtained as follows

$$Y_i = g_i T_i + v, \quad i = 1, 2, ..., N, \tag{10}$$

where $g_i$ is the channel gain between CR$i$ and the fusion center, and $v$ is AWGN with the variance $\sigma_v^2$. The fusion statistic is given by

$$Z = \sum_{i=1}^{N} \omega_i Y_i , \tag{11}$$

where the weight vector $\boldsymbol{\omega}=[\omega_1,\omega_2,\ldots,\omega_N]^{\mathrm{T}}$ satisfies $\|\boldsymbol{\omega}\|=1$. According to (4), the mean $u_{z,j}$ and variance $\sigma_{Z,j}^2$ under $H_j$ ($j$=0,1) are given by

$$H_0 \begin{cases} u_{Z,0} = \sum_{i=1}^{N} \omega_i g_i \sigma_n^2 \\ \sigma_{Z,0}^2 = \frac{2}{M} \sum_{i=1}^{N} \omega_i^2 g_i^2 \sigma_n^4 + \sigma_v^2 \end{cases}$$
$$H_1 \begin{cases} u_{Z,1} = \sum_{i=1}^{N} \omega_i g_i (1+\gamma_i) \sigma_n^2 \\ \sigma_{Z,1}^2 = \frac{2}{M} \sum_{i=1}^{N} \omega_i^2 g_i^2 (1+2\gamma_i) \sigma_n^4 + \sigma_v^2 \end{cases} . \tag{12}$$

Similar with (5-6), the cooperative probabilities of false alarm and detection are obtained as (13-14).

$$Q_f = Q\left( \frac{\lambda_g / \sigma_n^2 - \sum_{i=1}^{N} \omega_i g_i}{\sqrt{\frac{2}{M} \sum_{i=1}^{N} \omega_i^2 g_i^2 + \tilde{\sigma}_v^2}} \right), \tag{13}$$

$$Q_d = Q\left( \frac{\lambda_g / \sigma_n^2 - \sum_{i=1}^{N} \omega_i g_i (1+\gamma_i)}{\sqrt{\frac{2}{M} \sum_{i=1}^{N} \omega_i^2 g_i^2 (1+2\gamma_i) + \tilde{\sigma}_v^2}} \right), \tag{14}$$

where $\lambda_g$ is the global detection threshold of cooperative spectrum sensing, and $\tilde{\sigma}_v^2 = \sigma_v^2 / \sigma_n^4$. By supposing that the channel state between the CR and fusion center is much better than that between the PU and CR, we have $\tilde{\sigma}_v^2 \approx 0$ and $\gamma_i << 1$ for $i$=1, 2,…, $N$.

From (9), we know that the probability of detection improves with the increasing of the received SNR, and therefore, a larger weighed factor should be allocated to the CR with high SNR in order to improve the cooperative probability of detection. A simple method proposed in [16] is to obtain the weighed factors according to the SNR ratio of the CRs, which can be defined as

$$\omega_i = \gamma_i \Big/ \sqrt{\sum_{i=1}^{N} \gamma_i^2} . \tag{15}$$

The weight vector obtained by (15) can improve the cooperative detected performance; however, the channel gain between the CR and fusion center isn't considered by (15), and the detected performance may be decreased when the channel is worse.

The two basic communication characters of CR are defined as follows

(1) Decrease the interference to PU in order to guarantee the communication quality of PU.

(2) Improve the throughput of CR in order to improve the spectrum utilization.

So we can propose the optimal cooperative spectrum sensing scheme from the two aspects mentioned above.

### C. Weighing based on minimizing interference

Since the CR and PU coexist in the same channel, the communication of CR can undergo the four states defined as follows

(1) While the PU is present in the channel and the CR can detect the presence of the PU exactly, the CR can't use the channel in order to avoid disturbing the PU with the probability $Q_d$.

(2) While the PU is absent and the CR detects

the vacancy of the channel exactly, the CR can use this channel without disturbing the PU with the probability 1-$Q_f$ and rate $C_0$.

(3) While the PU is present in the channel and the CR falsely detects the vacancy of the channel, the CR can use the channel and disturb the PU with the probability 1-$Q_d$ and rate $C_1$.

(4) While the PU is absent, and the CR falsely detects the presence of the PU, the CR can vacate the idle channel and waste the spectrum utilization with the probability $Q_f$.

The CR communicates mainly at the scene (2) and (3) with the rates $C_0$ and $C_1$, which are obtained as follows

$$\begin{aligned} C_0 &= W\log_2\left(1+\frac{\sigma_R^2}{\sigma_n^2}\right) \\ C_1 &= W\log_2\left(1+\frac{\sigma_R^2}{\sigma_s^2+\sigma_n^2}\right) \end{aligned}, \tag{16}$$

where $W$ is the bandwidth of the primary channel, and $\sigma_R^2$ is the transmission power of the CR. Observably, we can have $C_0 > C_1$.

The transmission capacity of the CR at the scene (2) and (3) can be respectively obtained as

$$R_C = P_{H_0}(1-Q_f)C_0, \tag{17}$$

$$R_I = P_{H_1}(1-Q_d)C_1, \tag{18}$$

where $P_{H_0}$ and $P_{H_1}$ denote the probabilities of the hypotheses $H_0$ and $H_1$ respectively, and the transmission capacities $R_C$ and $R_I$ can be named communication throughput and interference capacity respectively. From (17) and (18), we know low $Q_f$ can increase the throughput of CR while high $Q_d$ can decrease the interference to PU.

The optimal problem in this subsection can be defined as to minimize the interference capacity in scene (3) subject to the constraint that guarantees the communication throughput in scene (2) and the spectrum utilization in scene (4). Therefore, the optimal problem can be defined as

$$\begin{aligned} &\min_{\boldsymbol{\omega}} R_I \\ &s.t.\ \ R_C \ge \varepsilon \\ &\quad\ Q_f \le \alpha \\ &\quad\ \|\boldsymbol{\omega}\| = 1 \end{aligned}, \tag{19}$$

where $\varepsilon$ and $\alpha$ are the constraint values, and generally we make $0 \le \alpha < 0.5$. According to (17-18), the optimal problem (19) can be modified as

$$\begin{aligned} &\max_{\boldsymbol{\omega}} Q_d \\ &s.t.\ \ Q_f \le \eta, \\ &\quad\ \|\boldsymbol{\omega}\| = 1 \end{aligned} \tag{20}$$

where $\eta = \min(1-\varepsilon / P_{H_0}C_0, \alpha)$ which denotes that if $\varepsilon \ge P_{H_0}C_0(1-\alpha)$, $\eta = 1-\varepsilon / P_{H_0}C$ and otherwise $\eta = \alpha$.

Since function $Q(x)$ is the decreasing function, according to (13-14), $Q_d$ improves with the increasing of $Q_f$, and when $Q_f$ reaches the upper band, $Q_d$ can also reach the maximum. Letting $Q_f = \eta$ and substituting it into (13-14), similar with (8), $Q_d$ can be denoted by $\eta$ as

$$Q_d \approx Q\left(\frac{Q^{-1}(\eta)}{\sqrt{1+2\bar{\gamma}}} - \sqrt{\frac{M}{2}}\frac{\sum_{i=1}^{N}\omega_i g_i \gamma_i}{\sqrt{\sum_{i=1}^{N}\omega_i^2 g_i^2(1+2\gamma_i)}}\right), \tag{21}$$

where $\bar{\gamma} = \sum_{i=1}^{N}\gamma_i / N$ is the average SNR of $N$ CRs. Since $Q(x)$ is the decreasing function, the optimal problem of (20) can be further modified by

$$\begin{aligned} &\max_{\boldsymbol{\omega}} f(\boldsymbol{\omega}) = \frac{\left(\sum_{i=1}^{N}\omega_i g_i \gamma_i\right)^2}{\sum_{i=1}^{N}\omega_i^2 g_i^2(1+2\gamma_i)}. \\ &s.t. \quad \|\boldsymbol{\omega}\| = 1 \end{aligned} \tag{22}$$

By substituting $d_i = \omega_i g_i \sqrt{1+2\gamma_i}$ into (22), we get

$$f(\boldsymbol{\omega}) = \left(\sum_{i=1}^{N} d_i \frac{\gamma_i}{\sqrt{1+2\gamma_i}}\right)^2 \Bigg/ \sum_{i=1}^{N} d_i^2 . \tag{23}$$

According to the Cauchy-inequality, we can get

$$\left(\sum_{i=1}^{N} d_i \frac{\gamma_i}{\sqrt{1+2\gamma_i}}\right)^2 \le \sum_{i=1}^{N} d_i^2 \sum_{i=1}^{N}\frac{\gamma_i^2}{1+2\gamma_i}. \tag{24}$$

When $d_i = \rho\gamma_i / \sqrt{1+2\gamma_i}$ where the constant $\rho > 0$, the equation of (24) which denotes that $f(\boldsymbol{\omega})$ reaches the maximum, can be obtained as

$$f_{\max}(\boldsymbol{\omega}) = \sum_{i=1}^{N}\frac{\gamma_i^2}{1+2\gamma_i}, \tag{25}$$

where the corresponding weighed factors satisfy

$$\omega_i^* = \frac{\gamma_i}{g_i(1+2\gamma_i)} \Big/ \sum_{i=1}^{N} \frac{\gamma_i^2}{g_i^2(1+2\gamma_i)^2},\ i=1,2,...,N. \tag{26}$$

By substituting (25) into (21) and (18), the minimum of interference capacity is obtained as

$$R_I = P_{H_1} C_1 \left(1 - Q\left(\frac{Q^{-1}(\eta)}{\sqrt{1+2\bar{\gamma}}} - \sqrt{\frac{M}{2}\sum_{i=1}^{N}\frac{\gamma_i^2}{1+2\gamma_i}}\right)\right). \tag{27}$$

From (27), we can know that with the increasing of the number and SNR of the cooperative CRs, the interference to the PU can be decreased.

**D. Weighing based on maximizing throughput**

Another purpose to research on the CR is to improve its communication throughput. Since the channel used by CR is allocated to the PU, and while the PU appears in the channel, the CR must vacate this channel and wait to search a new idle spectrum, it is important to improve the throughput of CR during the transmission time. It is also necessary to keep the interference to the PU below the specific tolerance, while the throughput is improved [17]. The optimal problem in this section can be defined as to maximize the communication throughput in scene (2) subject to the constraint that makes the interference in scene (3) and (4) below the tolerance. Therefore, the optimal problem can be defined as

$$\begin{aligned} &\max_{\boldsymbol{\omega}}\ R_C \\ &s.t.\ \ R_I \le \xi \\ &\quad\ Q_d \ge \beta \\ &\quad\ \|\boldsymbol{\omega}\| = 1 \end{aligned}, \tag{28}$$

where $\xi$ and $\beta$ are the constraint values, and generally we make $0.5 < \beta \le 1$. According to (17-18), the optimal problem in (28) is modified by

$$\begin{aligned} &\min_{\boldsymbol{\omega}}\ Q_f \\ &s.t.\ Q_d \ge \mu, \\ &\quad\ \|\boldsymbol{\omega}\| = 1 \end{aligned} \tag{29}$$

where $\mu = \max(1-\xi / P_{H_1}C_1, \beta)$ which denotes that if $\xi \le P_{H_1}C_1(1-\beta)$, $\mu = 1-\xi / P_{H_1}C_1$ and otherwise $\mu = \beta$.

As mentioned above, $Q_f$ increases with the increasing of $Q_d$, and when $Q_d$ reaches the lower band, $Q_f$ can reach the minimum. By substituting $Q_d = \mu$ into (13-14), $Q_f$ could be denoted by $\mu$ as

$$Q_f \approx Q\left(Q^{-1}(\mu)\sqrt{1+2\bar{\gamma}} + \sqrt{\frac{M}{2}}\frac{\sum_{i=1}^{N}\omega_i g_i \gamma_i}{\sqrt{\sum_{i=1}^{N}\omega_i^2 g_i^2}}\right). \tag{30}$$

Similar with (22), the optimal problem in (29) can be equivalent as

$$\begin{aligned} &\max_{\boldsymbol{\omega}}\ \phi(\boldsymbol{\omega}) = \frac{\left(\sum_{i=1}^{N}\omega_i g_i \gamma_i\right)^2}{\sum_{i=1}^{N}\omega_i^2 g_i^2} \\ &s.t.\quad \|\boldsymbol{\omega}\| = 1 \end{aligned}. \tag{31}$$

According to the Cauchy-inequality, the maximum of $\phi(\boldsymbol{\omega})$ can be obtained as

$$\varphi_{\max}(\boldsymbol{\omega}) = \sum_{i=1}^{N}\gamma_i^2, \tag{32}$$

where the corresponding $\boldsymbol{\omega}$ is given by

$$\omega_i^* = \frac{\gamma_i}{g_i} \Big/ \sqrt{\sum_{i=1}^{N}\frac{\gamma_i^2}{g_i^2}}\quad i=1,2,...,N. \tag{33}$$

By substituting (32) and (33) into (30) and (17), the maximum of communication throughput is obtained as

$$R_C = P_{H_0}C_0\left(1 - Q\left(Q^{-1}(\mu)\sqrt{1+2\bar{\gamma}} + \sqrt{\frac{M}{2}\sum_{i=1}^{N}\gamma_i^2}\right)\right). \tag{34}$$

According to (26) and (23), if $\gamma_i \ll 1$, it can be given that $\omega_i^* \sim \gamma_i / g_i$, and compared to (15), the proposed optimal algorithm in this paper can allocate a larger weighed factor to the CR whose channel gain to the fusion center is lower in order to compensate the lost information brought by the fading of the reporting channel, besides that increases the weighed factor of the CR with high SNR in order to improve its contribution to the cooperative detection.

## IV. COOPERATIVE DETECTION IN MULTI-CHANNEL

### A. Minimizing interference

Consider a primary communication system (multi-carrier modulation based) operating over a wideband channel which is divided into $L$ non-overlapping narrowband sub-bands. In a particular geographical region and within a particular time interval, some of the sub-bands might not be used by the PUs and are available for opportunistic spectrum access. Compared to the detection in single channel, the detection in multi-channel must consider the total detected performance of all the sub-channels. Since the fading of each channel is different, the thresholds and probabilities of false alarm and detection of each sub-channel should also be different in order to make the best use of the spectrum.

In this subsection, we present the multi-channel cooperative detection framework for wideband spectrum sensing. Since the sensing about wideband experiences different channel conditions, it is difficult to distinguish the channel fading. As mentioned in Section 3, the weighed cooperative detection can compensate the lost information brought by the channel fading, and therefore it is necessary to apply the weighed cooperation in the multi-channel detection.

The design objective is to find the optimal global threshold vector $\boldsymbol{\lambda}_g$=[$\lambda_{g,1}$,$\lambda_{g,2}$,…, $\lambda_{g,L}$] and the optimal weight vectors $\boldsymbol{\omega}^{(j)} = [\omega_1^{(j)}, \omega_2^{(j)}, ..., \omega_N^{(j)}]$ for $j$ = 1, 2,…, $L$, so that the CR system can make the efficient use of the unused idle sub-channels without causing harmful interference to the PU. For the given threshold vectors $\boldsymbol{\lambda}_g$ and $\boldsymbol{\omega}^{(j)}$, the probabilities of false alarm and detection can be compactly represented as follows

$$\begin{aligned} \boldsymbol{Q}_f(\boldsymbol{\lambda}_g, \boldsymbol{\omega}^{(j)}) &= [Q_f^{(1)}(\lambda_{g,1}, \boldsymbol{\omega}^{(1)}), ..., Q_f^{(L)}(\lambda_{g,L}, \boldsymbol{\omega}^{(L)})] \\ \boldsymbol{Q}_d(\boldsymbol{\lambda}_g, \boldsymbol{\omega}^{(j)}) &= [Q_d^{(1)}(\lambda_{g,1}, \boldsymbol{\omega}^{(1)}), ..., Q_d^{(L)}(\lambda_{g,L}, \boldsymbol{\omega}^{(L)})] \\ \boldsymbol{Q}_m(\boldsymbol{\lambda}_g, \boldsymbol{\omega}^{(j)}) &= [Q_m^{(1)}(\lambda_{g,1}, \boldsymbol{\omega}^{(1)}), ..., Q_m^{(L)}(\lambda_{g,L}, \boldsymbol{\omega}^{(L)})] \end{aligned} \quad . \quad (35)$$

The vector $\boldsymbol{Q}_m$ can be obtained by $\boldsymbol{Q}_m = \boldsymbol{I} - \boldsymbol{Q}_d$, where $\boldsymbol{I}$ denotes the all one vector.

All the $N$ CRs detect the $L$ sub-channels independently, and the received SNR of CR$i$ in the channel $j$ is defined as $\gamma_{ij}$ for $i$=1,2,…,$N$ and $j$=1, 2,…,$L$. We also denote the CR rates of the $L$ sub-channels at scene (2) and (3) as the two vectors $\boldsymbol{C}_0 = [C_{0,1}, C_{0,2}, ..., C_{0,L}]$ and $\boldsymbol{C}_1 = [C_{1,1}, C_{1,2}, ..., C_{1,L}]$ where $\boldsymbol{C}_0 > \boldsymbol{C}_1$ respectively. Therefore, the total communication throughput and interference capacity of the CR in $L$ sub-channels can be respectively obtained as follows

$$R_C = P_{H_0} \sum_{j=1}^{L} C_{0,j} \left(1 - Q_f^{(j)}(\lambda_{g,j}, \boldsymbol{\omega}^{(j)})\right), \quad (36)$$

$$R_I = P_{H_1} \sum_{j=1}^{L} C_{1,j} \left(1 - Q_d^{(j)}(\lambda_{g,j}, \boldsymbol{\omega}^{(j)})\right). \quad (37)$$

Similar with the detection in single channel, one of our objectives is to find the optimal thresholds $\boldsymbol{\lambda}_{gj}$ and weight vectors $\boldsymbol{\omega}^{(j)}$ for $j$=1, 2,…, $L$ in the $L$ sub-bands in order to collectively minimize the total interference to PU subject to the constraint that guarantees the communication throughput and spectrum utilization of the CR in each sub-channel. As such, the optimal problem of cooperative detection in multi-channel can be formulated as

$$\begin{aligned} &\min_{\boldsymbol{\lambda}_g, \boldsymbol{\omega}^{(j)}} R_I \\ &s.t.\ R_C \geq \varepsilon \\ &\boldsymbol{Q}_f(\boldsymbol{\lambda}_g, \boldsymbol{\omega}^{(j)}) \leq \boldsymbol{\alpha} \\ &\boldsymbol{Q}_d(\boldsymbol{\lambda}_g, \boldsymbol{\omega}^{(j)}) \geq \boldsymbol{\beta} \end{aligned} , \quad (38)$$

where $\varepsilon$, $\boldsymbol{\alpha} = [\alpha_1, \alpha_2, ..., \alpha_L]$ and $\boldsymbol{\beta} = [\beta_1, \beta_2, ..., \beta_L]$ are respectively the constraints of the throughput and probabilities of false alarm and detection.

The objective function and constraints in (38) are the non-convex functions with double parameters and nonlinear constraints, and therefore, the optimal problem in (38) is usually NP-hard to be solved directly. In order to solve the problem in (38), we resort to transformation of the problem into a sub-problem with low complexity, in which the conclusions obtained in Section 3 are also used.

According to (26), by choosing $\boldsymbol{\omega}^{(j)}$ as the optimal weight vector, we can define $R_I$ by $Q_f^{(j)}$ as (27). Since $Q_d^{(j)}$ increases with the increasing of $Q_f^{(j)}$, $R_I$ can reach the minimum when $R_C$ reaches its lower band. Since there is the only $Q_f^{(j)}$ corresponding to the given $\lambda_{g,j}$ and $\boldsymbol{\omega}^{(j)}$, the optimal solution of $\lambda_g$ can be substituted by optimizing $\boldsymbol{Q}_f$.

Therefore the optimal problem of (38) can be further modified as follows

$$\min_{\mathbf{Q}_f} \sum_{j=1}^{L} C_{1,j}\left(1-Q\left(\frac{Q^{-1}(Q_f^{(j)})}{\sqrt{1+2\overline{\gamma}_j}}-\sqrt{\frac{M\theta_j}{2}}\right)\right)$$

$$s.t.\quad \sum_{j=1}^{L} C_{0,j}Q_f^{(j)} = \sum_{j=1}^{L} C_{0,j} - \varepsilon'/P_{H_0}$$

$$Q\left(Q^{-1}(\beta_j)\sqrt{1+2\overline{\gamma}_j}+\sqrt{(0.5+\overline{\gamma}_j)M\theta_j}\right) \le Q_f^{(j)} \le \alpha_j \quad (39)$$

where the lower band of communication throughput $\varepsilon' = \max\left(\varepsilon, P_{H_0}\sum_{j=1}^{L} C_{0,j}(1-\alpha_j)\right)$ which denotes that if $\varepsilon \ge P_{H_0}\sum_{j=1}^{L} C_{0,j}(1-\alpha_j)$ , $\varepsilon' = \varepsilon$ and otherwise $\varepsilon' = P_{H_0}\sum_{j=1}^{L} C_{0,j}(1-\alpha_j)$ . The average SNR of the channel $j$ is $\overline{\gamma}_j = \sum_{i=1}^{N}\gamma_{ij}/N$ . The substituted variable $\theta_j = \sum_{i=1}^{N}\gamma_{ij}^2/\left(1+2\gamma_{ij}\right)$.

In this way, the original nonlinear constraints are transformed into the linear constraints, and the optimal global thresholds can be obtained by $\boldsymbol{Q}_f$ through (13). In order to solve the optimal problem in (39), firstly, we must prove that the objective function is convex in $\boldsymbol{Q}_f$ , and in order to prove this problem, we define

$$s_j(Q_f^{(j)}) = 1-Q\left(\frac{Q^{-1}(Q_f^{(j)})}{\sqrt{1+2\overline{\gamma}_j}}-\sqrt{\frac{M\theta_j}{2}}\right), \quad (40)$$

and the objective function can be defined as

$$S(\boldsymbol{Q}_f) = \sum_{j=1}^{L} C_{1,j}s_j(Q_f^{(j)}). \quad (41)$$

**Lemma 1:** Subject to the conditions $\boldsymbol{\alpha} < 0.5$ and $\boldsymbol{\beta} > 0.5$ , the function $s_j(Q_f^{(j)})$ is convex in $Q_f^{(j)}$ .

Proof: Let $Q^{-1}(Q_f^{(j)}) = \tau_j$ , and according to (40) it is obtained that $Q_f^{(j)} = Q(\tau_j)$ and $s_j(Q_f^{(j)}) = 1 - Q\left(\tau_j/\sqrt{1+2\overline{\gamma}_j}-\sqrt{0.5M\theta_j}\right)$. By taking the second derivative of $Q_f^{(j)}$ and $s_j(Q_f^{(j)})$ in $\tau_j$ , we can obtain

$$\frac{\partial^2 Q_f^{(j)}}{\partial^2\tau_j} = \frac{\tau_j}{\sqrt{2\pi}}\exp\left(-\frac{\tau_j^2}{2}\right), \quad (42)$$

$$\frac{\partial^2 s_j(Q_f^{(j)})}{\partial^2\tau_j} = -\frac{\tau_j-\sqrt{(0.5+\overline{\gamma}_j)M\theta_j}}{\sqrt{2\pi}(1+2\overline{\gamma}_j)^{3/2}}\times \exp\left(-0.5\left(\frac{\tau_j}{\sqrt{1+2\overline{\gamma}_j}}-\sqrt{0.5M\theta_j}\right)^2\right). \quad (43)$$

According to the inequality constraint of (39), the range of $\tau_j$ is obtained by

$$Q^{-1}(\alpha_j) \le \tau_j \le Q^{-1}(\beta_j)\sqrt{1+2\overline{\gamma}_j} + \sqrt{(0.5+\overline{\gamma}_j)M\theta_j}. \quad (44)$$

Since $\alpha_j < 0.5$ , we get $\tau_j > 0$ and $\partial^2 Q_f^{(j)}/\partial^2\tau_j > 0$ . According to (42-43), while $\beta_j > 0.5$ , we can have that $\tau_j < \sqrt{(0.5+\overline{\gamma}_j)M\theta_j}$ and $\partial^2 s_j(Q_f^{(j)})/\partial^2\tau_j > 0$ . Finally we can obtain

$$\frac{\partial^2 s_j(Q_f^{(j)})}{\partial^2 Q_f^{(j)}} = \frac{\partial^2 s_j(Q_f^{(j)})}{\partial^2\tau_j}\Big/\frac{\partial^2 Q_f^{(j)}}{\partial^2\tau_j} > 0, \quad (45)$$

which implies that $s_j(Q_f^{(j)})$ is convex in $Q_f^{(j)}$ .

**Lemma 2**: The objective function $S(\boldsymbol{Q}_f)$ is also convex in $\boldsymbol{Q}_f$.

Proof: By supposing that both the two vectors $\boldsymbol{Q}_{fa} = [Q_{fa}^{(1)}, Q_{fa}^{(2)}, ..., Q_{fa}^{(L)}]$ and $\boldsymbol{Q}_{fb} = [Q_{fb}^{(1)}, Q_{fb}^{(2)}, ..., Q_{fb}^{(L)}]$ satisfy the linear constraints of (39), for any $\zeta \in [0, 1]$ , we define that

$$\boldsymbol{Q}_{fc} = \zeta\boldsymbol{Q}_{fa} + (1-\zeta)\boldsymbol{Q}_{fb}, \quad (46)$$

where the vector $\boldsymbol{Q}_{fc} = [Q_{fc}^{(1)}, Q_{fc}^{(2)}, ..., Q_{fc}^{(L)}]$ . It is easy to know that $\boldsymbol{Q}_{fc}$ also satisfies the constraints of (39). Since according to Lemma 1, $s_j(Q_f^{(j)})$ is convex in $Q_f^{(j)}$ , it can be obtained that

$$s_j\left(Q_{fc}^{(j)}\right) = s_j\left(\zeta Q_{fa}^{(j)} + (1-\zeta)Q_{fb}^{(j)}\right) \le \zeta s_j(Q_{fa}^{(j)}) + (1-\zeta)s_j(Q_{fb}^{(j)}). \quad (47)$$

By substituting (47) into (41), we have

$$S(\boldsymbol{Q}_{fc}) = \sum_{j=1}^{L} C_{1,j}s_j(Q_{fc}^{(j)}) \le \zeta\sum_{j=1}^{L} C_{1,j}s_j(Q_{fa}^{(j)}) + (1-\zeta)\sum_{j=1}^{L} C_{1,j}s_j(Q_{fb}^{(j)}), \quad (48)$$
$$= \zeta S(\boldsymbol{Q}_{fa}) + (1-\zeta)S(\boldsymbol{Q}_{fb})$$

which means that function $S(\boldsymbol{Q}_f)$ is convex in $\boldsymbol{Q}_f$.

So the optimal problem (39) takes the form of minimizing a convex function subject to the linear constraints, and thus a local optimum is also the global optimum. Efficient numerical search algorithms such as the Graded Newton method can be used to find the optimal solution. In this subsection, the non-convex optimal problem with double parameters and nonlinear constraints is transformed into a convex optimal problem with single parameter and linear constraints, which can be solved easily.

### B. Maximizing throughput

Alternatively, we can formulate the cooperative detection in multi-channel into another optimization problem that maximizes the throughput of CR subject to the constraint of the interference to PU. This optimal problem is defined as follows

$$\begin{aligned} &\max_{\boldsymbol{\lambda}_g,\boldsymbol{\omega}^{(j)}} R_C \\ s.t.\quad & R_I \le \xi \\ & \boldsymbol{Q}_f(\boldsymbol{\lambda}_g,\boldsymbol{\omega}^{(j)}) \le \boldsymbol{\alpha} \\ & \boldsymbol{Q}_d(\boldsymbol{\lambda}_g,\boldsymbol{\omega}^{(j)}) \ge \boldsymbol{\beta} \end{aligned} . \tag{49}$$

For getting the sub-problem of (49), the weighed factors obtained by (33) are adopted, and $R_I$ can be denoted by $\boldsymbol{Q}_d$ according to (34). By transforming the objective function into the minimal problem, similar with (39), the optimal problem of (49) can be modified as

$$\begin{aligned} &\min_{\boldsymbol{Q}_d} \sum_{j=1}^{L} C_{0,j} Q\left( Q^{-1}(Q_d^{(j)})\sqrt{1+2\overline{\gamma}_j} + \sqrt{\frac{M\varphi_j}{2}} \right) \\ &s.t.\quad \sum_{j=1}^{L} C_{1,j} Q_d^{(j)} = \sum_{j=1}^{L} C_{1,j} - \xi'/P_{H_1} \\ &\beta_j \le Q_d^{(j)} \le Q\left( \frac{Q^{-1}(\alpha_j) - \sqrt{0.5M\varphi_j}}{\sqrt{1+2\overline{\gamma}_j}} \right) \end{aligned} , \tag{50}$$

where the upper band of the interference capacity $\xi' = \min\left(P_{H_1}\sum_{j=1}^{L} C_{1,j}(1-\beta_j), \xi\right)$ which denotes that if $\xi \le P_{H_1}\sum_{j=1}^{L} C_{1,j}(1-\beta_j)$ , $\xi' = \xi$ and otherwise $\xi' = P_{H_1}\sum_{j=1}^{L} C_{1,j}(1-\beta_j)$ . The substituted variable $\varphi_j = \sum_{i=1}^{N} \gamma_{ij}^2$ .

The optimal problem of (50) is also a convex optimal problem with single parameter and linear constraints, which can be proved to have solution similar with Lemma 1 and 2. The global detection threshold $\boldsymbol{\lambda}_g$ can be obtained by $\boldsymbol{Q}_d$ through (14).

## V. SIMULATION AND ANALYSIS

### A. Simulation of detection in single channel

In this subsection, we numerically evaluate the proposed weighed cooperative detection based on data fusion. Consider the single channel used by the PU, and the achievable rates $C_0 = 10$kbps and $C_1 = 5$kbps in the primary channel. There are $N$=5 CRs in the network, and their SNRs are $\boldsymbol{\gamma}$ = [-15, -10, -8, -5, -3] dB. The number of the sampling nodes $M$=100, and the hypothesis probabilities satisfy $P_{H_0} = P_{H_1} = 0.5$ . The sensing channel and reporting channel obey Rayleigh distribution.

Figures 5 and 6, respectively, illustrate the interference capacity and communication throughput of the three cooperative detection algorithms: the proposed weighed algorithm based on minimizing interference or maximizing throughput, the algorithm without weighing and the weighed algorithm based SNR. From Fig. 5, we can see that the proposed weighed algorithm based on minimizing interference can achieve lower interference than the other two subject to the constraint on the communication throughput. While communication throughput $R_C$ improves, the interference capacity $R_I$ also increases, that is because the probability $Q_d$ can decrease with the decreasing of $Q_f$ .

Figure 6 shows that the proposed weighed algorithm based on maximizing throughput also achieves higher communication throughput than the other two subject to the constraint on the interference capacity. While the interference capacity increases, the communication throughput also improves, and therefore there is a conflict between improving throughput and decreasing interference. So the limit probabilities of false

alarm and detection should be chosen appropriately according to the requirement of CR.

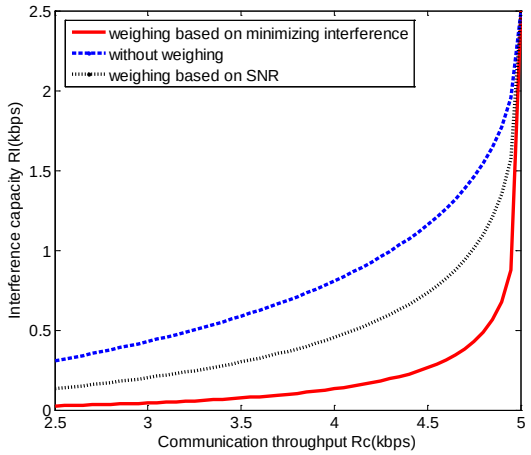


Fig. 5. Interference capacity $R_I$ versus communication throughput $R_C$.

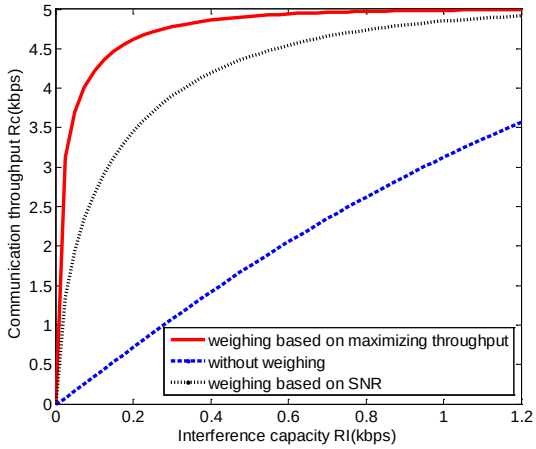


Fig. 6. Communication throughput $R_C$ versus interference capacity $R_I$.

Figures 7 and 8, respectively, reflect the interference capacity and communication throughput of the three algorithms versus the average channel gain between CRs and the fusion center. Here, the channel gains obey random Rayleigh distribution, and the average channel gain which is given by $g = \sum_{i=1}^{N} g_i / N$ increases from 0dB to 10dB. The proposed algorithm cannot be affected by the channel gain, while the other two have the obvious fluctuation with the changing of the channel gain. In addition, compared to the other algorithms, the proposed weighed algorithm based on minimizing interference always keeps the lower interference capacity, while the proposed weighed algorithm based on maximizing throughput always keeps higher communication throughput. That is because, according to (26) and (33), the weighed factors obtained by the proposed algorithm satisfy $\omega_i \sim 1/g_i$ for $i$=1, 2,…, $N$, and the larger factor can be allocated to the CR with lower channel gain in order to compensate the sensing loss brought by the channel fading.

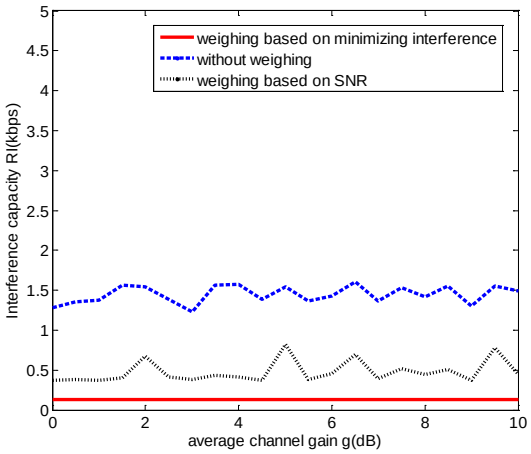


Fig. 7. Interference capacity $R_I$ versus the average channel gain $g$ from CRs to fusion center.

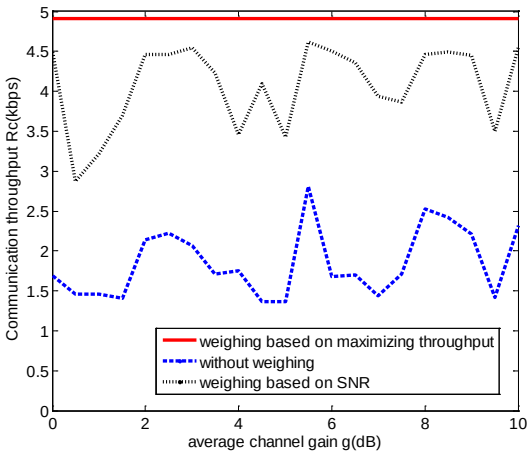


Fig. 8. Communication throughput $R_C$ versus the average channel gain $g$ from CRs to fusion center.

### B. Simulation of detection in multi-channel

In this section, the performance of the proposed cooperative detection in multi-channel is analyzed. We assume that there is $L$=5 sub-channels, and the average SNRs of these channels are $\bar{\gamma}$ =[-15,-13,-12,-10,-8] dB. The CR rates in $L$ sub-channels are $\boldsymbol{C}_0$ =[12, 10, 8, 6, 4] and $\boldsymbol{C}_1$ = [6, 4, 3, 2, 1]， and the upper band of probability of

false alarm and the lower band of probability of detection are $\alpha = 0.4$ and $\beta = 0.6$ respectively.

Figure 9 illustrates the comparative interference capacity $R_I$ of the proposed multi-channel cooperative detection based on (39), the weighed algorithm with the uniform threshold and the weighed factors obtained by (26), and the algorithm with uniform threshold but without weighing versus the communication throughput $R_C$. Differing from the uniform threshold adopted by the other two algorithms, the optimal thresholds shown in Fig. 10 which are different and adaptive to the status change of the sub-channels (channel with higher SNR has larger threshold), are adopted by the proposed algorithm, and therefore the proposed algorithm which can produce lower interference to the PU, can make better use of the wide frequency band by balancing the conflict between improving spectral utilization and decreasing interference.

Figures 11 and 12, respectively, show the probabilities of false alarm and detection of each sub-channel in the proposed algorithm and the weighed algorithm with uniform threshold when $R_C = 13.2$kbps . Obviously, the proposed algorithm can keep the sensing probabilities within the limits, and the probabilities of false alarm are all below 0.4 while the probabilities of detection are all above 0.6. However in the weighed algorithm with uniform threshold, the probabilities of false alarm are higher in some channels, while the probabilities of detection are lower in the other channels, and only the sensing probabilities of channel 3 satisfy the limits.

Figure 13 illustrates the comparative communication throughput $R_C$ of the proposed multi-channel cooperative detection based on (50), the weighed algorithm with the uniform threshold and the weighed factors obtained by (33), and the algorithm with uniform threshold but without weighing versus the interference capacity $R_I$. From this figure we can see that the proposed algorithm can achieve higher throughput than the other two.

From Figs. 14 and 15, we can see that similar with the optimal problem of (39), the optimal sub-channel probabilities of false alarm and detection obtained by (50) can respectively keep below 0.4 and above 0.6, when $R_I = 2.4$kbps . Compared to the probabilities in Figs. 11 and 12, in order to improve the throughput, the probabilities of false alarm are decreased, however, the probabilities of detection are synchronously decreased and therefore, the interference to PU is increased. That is, the conflict between improving throughput and decreasing interference is ineluctable.

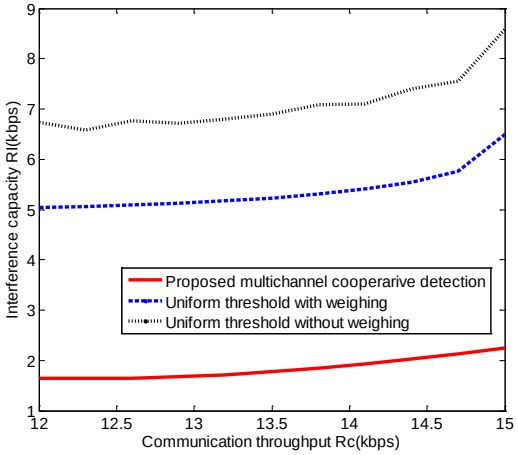


Fig. 9. Interference capacity $R_I$ versus communication throughput $R_C$.

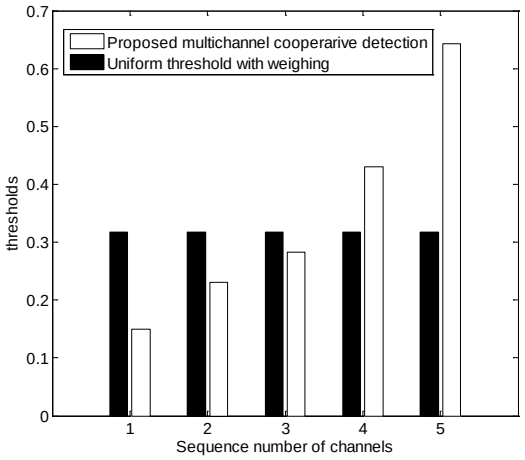


Fig. 10. Threshold of each sub-channel.

We illustrate the computational complexity of the proposed multi-channel cooperative detection. The number of iterations to reach the optimal solution is taken as the measure of complexity. Figure 16 shows the computational complexity versus the number of CRs $N$ when the number of channels $L$=10, while Fig. 17 shows the computational complexity versus different $L$ when $N$=10. We can see that compared to the conventional non-convex optimization scheme with double parameters, the computational complexity of the proposed scheme is much lower.

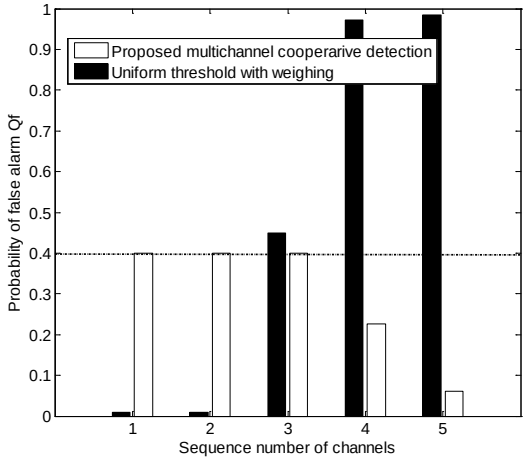


Fig. 11. Probability of false alarm in each sub-channel.

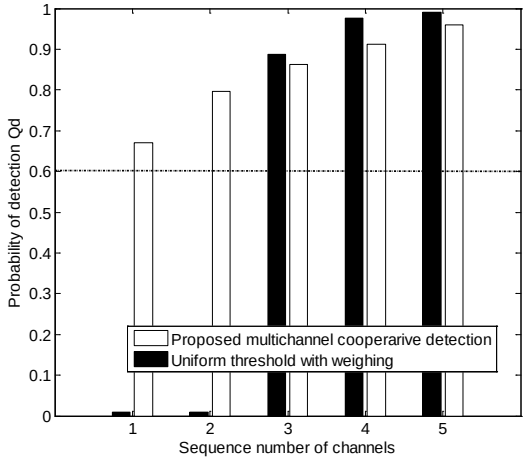


Fig. 12. Probability of detection in each sub-channel.

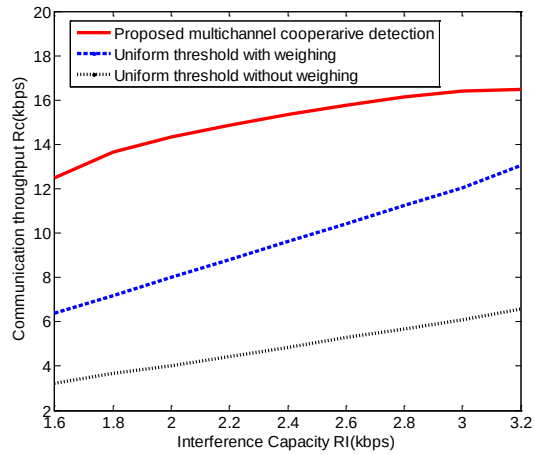


Fig. 13. Communication throughput $R_C$ versus interference capacity $R_I$.

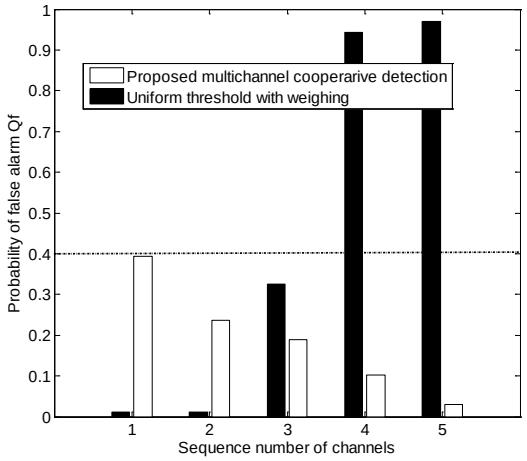


Fig. 14. Probability of false alarm in each sub-channel.

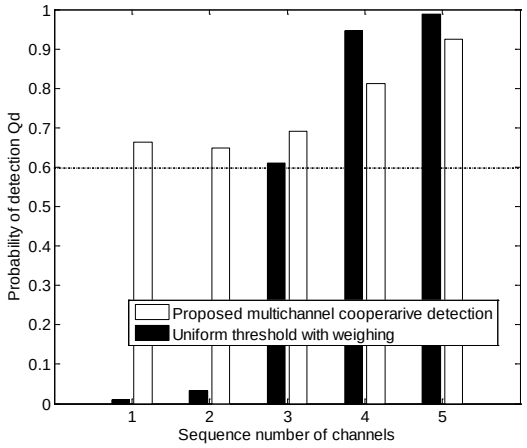


Fig. 15. Probability of detection in each sub-channel.

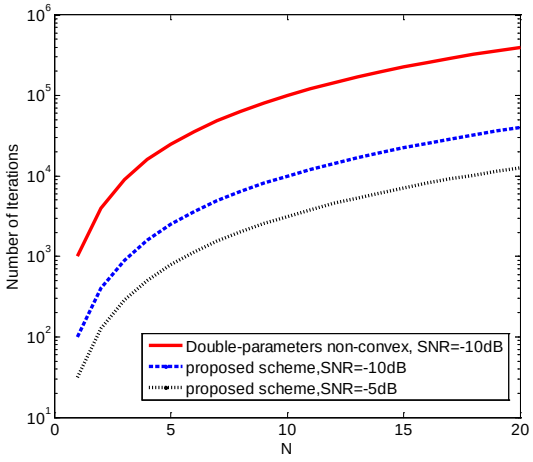


Fig. 16. Number of iterations versus the number of CRs $N$.

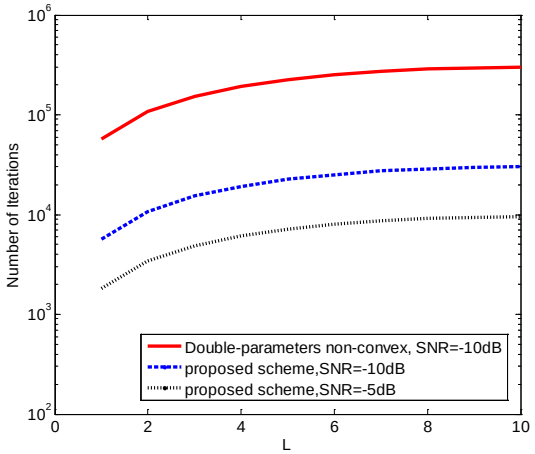


Fig. 17. Number of iterations versus the number of the sub-channels *L*.

## VI. CONCLUSION

In this paper, we have explored both the optimal cooperative spectrum sensing strategies for cognitive radio networks in single channel and multi-channel. We have studied the problem how to choose the optimal weighed factors to minimize interference and maximize throughput in the weighed cooperative detection model based on data fusion. We obtain the optimal weighed factors of the single-channel cooperative detection by the Cauchy-inequality, and by the research results of the single-channel cooperative detection, we have transformed the non-convex optimal problem of multi-channel cooperative detection with double parameters and nonlinear constraints into the convex optimal problem with single parameter and linear constraints, which can be solved easily.

In our algorithm, the weighed factors are proportional to the received SNRs by CRs and inversely proportional to the channel gains between CRs and the fusion center. Therefore compared to the conventional weighed algorithm, the proposed algorithm can allocate a larger weighed factor to the CR with higher SNR and lower gain in order to increase its decision strength in the cooperative detection and compensate the lost information brought by the channel fading. By the obtained weighing, the sensing performance of the cooperative detection can be improved greatly.

The simulation shows that there is a conflict between improving throughput and decreasing interference, however, the proposed algorithm can make better use of spectrum by balancing the conflict. The proposed algorithm can also keep the probabilities of false alarm and detection within the limits in order to guarantee the effective utilization of each sub-channel. In this paper, from the two aspects: minimizing interference and maximizing throughput, we develop our problems, however, these two aspects are conflictive and contrary, so how to find the uniform weighing to obtain a better tradeoff between the two aspects is an interesting research topic for further investigation.

## ACKNOWLEDGMENT

This paper is supported by National Natural Science Foundation of China (61071104). It also gets the supports of Communication Research Center of Harbin Institute of Technology.

## REFERENCE

[1] FCC. "B Spectrum Policy Task Force," *ET Docket 02–135*, Nov. 2002.

[2] M. McHenry, E. Livsics, T. Nguyen, and N. Majumdar. "BXG Dynamic Spectrum Accessfield Test Results," I*EEE Communication Magazine*, vol. 45, pp. 51–57, Jun. 2007.

[3] Krenik W. and Batra A. "Cognitive Radio Techniques for Wide Area Networks," *Design Automation Conference*, California, USA, pp. 409-412, June 2005.

[4] Joseph Mitola, G. Q. Maguire. "Cognitive Radio: Making Software Radios More Personal," *IEEE Person Communication*, vol. 6, no. 4, pp. 13–18, Aug. 1999.

[5] I. F. Akyildiz, W. Y. Lee, M. C. Vuran, and S. Mohanty, "BNext Generation/Dynamic Spectrum Access/Cognitive Radio Wireless Networks: A Survey," *Comput. Netw*., vol. 50, pp. 2127–2159, 2006.

[6] K. B. Letaief and W. Zhang. "Cooperative Communications for Cognitive Radio Networks," *Proceedings of the IEEE*, vol. 97, no. 5, pp. 878–893, May 2009.

[7] B. Shen, L. Huang, et al., "Energy Detection Based Spectrum Sensing for Cognitive Radios in Noise of Uncertain Power," i*n Proc. International Symposium on Communications and Information Technologies*, (ISCIT), Vientiane, Laos, pp. 628–633, October 2008.

[8] J. Shen, S. Liu, and et al. "Soft Versus Hard Cooperative Energy Detection under Low SNR," *in proc. Communications and Networking in China*, (Chinacom), pp. 128–131, 2008.

[9] J. Duan and Y. Li. "Performance Analysis of Cooperative Spectrum Sensing in Different Fading

Channels," *Proc. International Conference on Computer Engineering and Technology, (ICCET)*, vol. 3, pp. 364–368, April 2010.

[10] J. N. Laneman, D. N. C. Tse, G. W. Wornell. "Cooperative Diversity in Wireless Networks: Efficient Protocols and Outage Behavior," *IEEE Trans. Inf. Theory*, vol. 50, pp. 3062–3080, Dec. 2004.

[11] J. Ma, G. Zhao, and Y. Li. "Soft Combination and Detection for Cooperative Spectrum Sensing in Cognitive Radio Networks," *IEEE Transactions on Wireless Communications*, no.7, pp. 4502–4507, 2008.

[12] S. M. Mishra, A. Sahai, R. W. Brodersen, "Cooperative Sensing Among Cognitive Radios," *in Proc. Of IEEE International Conference on Communications* (ICC'06), vol. 4, pp. 1658–1663, June 2006.

[13] G. Taricco. "Optimization of Linear Cooperative Spectrum Sensing for Cognitive Radio Networks," *IEEE Journal on Selected Topics in Signal Processing*, vol. 5, no. 1, pp. 77–86, 2011.

[14] G. Xiong, S. Kishore, and A. Yener, "On Low Complexity Cooperative Spectrum Sensing for Cognitive Networks," *in Proc. IEEE Int. Workshop Comput. Adv. Multi-Sens.*, Aruba, Netherlands. pp. 145–148. December 2009.

[15] Z. Quan, S. Cui, et al., "Optimal Multiband Joint Detection for Spectrum Sensing in Cognitive Radio Networks," *IEEE Transactions on Signal Processing*, vol. 57, no. 3, pp. 1128–1140, 2009.

[16] Y. Yan, A. Li, and H. Kayama, "Study on Soft Decision based Cooperative Sensing in Cognitive Radio Network," *in Proc. Vehicular Technology Conference Fall* (VTC 2009-Fall), pp. 1–5, Sept. 2009.

[17] G. A. Ellis, "Wireless Propagation in Non Line of Sight Urban Areas using Uniform Theory of Diffraction," *Applied Computational Electromagnetic Society (ACES) Journal*, vol. 18, no. 3, pp. 162 – 171, November 2003.

Xin Liu: (1984-), born in China, received Bachelor and Master in Harbin Institute of technology. Now he is reading for his Ph.D. in Harbin Institute of Technology. His research is on signal processing, cognitive radio.

Xuezhi Tan: (1957-), born in China, and received his Bachelor, Master, and Ph.D. in Harbin Institute of Technology. Now his is a professor of Harbin Institute of Technology. His research is on cognitive radio, personal communication. He is also an IEEE member.

# Accelerating the Multilevel Fast Multipole Method with Parallel Preconditioner for Large-Scale Scattering Problems

**Ming Chen, Rushan Chen, Zhenhong Fan, and Dazhi Ding**

Department of Communication Engineering
Nanjing University of Science and Technology
Nanjing, P.R. China, 210094
eechenrs@mail.njust.edu.cn

***Abstract*—** A novel parallel framework is proposed for the iterative solution of the multilevel fast multipole method (MLFMM). The inversion of the near-field impedance matrix is used as the preconditioner matrix to improve the convergence history of the ill-conditioned linear system formulated by electric field integral equation. In order to accelerate the inversion of the near field impedance matrix with huge number of unknowns, the parallel technique is used to construct the preconditioner matrix. Our numerical experiments reveal that with an efficiently parallelized MLFMM and the effective parallel preconditioner, we are able to solve problems with millions of unknowns in a few hours. Both the number of iteration steps and the overall simulation time can be saved significantly. For closed-surface problems analyzed by the combined-field integral equation, the number of iterations can also be reduced significantly by the proposed method. Numerical results are presented to demonstrate the accuracy and efficiency of the proposed method.

***Index Terms*—** Multilevel fast multipole method, preconditioning, scattering problems.

## I. INTRODUCTION

The method of moments (MoM) [1-4] has found widespread application in a variety of electromagnetic radiation and scattering problems. The matrix associated with the resulting linear systems is large and dense for electrically large objects in electromagnetic scattering. It is basically impractical to solve the electric-field integral equation (EFIE) matrix equation using the direct method due to the memory requirement of $O(N^2)$ and computational complexity of $O(N^3)$, where $N$ is the number of unknowns. Making such solutions prohibitively expensive for large-scale problems, this difficulty can be circumvented by use of iterative solvers, and the matrix-vector product operation can be efficiently computed by the multilevel fast multipole method (MLFMM) [5-9]. The use of MLFMM reduces both the memory requirement and the computational complexity to *O(NlogN)*.

Although the MLFMM reduces the complexity of MoM from $O(N^2)$ to $O(N\log N)$, allowing for the solution of large problems with limited computational resources. However, accurate solutions of large problems require discretizations with millions of unknowns, which cannot easily be solved with sequential implementations of MLFMM running on a single processor. To solve such large problems, it is helpful to increase the computational resource by assembling parallel computing platforms and, at the same time, by paralleling MLFMM [10-14]. There are many efforts that have been done to improve the efficiency of the parallel MLFMM. Thanks to those efforts, it has become possible to solve millions of unknowns on relatively inexpensive platforms.

Among integral formulations, the application of boundary conditions for the electric field and the magnetic field on the surface of the object leads to the EFIE and the magnetic-field integral equation (MFIE), respectively. For closed object, EFIE and MFIE can be combined together to form the combined-field integral equation (CFIE), which provides better-conditioned matrix equations than EFIE and MFIE and is free of internal-resonance. However, for the open structure only EFIE can be used, the EFIE provides a first-kind Fredholm integral equation, which is usually ill-conditioned,

*Submitted On: June 15, 2011*
*Accepted On: September 12, 2011*

this is especially true when the higher-order basis functions are employed, which will drastically increase the condition number of the EFIE matrix. Generally, it requires a large number of iterations to reach convergence. This bottleneck severely limits the capability of the MLFMM for open structure. To break this bottleneck, many preconditioner techniques [15-20] have been developed to accelerate the convergence rate, such as the diagonal, block-diagonal, but they are not effective enough to yield a highly efficient solution.

We know that, in the MLFMM application, only the near-field impedance matrix is stored, which is composed of the interactions of the neighboring cubes in the lowest level of the octree structure. The Green's function used for the computation of the matrix elements decays with 1/R, where R is the distance between the pair of basis and testing functions. Due to this rapid decay of the Green's function, basis functions that are close to each other are expected to have strong electromagnetic coupling, resulting in matrix elements with larger magnitudes. Therefore, the near-field impedance matrix retains the most relevant contributions of the impedance matrix in MoM. In this paper, we use the exact inversion of the near-field matrix as a preconditioner matrix in MLFMM. From the numerical results, we can see that the number of iterations reduced significantly compared with that without the preconditioner. Moreover, for conducting geometries with closed surfaces, the CFIE should be considered. Even though EFIE can also be used in such problems, this has no practical use since CFIE can solve the closed-surface problems much faster. Furthermore, from the numerical results, we can see that the preconditioner for the CFIE systems can also get higher efficiency.

The remainder of this paper is organized as follows. Section II gives a brief introduction to the EFIE and MFIE, together with an introduction of the MLFMM. The efficient parallization of MLFMM and the construct preconditioner matrix are also investigated in this part in detail. Section III presents the numerical results to demonstrate the accuracy and efficiency of the proposed method. Finally, some conclusions are given in section IV.

## II. THEORY

The EFIE and MFIE formulation of electromagnetic scattering problems using planar Rao-Wilton-Glisson (RWG) basis functions for surface modeling is presented in [1]. The resulting linear systems from EFIE and MFIE formulation after Galerkin's testing are briefly outlined as follows

$$\sum_{n=1}^{N} Z_{mn} a_n = V_m, \quad m = 1,2,...,N, \tag{1}$$

where

$$Z_{mn}^{EFIE} = \iint_{s_m} ds \iint_{s_n} ds' [\, j\omega\mu \boldsymbol{J}_m \bullet \boldsymbol{J}_n - \frac{j}{\omega\mu} (\nabla \bullet \boldsymbol{J}_m)\nabla' \bullet \boldsymbol{J}_n))] g(\boldsymbol{r}, \boldsymbol{r}'), \tag{2}$$

$$Z_{mn}^{MFIE} = \frac{1}{2}\iint_S \boldsymbol{J}_m \bullet \boldsymbol{J}_n dS - \iint_S \boldsymbol{J}_n \bullet \hat{n} \times \nabla \times \iint_{S'} G\boldsymbol{J}_m dS' dS, \tag{3}$$

and

$$V_m^{EFIE} = \iint_{s_m} \boldsymbol{J}_m \bullet \boldsymbol{E}^{inc} ds, \tag{4}$$

$$V_m^{MFIE} = \iint_{s_m} \boldsymbol{J}_m \bullet (n \times \boldsymbol{H}^{inc}) ds. \tag{5}$$

Here $g(\vec{r}, \vec{r}') = e^{-jk|\vec{r}-\vec{r}'|} / 4\pi \left|\vec{r} - \vec{r}'\right|$ refers to the Green's function in free space and $a_n$ are the coefficients of the induced current expanded in RWG basis functions, $\overline{V}$ is the vector of incident field. $r$ and $r'$ denote the observation and source point locations. $\boldsymbol{E}^{inc}$ and $\boldsymbol{H}^{inc}$ are the incident plane wave, $\eta$ and $k$ denote the free space impedance and wave number, respectively.

For closed structure, the CFIE is simply a linear combination of EFIE and MFIE and is of the form

$$Z^{CFIE} = \frac{\alpha}{\eta} Z^{EFIE} + (1-\alpha) Z^{MFIE}. \tag{6}$$

The combination parameter $\alpha$ ranges from 0 to 1 and can be chosen to be any value within this range.

From above we can see that, if we have discretization of equation (2) and (3) by MoM, we end up with a dense linear matrix. The surface of the object is in general meshed with $0.1\lambda$ of the wavelength for accuracy. Hence, for high frequencies where the electrical size of the object becomes large in terms of the wavelength, the system matrix becomes also large. When iterative methods are used to solve such systems, they can at best provide $O(N^2)$ complexity, which severely limit the capacity of the MoM in dealing with

large objects. Fortunately, a solution has been proposed to accelerate the computation of the MVP using the MLFMM for the MoM, which reduces the memory requirement and the computational complexity to $O(N\log N)$.

In MLFMM, the impedance matrix $\overline{\overline{Z}}$ can be split into two parts as

$$\overline{\overline{Z}} \cdot \bar{a} = \overline{\overline{Z}}_{NF} \cdot \bar{a} + \overline{\overline{Z}}_{FF} \cdot \bar{a}, \qquad (7)$$

where $\overline{\overline{Z}}_{NF}$ denotes the sparse matrix that corresponds to near-field interactions, while $\overline{\overline{Z}}_{FF}$ denotes the matrix that corresponds to far-field interactions. To calculate electromagnetic interactions by MLFMM in a multilevel scheme, a tree structure first needed to construct. The entire object is first enclosed into a large cube, and then the cube is partitioned into eight smaller cubes. Each subcube is recursively subdivided into eight smaller cubes until the finest cubes satisfy the termination criterion. After constructing an octree, we find nonempty cubes by sorting. Only nonempty cubes are recorded using tree-structured data at all levels. Thus, the tree structure is sparse. The computational cost depends on the nonempty cubes, not all cubes. Two cubes are well-separated if the ratio of the cube-center-distance to the cube size is greater than or equal to 2. The interaction between them can be computed in a group-by-group manner by MLFMM. Otherwise, they are near each other and share at least one edge point, the interaction between the two cubes can be calculated directly by MoM.

Although the MLFMM has reduced the complexity of the MoM from complexity $O(N^2)$ to $O(N\log N)$, allowing for the solution of large problems with limited computational resources. However, accurate solutions of large problems require discretizations with millions of unknowns, which cannot easily be solved with sequential implementations of MLFMM running on a single processor. Both the computation ability and the storage ability of a single computer can not afford. To solve such large problems, it is helpful to increase the computational resource by assembling parallel computing platforms and, at the same time, by paralleling MLFMM. Parallel MLFMM has received much attention in recent years with the development of the computer science; the bigger problems have been solved on the super computer. To improve the convergence rate of the equation (1) for the open structure, the parallel preconditioner for the parallel MLFMM was also constructed.

### A. Efficient parallelization of MLFMM

Because of the complicated structure, parallelization of MLFMM is not a trivial. Simple parallelization schemes usually lead to inefficient solutions due to dense communications and unbalanced distribution of the workload among processors. For high efficiency parallelization, several issues must be carefully considered to obtain an efficient parallelization of MLFMM.

In the past few years, a series of implementation tricks have been developed for efficiently parallelizing the MLFMM, these tricks are different, but the most important thing in those tricks in parallelizing MLFMM is load-balancing and minimizes the communications between the processors. This is achieved by using different partitioning strategies for the lower and higher levels of the tree structure. In the lower levels of the tree structure, there are many clusters with a small number of samples for the radiated and incoming fields. The number of cubes is much larger than the number of processors. Therefore, it is natural to distribute the cubes equally among processors. However, it is difficult to achieve good load-balancing in higher levels with this parallel approach, since the number of cubes in the coarse levels is small and the electric size of the cube is large, the far-field patterns is large. Therefore, in the coarse level, we adopt another parallel approach in the coarse levels; we replicate the cubes in every processor, but partition the far-field patterns equally among all processors as paper. Using this approach for the parallel MLFMM in the far-field, good load balancing can be achieved.

The interaction in MLFMM is classified into a near-field interaction and the far-field interaction. After distribute the cubes to each processor, the near-field interaction lists and the far-field interaction lists can be set up in a parallel way. The near-field interaction are calculated directly and stored in memory without any communication. For the far-field interaction in the MLFMM is transformed into three phases: called the aggregation, translation, and disaggregation stage.

***Aggregation stage*:** The far-field interaction begins with aggregating basis functions at the finest level to obtain the radiation pattern. Each processor

calculates and stores the radiation and receiving patterns of the basis and testing functions included in its local box. Then each processor shifting the radiation pattern to the center of the box in the second finest level, and finally interpolating the deficient radiation pattern to obtain the radiation pattern of the box in the second-finest level. This procedure repeats until the shared levels. In the shared levels, each box is assigned to the same processor. The far-field pattern of each box is distributed equally among processors. In the distributed levels, even though a local interpolation is used, some of the far-field patterns may locate in other processors. Therefore one-to-one communications are needed to get the required data.

***Translation stage:*** The translation stage is one of the most important stages in the parallelization MLFMM; since the cubes are distributed among the processors; one to one communications are required between the processors for the translation stage. To eliminate this overhead, each processor is loaded with extra cubes called the ghost cubes. For example, if cube $i$ at processor $a$ needed the far-field samples of cube $j$ at processor $b$, maybe another cube at processor $a$ also needed the far-field samples of cube $j$ at processor $b$, to reduce the communication between the processors; we allocate space for the cube $j$ at processor $a$. When the far-field samples of the cube $j$ is received by processor $a$, we store it at processor $a$, this ensure that the same data is not transferred more than once. In the shared levels, the far-field samples of each cube are distributed equally among the processors. Therefore, there is need no communication between the processors at the translation stage in the shared levels.

***Disaggregation stage:*** The disaggregation stage is generally the inverse of the aggregation stage; the incoming fields are calculated at the centre of each cube from the top of the tree structure to the lowest level using the interpolation and shift operations. Some of the samples obtained from the interpolation operation should be sent to other processors, this is because interpolation during the aggregation stage are performed using the inflated data prepared by one-to-one communications among the processors. Following an interpolation operation, some of the resulting data are used locally, while the rest are sent to other processors, similar to the communications during the translation stage.

### B. Novel preconditioner in MLFMM

For equation (1), there are two ways to solve it. One is the direct solver, and the other is the iterative solver. For large-scale problems, it is impractical to solve the matrix equation with a large number of unknowns using the direct solver because it has a memory requirement of $O(N^2)$. This difficulty can be circumvented by solving the matrix equation using the Krylov-sub-space iterative method, which requires the matrix-vector product (MVP) in each iteration step. In the past, several iterative methods, including the conjugate gradient (CG), the biconjugate gradient (BCG), the stabilized biconjugate gradient (BCGS), and the generalized minimal residual (GMRES) have been employed. The use of those methods reduce the memory requirement to $O(N)$. Iterative solutions of linear systems using Krylov-subspace methods make it possible to solve large-scale scientific problems with modest computing requirements. Effective parallelization of both the matrix-vector multiplication and the iterative solvers are possible, allowing even larger systems to be solved with cost-effective parallel computers.

Unfortunately, the MoM matrix based on EFIE is usually ill-conditioned and requires a large number of iterations to reach convergence. In order to speed up the convergence rate of the GMRES solution, preconditioning techniques are often used, such as the block-diagonal. The block-diagonal techniques can help to partially alleviate this difficulty, but they are not effective enough to yield a highly efficient solution. In this paper, we use the exact inverse of the near-field matrix as the precondition for the MLFMM, The preconditioner matrix is very easy to construct, which can be obtained from the near-field interaction matrix. Number results are presented to show the high effectiveness of the proposed preconditioner and fast convergence of the iterative solution.

From above, we have known that the impedance matrix can be split into two parts, where $\overline{\overline{Z}}_{NF}$ denotes the near-field interactions and $\overline{\overline{Z}}_{FF}$ denotes the far-field interactions, since $\overline{\overline{Z}}_{FF}$ is not readily available and $\overline{\overline{Z}}_{NF}$ retains the most relevant contributions of the impedance matrix, it is

customary to construct preconditioners from $\overline{\overline{Z}}_{NF}$ assuming it to be a good approximation to $\overline{\overline{Z}}$. Therefore, in this paper, we choose the preconditioning matrix $M = \overline{\overline{Z}}_{NF}$. We call this proposed preconditioner the NF_LU preconditioner method.

In order to speed up the convergence rate of the Kryloy iterative methods, the preconditioning matrix $M$ are employed to transform (5) into an equivalent form

$$M^{-1}Ax = M^{-1}b, \tag{8}$$

with $\tilde{A} = M^{-1}A$ and $\tilde{b} = M^{-1}b$, equation (8) can be written as the following form

$$\tilde{A}x = \tilde{b}. \tag{9}$$

$M^{-1}$ is a matrix for preconditioning the matrix $A$ from the left. The purpose of preconditioning is to make the condition number of the matrix $\tilde{A}$ better than the original matrix $A$. So the Kryloy iterative methods for the equation (9) can get a fast convergence.

For sequential implementations of MLFMM running on a single processor, the calculation of $M^{-1}$ can be obtained by the Umfpack strategy, However, for large-scale problems, the direct solver $M^{-1}$ may require prohibitive memory and the time used to construct the inverse matrix will be very long. Fortunately this cost can be alleviated by parallelization. With an efficient parallelization to compute the $M^{-1}$, problems that are discretized with tens of millions of unknowns are easily solved on a cluster of computers. In this paper, we use the parallel LU factorization to construct the preconditioner matrix $M^{-1}$, after decomposing the matrix $M$ in the form of $M = LU$, preconditioning operation is performed in each step by solving $LUv = w$, the preconditioning operation $v = M^{-1}w$ is computed by solving the linear system $LUv = w$ is performed in two distinct steps: solve $Lx = w$ and $Uv = x$ successively.

## III. NUMERICAL RESULTS

In this section, several numerical examples are presented to demonstrate the efficiency of the proposed method. We calculate the RCS of three conducting geometries, which are shown in Fig. 1-3. The first two geometries are open structures analyzed by EFIE while the third structure is a closed structure computed by CFIE. All experiments are performed on a 2-node cluster connected with an Infiniband network. Each node includes 8 cores and 48 GB of RAM. The resulting linear systems are solved by the restarted version of the GMRES solver with dimension of 30 and tolerance residual of $10^{-3}$.

First of all, the proposed method is used to the analysis scattering from a square PEC plane with length of 16m, the incident plane wave direction is fixed at $\theta_{inc} = 0^\circ$ and $\phi_{inc} = 0^\circ$, the scattering angle is fixed at $\theta_s = 0^\circ \sim 180^\circ$ and $\phi_s = 0^\circ$ are shown in Fig. 1. The computational information (the electric size of the plane; the number of unknowns; the number of iterations without NF_LU preconditioner; the number of iterations with NF_LU preconditioner) for this example is given in Table I. From this table, we can conclude that without preconditioner, EFIE solutions converge fast only for a small number of unknowns. The number of iteration increases quickly to reach convergence without a preconditioner when the number of unknown increases. Convergence fails at the 1000th iterations without preconditioner when the electric size of the plane is $128\lambda$; it can be found from Table I that the NF_LU solve all problems within reasonable iteration counts. Compared with iterative solution without preconditioner, the NF_LU preconditioned method decrease the number of iterations about 12 times.

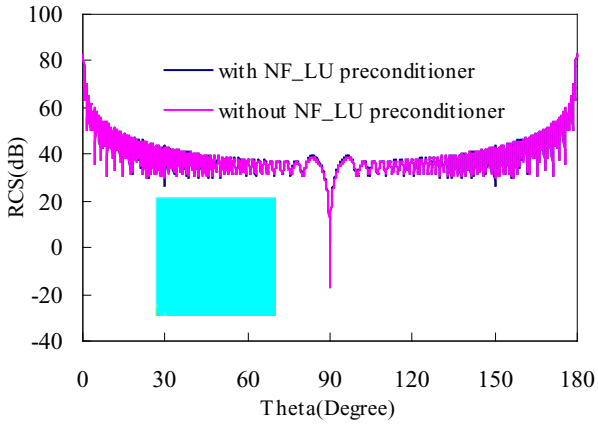


Fig. 1. Bistatic RCS of the conduct plane at 1.2 GHz.

The second example is the analysis of scattering from a half PEC sphere, the radius of the sphere is 8m. The incident direction of the plane wave are $\theta_{inc} = 0^\circ$ and $\phi_{inc} = 0^\circ$. The

scattering angle is observed at $\theta_s = 0^\circ \sim 180^\circ$, when $\phi_s = 0^\circ$ are shown in Fig. 2. The computational information for this example is given in Table II. As the electrical size of the half sphere is bigger than $32\lambda$, it can be seen from Table II that convergence fails without preconditioner since the number of iterations is larger than 1000. In contrast, with a NF_LU preconditioner, it is able to achieve convergence in 200 iterations when the electric size of the half sphere is $128\lambda$. Compared with traditional method without preconditioner, the NF_LU preconditioned method performs high efficiency in this example.

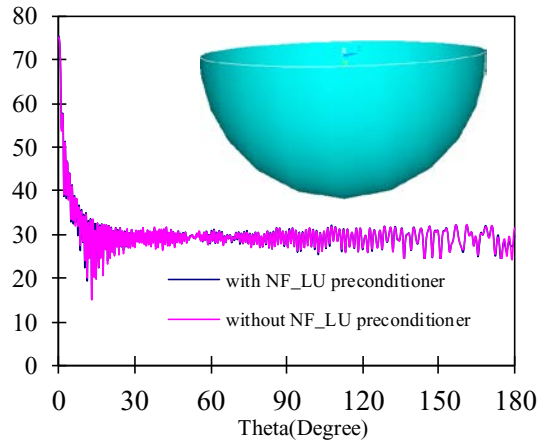


Fig. 2. Bistatic RCS in dB of the conduct half sphere at 1.2 GHz.

Table I: Performance comparison of no preconditioner and NF_LU preconditioner

| Frequency (GHz) | Unknowns | No preconditioner | NF_LU preconditioner |
|---|---|---|---|
| 0.3 | 85840 | 255 | 21 |
| 0.6 | 344000 | 352 | 30 |
| 1.2 | 1377280 | 645 | 41 |
| 2.4 | 5509120 | >1000 | 60 |

Table II: Performance comparison of no preconditioner and NF_LU preconditioner

| Frequency (GHz) | Unknowns | No preconditioner | NF_LU preconditioner |
|---|---|---|---|
| 0.3 | 78004 | 420 | 44 |
| 0.6 | 312016 | >1000 | 73 |
| 1.2 | 1248064 | >1000 | 117 |
| 2.4 | 5001952 | >1000 | 198 |

The last example is used to analyze scattering from a VFY-218 plane, since many real-life problems confronted in CEM involve complicated structures enclosing a volume. Due to its favorable properties, CFIE is the preferred integral-equation formulation for those targets with closed surfaces. The incident direction is fixed at $\theta_{inc} = 90$ and $\phi_{inc} = 90$. The scattering angles are $\theta_s = 90$ at $\phi_s = 0 \sim 360$ are shown in Fig. 3. The electric current on the surface of the plane is shown in Fig. 4. The computational information for this example is given in Table III. It can be seen from Table III that even for the CFIE matrix, the proposed preconditioner also performs a better efficiency.

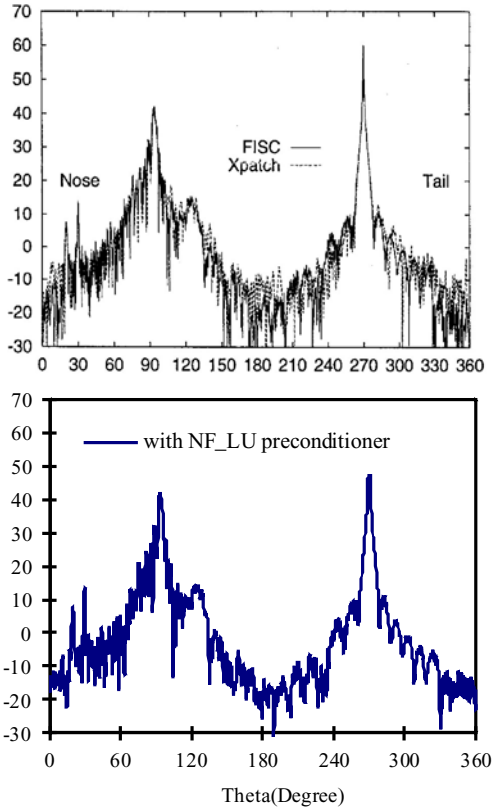


Fig. 3. Bistatic RCS in dB of the VFY-218 plane at 3GHz.

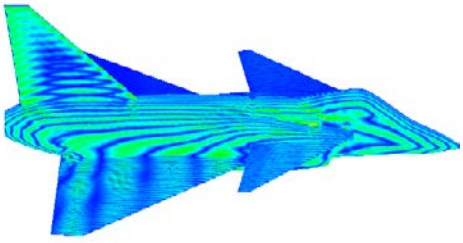

Fig. 4. Current distribution on the VFY-218 at 3GHz.

Table III: Performance comparison of no preconditioner and NF_LU preconditioner

| Frequency (GHz) | Unknowns | No preconditioner | NF_LU preconditioner |
|---|---|---|---|
| 0.35 | 34242 | 82 | 12 |
| 0.75 | 136968 | 76 | 15 |
| 1.5 | 547872 | 164 | 44 |
| 3.0 | 2191488 | 223 | 67 |

## IV. CONCLUSION

In this paper, we present the details of a hierarchical partitioning strategy for the efficient parallelization of MLFMM on distributed-memory architectures. The parallel NF_LU can accelerate the convergence of the GMRES iterative solver which is used for the solution of surface integral equations. From the numerical results, we can conclude that for the large open-surface problems that are analyzed by EFIE, the proposed preconditioner is more efficient and robust when compared with no preconditioner. For complex closed-surface problems that can make use of the well-conditioned CFIE, the proposed method is also very efficient.

## REFERENCES


[1] S. Rao, D. Wilton, and A. Glisson, "Electromagnetic Scattering by Surfaces of Arbitrary Shape," *IEEE Trans. Antennas and Propag.,* vol. 30, no. 3, pp. 409-418, May 1982.

[2] K. A. Michalski and D. L. Zheng, "Electromagnetic Scattering and Radiation by Surfaces of Arbitrary Shape in Layered media, Part I: Theory," *IEEE Trans. Antennas and Propag.*, vol. 38, no. 3, pp. 335-344, March 1990.

[3] K. A. Michalski and D. L. Zheng, "Electromagnetic Scattering and Radiation by Surfaces of Arbitrary Shape in Layered Media, Part II: Implementation and Results for Contiguous Half-Spaces," *IEEE Trans. Antennas and Propag.*, vol. 38, no. 3, pp. 345-352, 1990.

[4] D. Ding, J. Ge, and R. Chen, "Well-Conditioned CFIE for Scattering from Dielectric Coated Conducting Bodies above a Half-Space," *Applied Computational Electromagnetic Society (ACES) Journal*, vol. 25, no. 11, pp. 936 - 946, 2010.

[5] R. Coifman, V. Rokhlin, and S. M. Wandzura, "The Fast Multipole Method for the Wave Equation: A Pedestrian Prescription," *IEEE Trans. Antennas Propag.*, vol. 35, no. 3, pp. 7-12, 1993.

[6] J. M. Song, C. C. Lu., and W. C. Chew, "Multilevel Fast Multipole Algorithm for Electromagnetic Scattering by Large Complex Objects," *IEEE Trans. Antennas and Propag.*, vol. 45, no. 10, pp. 1488-1493, October 1997.

[7] C. C. Lu and W. C. Chew, "A Multilevel Algorithm for Solving Boundary Integral Equations of Wave Scattering," *Micro. Opt. Tech. Lett.*, vol. 7, pp. 466-470, July 1994.

[8] J. M. Song and W. C. Chew, "Multilevel Fast-Multipole Algorithm for Solving Combined Field Integral Equation of Electromagnetic Scattering," *Micro. Opt. Tech. Lett.,* vol. 10, pp. 14-19, September 1995.

[9] M. M. Li, H. Chen, C. Li, R. S. Chen, and C. Ong, "Hybrid UV/MLFMA Analysis of Scattering by PEC Targets above a Lossy Half-Space," *Applied Computational Electromagnetic Society (ACES) Journal*, vol. 26, no. 1, pp. 17-25, January 2011.

[10] H. Zhao, J. Hu, and Z. Nie, "Parallelization of MLFMA with Composite Load Partition Criteria and Asynchronous Communication," *Applied Computational Electromagnetic Society (ACES) Journal*, vol. 25, no. 2, pp. 167-173, 2010.

[11] H. Fangjing, N. Zaiping, and H. Jun, "An Efficient Parallel Multilevel Fast Multipole Algorithm for Large-scale Scattering Problems," *Applied Computational Electromagnetic Society (ACES) Journal*, vol. 25, no. 4, pp. 381-387, April 2010.

[12] K. C. Donepudi, J. M. Jin et al, "A Higher Order Parallelized Multilevel Fast Multipole Algorithm for 3-D Scattering," *IEEE Trans. Antennas and Propag.*, vol. 49, no. 7, pp. 1069-1078, July 2001.

[13] W. Rankin and J. Board. "A Potable Distributed Implementation of the Parallel Multipole Tree Algorithm," *IEEE Symp. on High Performance Distributed Computing*, pp. 17-22, 1995.

[14] X. M. Pan and X. Q. Sheng, "A Sophisticated Parallel MLFMM for Scattering by Extremely Large Targets," *IEEE Trans. Antennas and Propag.*, vol. 50, no. 3, pp. 129-138, June 2008.

[15] M. Grote and T. Huckle, "Parallel Preconditioning with Sparse Approximate Inverses," *SIAM J. Sci. Stat. Comput.,* vol. 18, pp. 838-853, 1997.

[16] E. Chow, "A Priori Sparsity Patterns for Parallel Sparse Approximate Inverse Preconditioners," *SIAM J. Sci. Comput.,* vol. 21, pp. 1804-1822, 2000.

[17] K. F. Tsang, R. S. Chen, M. Lei, and E. K. N. Yung, "Application of the Preconditioned Conjugate Gradient Algorithm to the Integral Equations for Microwave Circuits," *Micro. Opt. Tech. Lett.*, vol. 34 (4), pp. 266-270, 2002.

[18] K. Wang, S. Kim, and J. Zhang, "A Comparative Study on Dynamic and Static Scarcity Patterns in Parallel Sparse Approximate Inverse Preconditioning," *Journal of Mathematical Modeling and Algorithms*, vol. 2, no. 3, pp. 203-215, 2003.

[19] Z. N. Jiang, Z. H. Fan, D. Z. Ding, R. S. Chen, and K. W. Leung, "Preconditioned MDA-SVD-MLFMA for Analysis of Multi-scale Problems," *Applied Computational Electromagnetic Society (ACES) Journal*, vol. 25, no. 11, November 2010.

[20] J. Lee, J. Zhang, and C. Lu, "Performance of Preconditioned Krylov Iterative Methods for Solving Hybrid Integral Equations in Electromagnetics," *Applied Computational Electromagnetic Society (ACES) Journal,* vol. 18, no. 3, pp. 54-61, November 2003.

**Ming Chen** was born in Anhui, China. He received the B.S. degree in Physics from Anhui University in 2006, and is currently working toward the Ph.D. degree at Nanjing University of Science and Technology (NJUST), Nanjing, China. His current research interests include computational electromagnetics, antennas, and electromagnetic scattering and propagation.

**Ru-Shan Chen** was born in Jiangsu, P. R. China. He received his B.Sc. and M.Sc. degrees from the Dept. of Radio Engineering, Southeast University, in 1987 and in 1990, respectively, and his Ph.D. from the Dept. of Electronic Engineering, City University of Hong Kong in 2001. He became a Teaching Assistant in 1990 and a Lecturer in 1992. Since September 1996, he has been a Visiting Scholar with the Department of Electronic Engineering, City University of Hong Kong, first as Research Associate, then as a Senior Research Associate in July 1997, a Research Fellow in April 1998, and a Senior Research Fellow in 1999. From June to September 1999, he was also a Visiting Scholar at Montreal University, Canada. In September 1999, he was promoted to Full Professor and Associate Director of the Microwave & Communication Research Center and in 2007, he was appointed Head of the Dept of Communication Engineering, Nanjing University of Science & Technology (NJUST). His research interests mainly include microwave/millimeter-wave systems, measurements, antenna, RF-integrated circuits, and computational electromagnetics. He is a Senior Member of the Chinese Institute of Electronics (CIE). He received the 1992 third-class science and technology advance prize given by the National Military Industry Department of China, the 1993 third class science and technology advance prize given by the National Education Committee of China, the 1996 second-class science and technology advance prize given by the National Education Committee of China, and the 1999 first-class science and technology advance prize given by JiangSu Province as well as the 2001 second-class science and technology advance prize. At NUST, he was awarded the Excellent Honor Prize for academic achievement in 1994, 1996, 1997, 1999, 2000, 2001, 2002, and 2003. He has authored or co-authored more than 200 papers, including over 140 papers in international journals. He is the recipient of the Foundation for China Distinguished Young Investigators presented by the National Science Foundation (NSF) of China in 2003. In 2008, he became a Chang-Jiang Professor under the Cheung Kong Scholar Program awarded by the Ministry of Education, China.

**Zhen-Hong Fan** was born in Jiangsu, the People's Republic of China in 1978. He received the M.Sc. and Ph.D. degrees in Electromagnetic Field and Microwave Technique from Nanjing University of Science and Technology (NJUST), Nanjing, China, in 2003 and 2007, respectively. During 2006, he was with the Center of Wireless Communication in the City University of Hong Kong, Kowloon, as a Research Assistant. He is currently an associated Professor with the Electronic Engineering of NJUST. He is the author or coauthor of over 20 technical papers. His current research interests include computational electromagnetics, electromagnetic scattering and radiation.

**Dazhi Ding** was born in Jiangsu, the People's Republic of China. He received the B.S. and Ph.D. degrees in Electromagnetic Field and Microwave Technique from Nanjing University of Science and Technology (NJUST), Nanjing, China, in 2002 and 2007, respectively. During 2005, he was with the Center of Wireless Communication in the City University of Hong Kong, Kowloon, as a Research Assistant. He is currently a Lecturer with the Electronic Engineering of NJUST. He is the author or coauthor of over 20 technical papers. His current research interests include computational electromagnetics, electromagnetic scattering and radiation.

# Cosecant Squared Pattern Synthesis for Reflector Antenna using a Stochastic Method

**A. R. Mallahzadeh and P. Taghikhani**

Department of Electrical Engineering
Shahed University, Tehran, Iran
Mallahzadeh@shahed.ac.ir, taghikhani@shahed.ac.ir

***Abstract*** ─ A novel method based on invasive weed optimization (IWO) algorithm is described for synthesizing a point source doubly curved reflector antenna to produce a shaped beam in one plane and narrow beam in the perpendicular plane. The whole reflector body can be created by determining two basic curves. The central vertical curve is approximately responsible for producing a shaped beam in the vertical plane. It can be expressed by a well-defined function, and the function coefficients will compose a solution space to be explored by IWO. The transverse section curve is known to be a parabola for producing a narrow beam in that plane. The validity of the proposed method is verified by an example of shaped reflector antenna with cosecant squared pattern and comparing it with previously used methods. The simulation results based on physical optics (PO) further prove the validity and versatility of this technique for solving reflector synthesize problems.

***Index Terms*** ─ Cosecant squared pattern, doubly curved reflector, IWO.

## I. INTRODUCTION

Antennas with the cosecant squared pattern in the elevation plane and pencil beam in the azimuth plane are widely used in surveillance-search radar systems. In comparison with phased array antennas, reflector antennas don't have the calibration and implementation problems. Doubly curved reflector antenna is a classical antenna for this purpose. The synthesis procedure based on geometrical optics (GO) is described in details by many authors [1-4]. Different types of configuration [4-6] and analysis methods for computing its farfield pattern has been presented in [7-11]. The design procedure based on GO, is inflexible to achieve extra desired features such as low sidelobe level or low ripples at the shaped beam region for antenna performance. By knowing that doubly curvature antenna can be synthesized to produce a shaped beam in one of the principle planes, and after the success of optimization algorithms in antenna problems, the authors are guided to create a new synthesis method for doubly curved reflector antennas.

Optimization algorithms in solving antenna problems are always employed for improving antenna performance for example, [12, 13]. In this paper, the authors try to employ an optimization algorithm to create a synthesis method for doubly curved reflector antennas. The algorithms could find the antenna structure independently and by defining a proper goal both synthesize and optimization can be done. Describing central section curvature of reflector surface using a few parameters, and finding the parameters to reach the antenna desired performance, is fundamental to the proposed method. This method uses IWO as a tool to perform the idea, because IWO is an efficient and robust optimization algorithm method in finding global minima. It was first extracted by [14] and successfully has been used in antenna design problems [15-18]. In this paper, the basic concept of GO synthesis is reviewed briefly. Then, the proposed method is described in details so that the procedure can be fully understood and in the next step, a reflector is designed and compared with the reflector designed based on the previous GO based method.

*Submitted On: January 6, 2011*
*Accepted On: August 24, 2011*

## II. THEORETICAL ANTENNA DESIGN

Totally for reflector antenna problems and propagation problems [19], geometrical optics analysis can be more useful and efficient than other methods. For doubly curved reflector antennas, the conventional way to synthesize a shaped pattern is based on GO also [1-3]. In this section, we will only review the basic concept of GO synthesis procedure and extract design formulas.

Doubly curved reflector antenna contains two main sections. The central vertical section of the reflector must be designed to provide the desired elevation shaped pattern. The transverse section is required to be a parabola for focusing feed rays in the transverse or azimuth plane to produce the narrow beam in that plane.

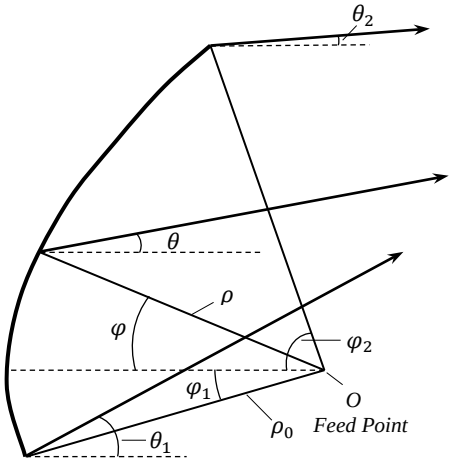


Fig. 1. Central vertical curve parameters.

### A. Central vertical section

In order to shape the reflector antenna's surface to have a prescribed elevation pattern, the proper central vertical section must be found. It means that the central vertical section has the dominant effect on elevation pattern. The central curve is illustrated in Fig. 1 [4]. Consider that the phase center of feed is located at the origin *O*. $\varphi$ is the angle of incident ray with respect to $z$ and $\theta$ is the angle of reflected ray. The angle between the incident and reflected rays, $\sigma$, can be determined as follows:

$$\sigma = \theta + \varphi, \tag{1}$$

$\rho$ is the distance from origin to central curve. Clearly $\theta$ and $\rho$ are functions of $\varphi$ (i.e. $\sigma(\varphi)$ and $\rho(\varphi)$). The differential equation of the central curve is [2]:

$$\frac{d\rho}{\rho d\varphi} = \tan(\frac{\sigma}{2}), \tag{2}$$

In this equation, $\sigma(\varphi)$ and $\rho(\varphi)$ are both unknown. If we know $\sigma(\varphi)$, $\rho(\varphi)$ can be determined.

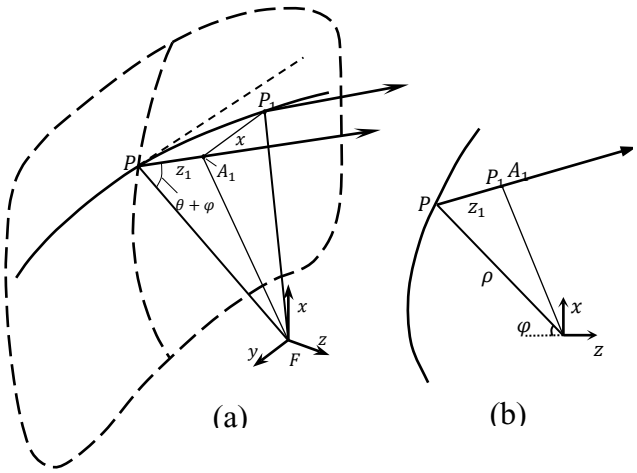


Fig. 2. Ray path in transverse section curve: (a) 3D view, (b) side view.

### B. Transverse section of reflector

The transverse sections of the surface are determined by the requirement that the reflector is to convert a spherical wave into a cylindrical wave. For this purpose, all reflected rays from the reflector in the direction $\theta$ need to be parallel. Therefore, as illustrated in Fig. 2 the following condition must be met [4]:

$$\overline{FP_1} = \overline{FP} + \overline{PA_1}, \tag{3}$$

this leads to

$$\left[\rho^2 + z_1^2 - 2\rho z_1 \cos(\varphi+\theta) + y^2\right]^{\frac{1}{2}} = \rho + z_1, \tag{4}$$

The latter equation gives transverse parabolas of the reflector surface. The desired surface can be achieved by combining both vertical and transverse curves of reflector.

To determine the reflector central curve using (2), it is necessary to derive a more useful differential equation based on energy balance principles of GO.

Let $I(\varphi,\psi)$ be the incident energy of feed. $I(\varphi,0)d\psi d\varphi$ is the power incident on a central element of the reflector. This power is reflected in a wedge with a $\rho d\psi$ width and with a wedge angle $d\theta$. If $P(\theta)$ is the reflected energy of

antenna, the following relation can be written based on the GO principle of energy balance [1-4]:

$$P(\theta)\rho d\psi d\theta = I(\varphi) d\psi d\varphi, \quad (5)$$

Taking logarithmic derivatives with respect to $\varphi$ of Eq. (5) and substituting from Eq. (2), we get instead the differential equation which for cosecant squared pattern with

$$P(\theta) = \csc^2(\theta), \theta_1 < \theta < \theta_2 \text{ when } \varphi_1 < \varphi < \varphi_2, \quad (6)$$

it is

$$\frac{d^2\theta}{d\varphi^2} + \left[ \tan(\frac{\varphi - \theta}{2}) - \frac{I'(\varphi)}{I(\varphi)} \right] \frac{d\theta}{d\varphi} - \left(2\cot\theta\right)(\frac{d\theta}{d\varphi})^2 = 0. \quad (7)$$

This equation couldn't be solved analytically and has to be discretized and solved numerically. Besides, a proper guess for the initial value of $d\theta/d\varphi$ is required to solve this equation [1]. Finding the proper initial value for $d\theta/d\varphi$ needs an exhausting trial-and-error and different values must be examined to achieve the desired farfield pattern.

After finding $\theta(\varphi)$, $\sigma(\varphi)$ and $\rho(\varphi)$ will be clear. By using Eq. (2) and Eq. (4), whole reflector body is achieved.

## III. SHAPED REFLECTOR SYNTHESIS USING IWO

Recently, employing optimization algorithms, such as genetic algorithm, particle swarm optimization, ant colony, and etc., for solving an antenna optimization problem is very common. Another algorithm is the invasive weed optimization (IWO) which was first proposed by Mehrabian and Lucas [14]. IWO is an effective and robust algorithm to find global minima as it has been shown in [14]. According to [14, 18], the algorithm process can be summarized as follows:

1. A finite number of seeds spread out randomly on the search area.
2. They grow to flowering weeds and produce seeds. The number of reproduced seeds of each weed depends on its own fitness and better fitness permits more seeds to be reproduced. However, the maximum number of seeds is limited.
3. These reproduced seeds disperse over the search area around their parent weeds. The random dispersion has a normal distribution with mean equal to zero but varying variance (spatial dispersal). The standard deviation (SD) decreases in each time step of the algorithm as [14]

$$SD_{iter} = \frac{(iter_{\max} - iter)^n}{(iter_{\max})^n}(SD_{initial} - SD_{final}) + SD_{final}, \quad (8)$$

where $iter$ is the number of current time step, $iter_{max}$ is the maximum number of iterations, $SD_{iter}$ is the SD at the present time step, $SD_{initial}$ and $SD_{final}$ are prescribed constant values for SD at first and last iteration, and $n$ is the nonlinear modulation index which usually is set to 3. This decreasing behavior for SD causes aggregation of seeds around better solutions.

4. There is a maximum for the number of weeds in each time step and only plants with better fitness can survive and produce seeds in the next step (competitive exclusion). The process continues until the maximum number of iterations is reached and finally the plant with the best fitness is closest to the optimal solution. The flow chart of this algorithm is represented Fig. 3. [18].

### A. Antenna synthesis using IWO

In this paper, we employ the ability of IWO for synthesizing a doubly curved reflector antenna. IWO will choose the best design depending on its defined goal. The synthesis method can define the desired pattern and reach to it while in synthesis procedure by the GO method, there is not enough flexibility in defining the desired sidelobe level or limited ripple in the shaped region. The optimization algorithm tries to find the best reflector body which its characteristics are fitted on the desired characteristics.

It was mentioned in Section 3 that the basic curves of the doubly curved reflector antenna can construct the whole body of it. It can be said that the central vertical curve approximately produces the shaped elevation pattern and transverse section is mostly a parabola to emerge feed rays parallel for generating a pencil beam in the transverse or azimuth plane.

In the synthesis procedure based on IWO, the main idea is finding a central section curve which can create a reflector body with the desired shaped pattern. Transverse sections are parabolas and don't need to be found. In order to implement the idea, we recommend the following method.

**B. Central curve synthesis using IWO**

In order to determine the central curve by the optimization algorithm, at first, the curve must be expressed by a finite number of parameters. For example, the curve's function can be approximated to an *n*-th order polynomial with *n+1* coefficient or parameters. Afterward, these parameters need to be determined properly by IWO for creating the central curve. The central curve with the parabolas which are mentioned in Eq. (4) will create the whole body of reflector. The optimization procedure has a goal which is obtaining the desired $(\csc\theta)^2$ pattern in the elevation plane.

In this paper, central curve is expressed indirectly. As it was described in Section 3, if the distribution of $\sigma(\varphi)$ between $\varphi_1$ and $\varphi_2$ is determined, $\theta(\varphi)$ and $\rho(\varphi)$ will be determined, respectively according to equations (1) and (2), and then the central vertical curve will be created. For approximating $\sigma(\varphi)$ distribution, various functions were examined to find a function with fewer parameters and good accuracy. The best choice was the 4-th order polynomial:

$$\sigma(\varphi) = p_1\varphi^4 + p_2\varphi^3 + p_3\varphi^2 + p_4\varphi + p_5, \qquad (9)$$

where $p_i$ , $i = 1,2,\ldots,5$ are the parameters which should be determined. The IWO process starts with initial random coefficients of a chosen function for $\sigma(\varphi)$. Random central curves and then random surfaces will be generated according to Eq. (4). So in each time step of the algorithm, we have a number of random reflector surfaces. To obtain the elevation radiation pattern of each reflector it has to be analyzed. Since we have the radiation pattern of the feed, the secondary pattern of reflector can be obtained by PO simulations. The obtained elevation pattern is compared with the ideal sector cosecant squared pattern. Consequently, the error (or fitness) value of weed (produced surface) is the difference between far field vertical plane pattern and a desired sector cosecant squared pattern. The optimization process continues until accomplishing a radiation pattern which is closest to cosecant squared pattern.

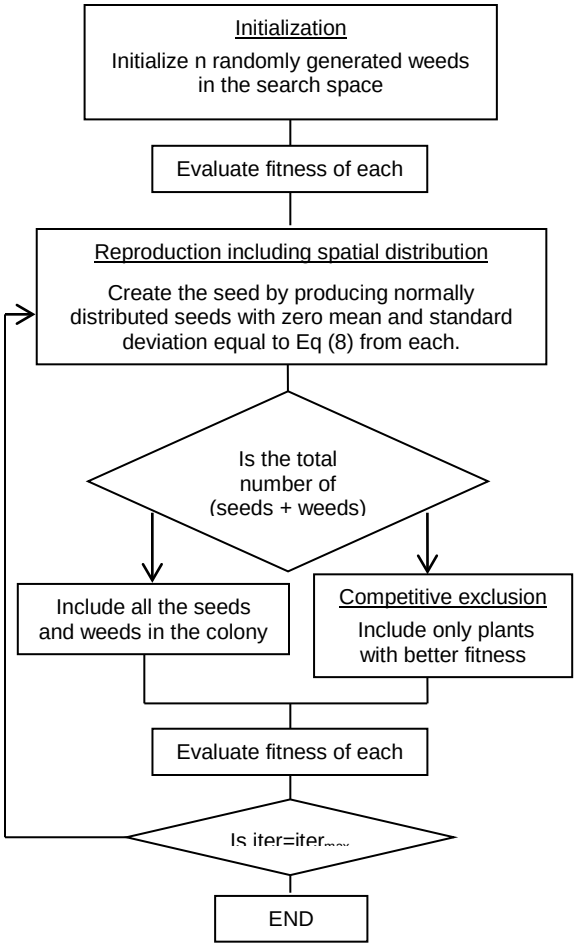


Fig. 3. A flow-chart representation of the IWO algorithm.

In this paper, the focus is on achieving a low ripple in the shaped region. To do this a proper fitness function is needed to be calculated for every produced reflector, which focuses on shaped region error. Consider that the obtained elevation pattern of each reflector varies from $-180^\circ$ to $180^\circ$. We sample $N$ point of this elevation pattern (the value of gain $G_i$) and calculate the fitness function as follows:

$$f = \frac{1}{N}\left(\sum_{\theta_1^\circ}^{\theta_2^\circ}\left(\left|G_i(\theta) - (\csc\theta)^2\right|\right)^2 + \sum_{o.w.}\left(\frac{1}{2}(X + |X|)\right)^2\right), \qquad (10)$$

where

$$X = \left[G_i(\theta) - (-25)\right]; \quad \& \quad o.w. \equiv \begin{cases} -180^\circ \le \theta \le \theta_0 \\ \theta_2 \le \theta \le 180^\circ \end{cases}$$

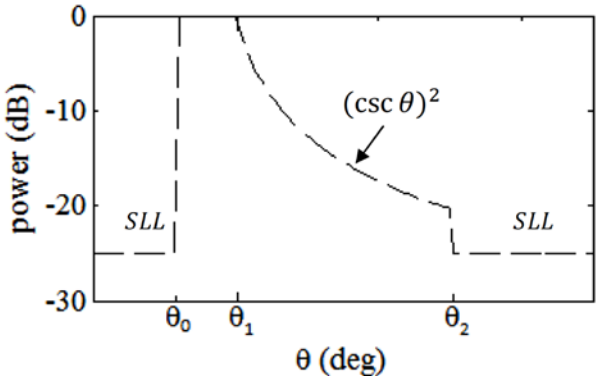


Fig. 4. Specifying $\theta_0$, $\theta_1$, and $\theta_2$ in goal boundaries.

As it is mentioned in the fitness function if the side lobe level goes upper than -25 dB, another term, which is the relative error of the unwanted and desired sidelobe level, will be added to the error due to the cosecant region. The region between $\theta_0$ and $\theta_1$ does not affect the total error.

## IV. SIMULATION RESULTS

Table 1: IWO parameter values

| Symbol | Quantity | Value |
|---|---|---|
| N | Number of initial population | 25 |
| $iter_{max}$ | Maximum number of iterations | 50 |
| Dim | Problem dimension | 5 |
| Pmax | Maximum number of plant population | 8 |
| Smax | Maximum number of seeds | 5 |
| Smin | Minimum number of seeds | 1 |
| N | Nonlinear modulation index | 3 |
| SDintial | Initial value of standard deviation | 10 |
| SDfinal | Final value of standard deviation | 0.01 |
| Lini | Initial search area | -5 to +5 |

In order to show the ability of the IWO algorithm in synthesizing this type of antenna, a detailed simulation result is presented. The $\rho_0$ is chosen to be $0.724\ m$. Therefore, the antenna dimension is $1.3\ m \times 0.88\ m$. The feed is a typical horn operating at 9.37 GHZ frequency. Since the feed is placed 15° offset and has about 92° 10–dB beam width, $\varphi$ varies from -61° to 31°. $\sigma(\varphi)$ is specified according to Eq. (9).

The 10–dB beam width of feed in the transverse plane and the positioning of the central section curve in front of feed, specifies the size of the reflector in that plane.

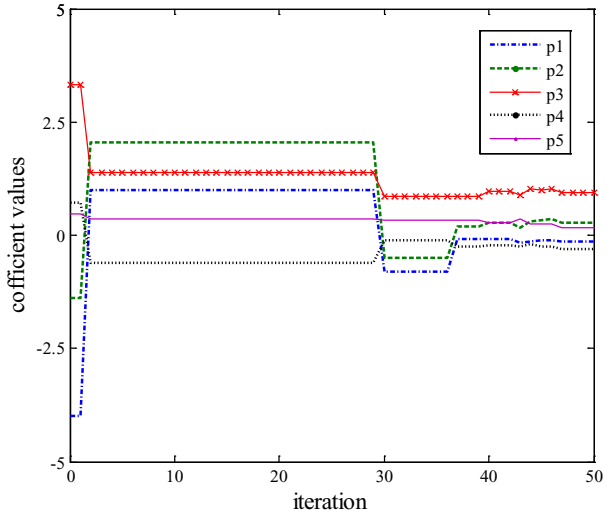


Fig. 5. $\sigma(\varphi)$'s coefficient values as the number of iteration increases.

The optimization procedure is started with the parameters' values which are tabulated in Table 1. The other related graphs for IWO are Fig. 5 and Fig. 6. Figure 5 shows the convergence process of coefficients (which are the algorithm dimensions) versus iteration. After 50 iterations, the optimum solution or lowest fitness is achieved (Fig. 6). The final values of $p_i$ , $i = 1,2,\ldots,5$ are in Table 2.

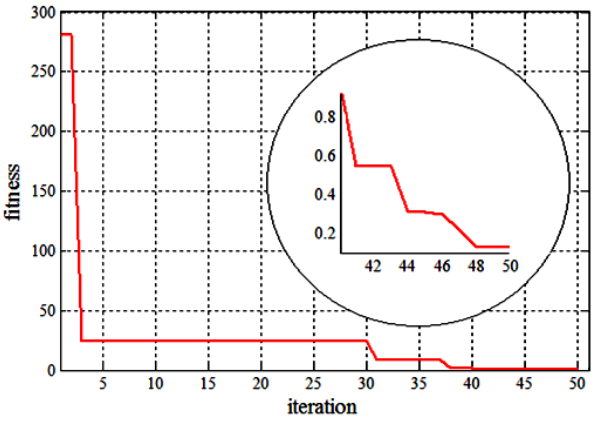


Fig. 6. Convergence diagram of optimization procedure.

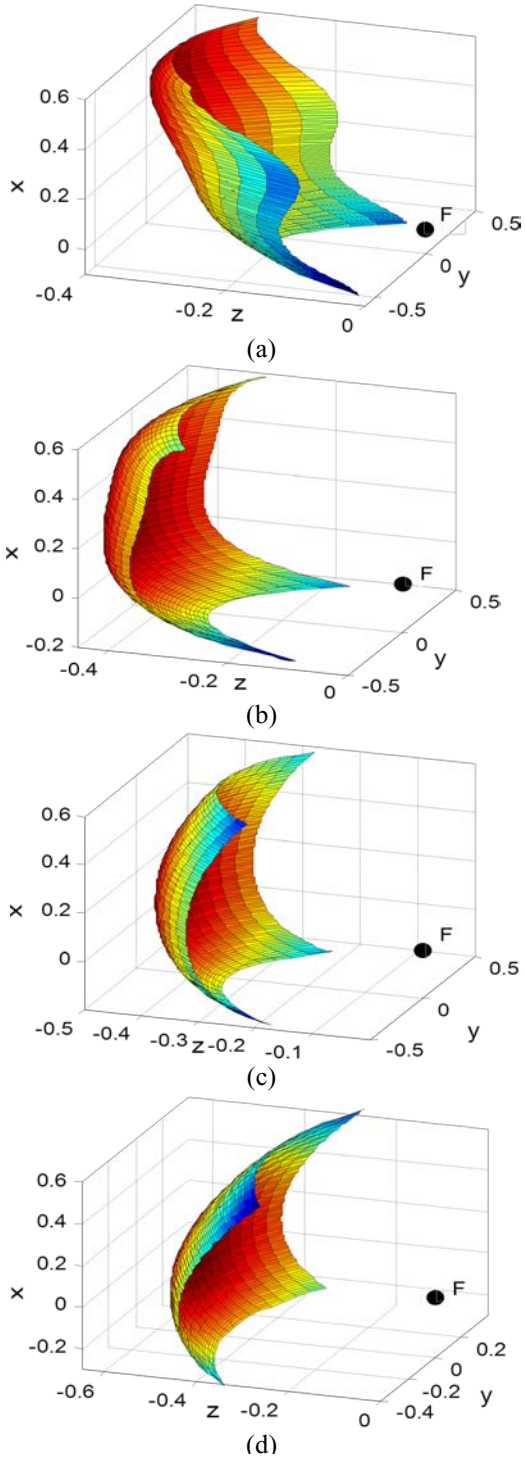


Fig. 7. Convergence procedure of reflector surfaces (3D view). (a) Initial produced reflector, (b) produced reflector surface in second iteration, (c) produced reflector surface in 25-th iteration, and (d) the final optimum reflector surface.

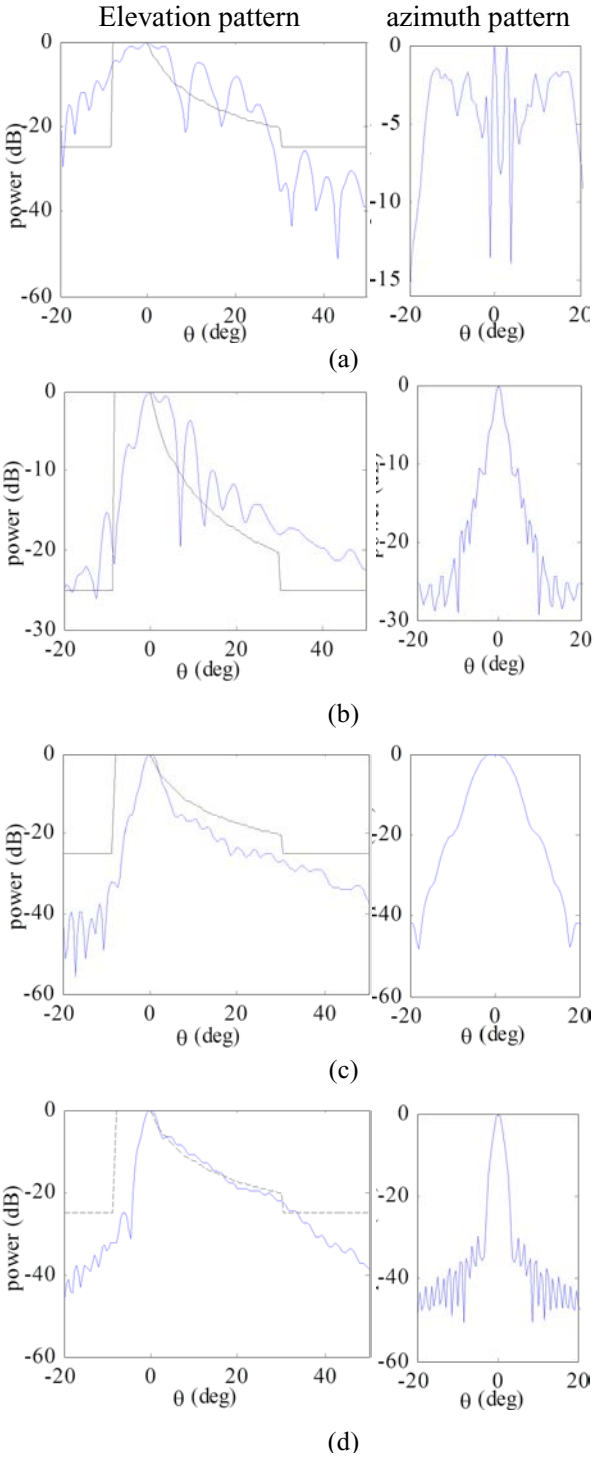


Fig. 8. Radiation pattern of produced reflector surfaces in Fig. 7. (a) Initial produced reflector, (b) produced reflector surface in second iteration, (c) produced reflector surface in 25-th iteration, and (d) the final optimum reflector surface.

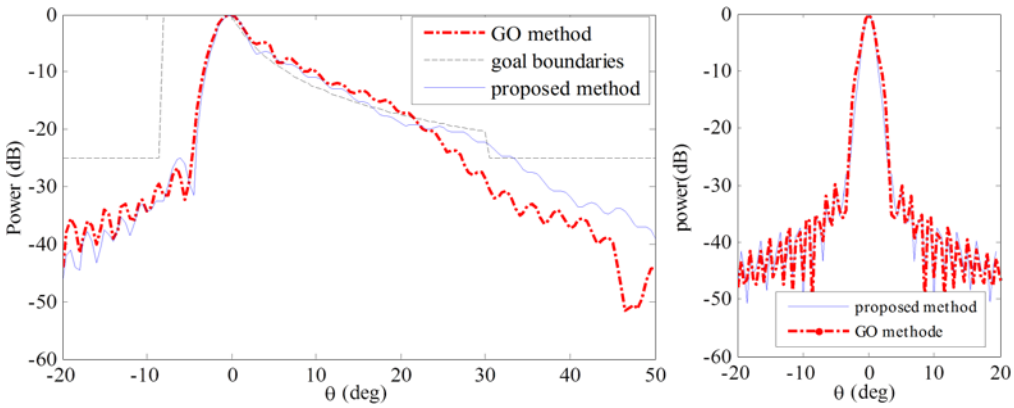


(a) (b)

Fig . 9. Comparison between two methods: (a) on the ripple of the shaped region in elevation pattern, (b) pencil beam in azimuth pattern.

Table 2: $\sigma(\varphi)$'s coefficient final optimum values

| $p_1$ | $p_2$ | $p_3$ | $p_4$ | $p_5$ |
|---|---|---|---|---|
| -0.1494 | 0.2818 | 0.9416 | -0.3041 | 0.16 |

In Fig. 7, the surfaces, which are produced during IWO iterations, are shown. It can be seen that the surfaces try to find their proper configuration as the number of iteration increases. The far filed patterns of the illustrated surfaces are shown in Fig. 8 respectively. As it is shown, the elevation pattern tries to be fitted to its defined goal as the number of iteration increases. The disorganized azimuth patterns in Fig. 8 are resulted of disorganized surfaces in their corresponding steps of iteration. In order to comprise the simulated pattern of the proposed method and the GO based method, another reflector in the equal conditions, same as feed position and reflector dimension is designed based on the GO method. It is shown in Fig. 9. Actually, the ripple in the cosecant squared band for the designed antenna using IWO, is less than 2dB, But the other pattern has the larger ripple.

## V. CONCLUSION

The invasive optimization algorithm (IWO), a novel stochastic algorithm has been successfully employed to create a flexible method to design doubly curved reflector antennas. Totally, synthesis procedures based on optimization algorithms can reduce the complexity of the problem and improve the flexibility in design goals and antenna performance. In addition, other antenna parameters such as positions, orientations, and feed excitation can be set as other optimization parameters. Furthermore, different types of desired goals can be defined to be optimized. In this paper, the focus was on a lower ripple on the cosecant squared region while other characteristics like the extremely low sidelobe level or elimination ground effect by having a sharp fall in the elevation pattern before shaped region and other definable goals can be defined and achieved. The proposed method is suggested to be employed because of more flexibility in defining a desirable destination pattern. The validity of the proposed technique is verified by designing the fixed antenna set using the two described methods. If a more accurate simulation is employed, the method can be more accurate.

## REFERENCES

[1] S. Silver, *Microwave Antenna Theory and Design*, McGraw-Hill, New York, 1949.

[2] A. S. Dunbar, "Calculation of Doubly Curved Reflectors for Shaped Beams," *Proc. IRE*, vol. 36, pp.1289-1290, October 1948.

[3] T. A. Milligan, *Modern Antenna Design*, John Wiley, 2nd ed., 2005.

[4] A. Brunner, "Possibilities of Dimensioning Doubly Curved Reflectors for Azimuth-Search radar Antennas," *IEEE Trans. Antennas and Propagat.*, vol. AP-19, no. 1, pp. 52-57, January 1971.

[5] M. Mizusawa, S. I. Betsudan, S. Urasaki, and M. Iimori, "A Dual Doubly Curved Reflector Antenna Having Good Circular Polarization Characteristics," *IEEE Trans. Antennas and*

*Propagat.*, vol. AP-26, no. 3, pp. 455-458, May 1978.

[6] S. Karimkashi, A. R. Mallahzadeh, and J. Rashed-Mohassel, "A New Shaped Reflector Antenna for Wide Beam Radiation Patterns," *IEEE International Symposium on Microwave, Antenna, Propagation, and EMC Technologies for Wireless Communications*, pp. 535-538, August 2007.

[7] T. F. Carberry, "Analysis Theory for the Shaped-Beam Doubly Curved Reflector Antenna," *IEEE Trans. Antennas and Propagat.*, vol. AP-17, no. 2, pp.131-138, March 1969.

[8] F. Winter, "Dual Vertical Beam Properties of Doubly Curved Reflectors," *IEEE Trans. Antennas and propagat.*, vol. AP-19, no. 2, pp. 174-180, March 1971.

[9] J. Sletten, "Ray Tracing Method for Doubly Curved Reflector Surfaces," *Proceeding of The IEEE*, vol. 69, no. 6, pp. 743-744, June 1981.

[10] J. Pidanic, D. Cermak, and V. Schejbal, "Gain Estimation of Doubly Curved Reflector Antenna," *Radioengineering*, vol. 17, no. 3, pp. 38-41, September 2008.

[11] S. Junhao, "On the Improvement of Shaped-Beam Doubly Curved Reflector Antenna," *Antennas, Propagation & EM Theory, ISAPE '06. 7th International Symposium on*, pp. 26-29, October 2006.

[12] S. Alfonzetti, G. Borzì, E. Dilettoso, and N. Salerno, "Stochastic Optimization of a Patch Antenna," *Applied Computational Electromagnetic Society (ACES) Journal*, vol. 23, no. 3, pp. 237-242, September 2008.

[13] J. Martinez-Fernandez, J. M. Gil, and J. Zapata, "Ultrawideband Optimized Profile Monopole Antenna by Means of Simulated Annealing Algorithm and the Finite Element Method," *IEEE Trans. Antennas Propagtion.*, vol. 55, no. 6, pp. 1826-1832, June 2007.

[14] A. R. Mehrabian and C. Lucas, "A Novel Numerical Optimization Algorithm Inspired from Weed Colonization," *Ecoogical Informatics*, vol. 1, pp. 355–366, 2006.

[15] A. R. Mallahzadeh, H. Oraizi, and Z. Davoodi-Rad, "Application of the Invasive Weed Optimization Technique for Antenna Configurations," *Progress of Electromagnetics Research PIER 52*, pp.225–254, 2008.

[16] A. R. Mallahzadeh, S. Es'haghi, and H. R. Hassani, "Compact U-Array MIMO Antenna Designs Using IWO Algorithm," *International Journal of RF and Microwave Computer-Aided Engineering.*, vol. 19, Issue 5, pp. 568–576, September 2009.

[17] B. Bahreini, A. R. Mallahzadeh, and M. Soleimani, "Design of a Meander-Shaped MIMO Antenna Using IWO Algorithm for Wireless Applications," *Applied Computational Electromagnetic Society (ACES) Journal*, vol. 25, no. 7, pp. 631-638, July 2010.

[18] S. Pal, A. Basak, S. Das, and A. Abraham, "Linear Antenna Array Synthesis with Invasive Weed Optimization Algorithm," *Soft Computing and Pattern Recognition (SoCPaR) International Conference of*, pp. 161 - 166, December 2009.

[19] C. W. Trueman, "Three-Dimensional Geometrical Optics Code for Indoor Propagation," *Applied Computational Electromagnetic Society (ACES) Journal*, vol. 17, no. 2, pp.134-144, July 2002.

**Alireza Mallahzadeh** received the B.S. degree in Electrical Engineering from Isfahan University of Technology, Isfahan, Iran, in 1999 and the M.S. degree in Electrical Engineering from Iran University of Science and Technology, Tehran, in 2001, and the Ph.D. degree in electrical engineering from Iran University of Science and Technology, Tehran, in 2006. He is a member of academic staff, Faculty of Engineering, Shahed University, Tehran. He has participated in many projects relative to antenna design, which resulted in fabricating different types of antennas for various companies. Also, he is interested in numerical modeling, and microwaves.

**Parastoo Taghikhani** received the B.S. and M.S. degree in Electrical Engineering from Shahed University, Tehran, Iran, in 2008 and 2011. Her research interests are antennas, propagation and microwaves. She also is interested in optimization algorithms.

# An Efficient Parallel FE-BI Algorithm for Large-scale Scattering Problems

**Z. H. Fan, M. Chen, R. S. Chen, and D. Z. Ding**

Department of Communication Engineering
Nanjing University of Science and Technology, China
Nanjing, P.R. China, 210094
eechenrs@mail.njust.edu.cn

***Abstract*** ─In this paper, we present fast and accurate solutions of large-scale scattering problems involving three-dimensional objects with arbitrary shapes using parallel finite element-boundary integral method (FE-BI). Particularly, an efficient parallel preconditioner is constructed with both the finite-element matrix and the near-field part of the boundary integral equation operator for the ill-conditioned linear system formulated by the FE-BI. With an efficient parallelization of FE-BI, scattering problems that are discretized with millions of unknowns could be easily solved on distributed-memory computers. The numerical results are presented to demonstrate the accuracy and efficiency of the proposed method.

***Index Terms*** **-** Finite element boundary integral method, parallelization, multilevel fast multipole method, scattering problems.

## I. INTRODUCTION

The finite element boundary integral method (FE-BI) [1-5] provides fast and accurate solutions for three-dimensional electromagnetic scattering from complex geometries, which may be comprised of both conductors and dielectric media. The method divides the analyzed objects into two regions, one is the interior region and another is the exterior region. The field in the interior region is formulated using the finite-element method (FEM) and the field in the exterior region is represented by a boundary integral equation (BIE). The interior and exterior fields are then coupled by the field continuity conditions. In the FE-BI method, the final coefficient matrix is made up of a complex dense BIE sub-matrix and a complex sparse FEM sub-matrix. The multilevel fast multipole method (MLFMM) [6-10] is used to speed up the matrix-vector product (MVP) for the dense BIE part when the electrically large object is analyzed, which reduces the memory requirement from $O(N^2)$ to $O(NlogN)$ and the computational complexity from $O(N^3)$ to $O(NlogN)$, where $N$ is the number of unknowns belongs to BIE part. When the FE-BI is combined with MLFMM, the coefficient matrix can be fast built when a large object is analyzed. Unfortunately, the FE-BI method suffers from a very slow convergence rate with the iterative solvers since the coefficient matrix arising from FE-BI is badly ill-conditioned. This bottleneck severely limits the capability of the FE-BI method since the iterative methods are the only choose for the large-scale problems. To break this bottleneck, many preconditioners have been developed to accelerate the convergence rate, such as the diagonal, block-diagonal, but they are not effective enough to yield a highly efficient solution. In [11], Liu and Jin proposed to use the FEM-absorbing boundary condition (ABC) matrix as the precondition for the FE-BI matrix equation. However, about 0.05 $\lambda$ distance should be set between both the absorbing boundary and the scattering objects to improve the efficiency of the preconditioner. This will bring an increase of unknowns for the increscent calculation domain, which reduces the efficiency of the FE- ABC preconditioner. In this paper, an efficient preconditioner is constructed by the finite-element

*Submitted On: March 6, 2011*
*Accepted On: September 12, 2011*

part and the near-field value terms of the boundary integral, both can be easily obtained from the FE-BI matrix with no additional cost and memory requirement since the main contribution of the impedance matrix for the boundary integral is given by the near-field part. In our experience, the convergence rate of solving the FE-BI matrix is significantly accelerated after equipping this preconditioning technique.

Although the preconditioned FE-BI has been applied to a variety of electromagnetic problems with remarkable success, accurate solutions of many real-life problems require discretization with more than millions of unknowns, leading to large-scale matrix equations, which can not be solved on a single personal computer. In order to solve large problems, it is necessary to parallelize the FE-BI code and implement on distributed computers. However, it is not a trivial to design a high efficient parallelization scheme because of the complicated structure of the FE-BI matrices. Simple parallelization techniques usually fail to provide efficient solutions, due to communications among processors, poor loading-balance of the work. In this work, the FE-BI matrix is divided according to the features of the sub-matrices, which making it possible to compute and store only a small part of matrix in each computer and take full advantage of the parallelization computing. Especially, a series of implementation efforts previously developed for parallelizing the MLFMM in [12-19] are adopted to improve the parallelization efficiency of the BIE part, which is the most important point for the whole parallelization implementation. At the same time, the precondition matrix is constructed and factorized in parallelization.

The remainder of this paper is organized as follows. Section II gives a brief introduction to the FE-BI, together with an introduction of the novel preconditioner for the FE-BI. The parallization of FE-BI is also investigated in this part in detail. Section III presents the numerical results to demonstrate the accuracy and efficiency of the proposed method. Finally, some conclusions are given in section IV.

## II. THEORY

Consider the problem of electromagnetic wave scattering by an inhomogeneous object characterized by relative permittivity $\varepsilon_r$ and permeability $\mu_r$ . The object is excited by an incident field $\boldsymbol{E}^i(\boldsymbol{r})$ and the total field $\boldsymbol{E}(\boldsymbol{r})$ comprises the sum of the incident field $\boldsymbol{E}^i(\boldsymbol{r})$ and the scattered field $\boldsymbol{E}^s(\boldsymbol{r})$ . To solve this problem with FE-BI, we first introduce a surface $S$ to enclose the object and divide the object into an interior region and an exterior region. We employ the FEM to deal with the interior region. The exterior region is formulated using the BIE. The field inside $S$ can be formulated into an equivalent variational problem with the functional given by

$$F(\mathbf{E})=\frac{1}{2jk_0}\iiint_V\left[\frac{1}{\mu_r}(\nabla\times\mathbf{E}(\mathbf{r}))\bullet(\nabla\times\mathbf{E}(\mathbf{r}))-k_0^2\varepsilon_r\mathbf{E}(\mathbf{r})\bullet\mathbf{E}(\mathbf{r})\right]dV+\eta_0\oiint_S(\mathbf{E}(\mathbf{r})\bullet\mathbf{J}_s(\mathbf{r}))dS, \quad (1)$$

where $k_0$ and $\eta_0$ denote the free-space wave number and impedance, respectively. $V$ denotes the volume enclosed by $S$, $\hat{n}$ denotes the outward unit vector normal to $S$, $K_0$ is the free-space wave number. Using tetrahedron-based edge elements to expand $\mathbf{E}(\mathbf{r})$ and Rao-Wilton-Glisson (RWG) [20] basis functions to expand $\boldsymbol{J}_s$

$$\mathbf{E}=\sum_{i=1}^{M}E_i\mathbf{W}_i\ ,\quad \boldsymbol{J}_s=\sum_{i=1}^{N_s}J_i\mathbf{f}_i\ . \quad (2)$$

Substituting (2) into (1), we obtain the matrix equation

$$\begin{bmatrix}\boldsymbol{K}_{\mathrm{II}} & \boldsymbol{K}_{\mathrm{IS}} & 0\\ \boldsymbol{K}_{\mathrm{SI}} & \boldsymbol{K}_{\mathrm{SS}} & \boldsymbol{B}\end{bmatrix}\begin{Bmatrix}\boldsymbol{E}_{\mathrm{I}}\\ \boldsymbol{E}_{\mathrm{S}}\\ \boldsymbol{J}_{\mathrm{S}}\end{Bmatrix}=\begin{Bmatrix}0\\ 0\end{Bmatrix}, \quad (3)$$

where $\boldsymbol{E}_{\mathrm{I}}$ is a vector containing the discrete electric field inside $V$, $\boldsymbol{E}_{\mathrm{S}}$, and $\boldsymbol{J}_s$ are the vectors containing the discrete electric and magnetic field on $S$. $[\boldsymbol{K}_{\mathrm{II}}],[\boldsymbol{K}_{\mathrm{IS}}],[\boldsymbol{K}_{\mathrm{SI}}],[\boldsymbol{K}_{\mathrm{SS}}]$, and $[\boldsymbol{B}]$ denote the corresponding highly sparse FEM matrices, $[\boldsymbol{K}_{\mathrm{II}}]$ and $[\boldsymbol{K}_{\mathrm{SS}}]$ are symmetric matrices and $[\boldsymbol{K}_{\mathrm{IS}}]=[\boldsymbol{K}_{\mathrm{SI}}]^T$ ,where the superscript $T$ denotes the transpose.

Equation (3) cannot be solved unless a relation between $\boldsymbol{E}_{\mathrm{S}}$ and $\boldsymbol{J}_s$ is established. Such a relation is provided by BIE for the exterior region, whose discretization yields

$$[\boldsymbol{P}]\{\boldsymbol{E}_{\mathrm{S}}\}+[\boldsymbol{Q}]\{\boldsymbol{J}_{\mathrm{S}}\}=\{\boldsymbol{b}\}\ . \quad (4)$$

In (4), $\{\boldsymbol{b}\}$ is a vector related to the incident

field. [$\boldsymbol{P}$] and [$\boldsymbol{Q}$] are generated by BIE. Combining (3) and (4) together, we obtain the following matrix equation

$$\begin{bmatrix} \boldsymbol{K}_{\mathrm{II}} & \boldsymbol{K}_{\mathrm{IS}} & 0 \\ \boldsymbol{K}_{\mathrm{SI}} & \boldsymbol{K}_{\mathrm{SS}} & \boldsymbol{B} \\ 0 & \boldsymbol{P} & \boldsymbol{Q} \end{bmatrix} \begin{Bmatrix} \boldsymbol{E}_{\mathrm{I}} \\ \boldsymbol{E}_{\mathrm{S}} \\ \boldsymbol{J}_{\mathrm{S}} \end{Bmatrix} = \begin{Bmatrix} 0 \\ 0 \\ \boldsymbol{b} \end{Bmatrix}. \quad (5)$$

The generation of (3) using FEM is standard, the generation of (4) using the method of moment (MoM) [20-21] can take many different forms. The basic equations for generating (4) are the electric-field integral equation (EFIE) is given by

$$\mathbf{E}^{inc}(\mathbf{r}) = \frac{1}{2}\mathbf{E}(\mathbf{r}) + \mathbf{L}(\bar{\mathbf{J}}_s) - \mathbf{K}(\mathbf{M}_s) \ , \quad (6)$$

and the magnetic-field integral equation (MFIE) is given by

$$\bar{\mathbf{H}}^{inc}(\mathbf{r}) = \frac{1}{2}\bar{\mathbf{H}}(\mathbf{r}) + \boldsymbol{L}(\mathbf{M}_s) + \boldsymbol{K}(\bar{\mathbf{J}}_s) \ , \quad (7)$$

where $\boldsymbol{J}$ and $\boldsymbol{M}$ are related to the fields on $S$ by $\bar{\mathbf{J}}_s = \eta_0 \hat{n} \times \mathbf{H}$ and $\mathbf{M}_s = \mathbf{E} \times \hat{n}$ , respectively, and ($\mathbf{E}^{inc}, \bar{\mathbf{H}}^{inc}$) denote the incident fields. The operators $L$ and $K$ are defined as

$$\mathbf{L}(\mathbf{X}) = jk_0 \iint_S \mathbf{X}(\mathbf{r}') G_0(\mathbf{r}, \mathbf{r}') \mathrm{d}S' + \iint_S \frac{j}{k_0} \nabla' \cdot \mathbf{X}(\mathbf{r}') \nabla G_0(\mathbf{r}, \mHbf{r}') \mathrm{d}S' \ , \quad (8)$$

$$\mathbf{K}(\mathbf{X}) = \iint_S \mathbf{X}(\mathbf{r}') \times \nabla G_0(\mathbf{r}, \mathbf{r}') \mathrm{d}S' \ . \quad (9)$$

However, each of them suffers from the problem of interior resonance and fails to produce accurate solutions at and near the resonant frequencies. To eliminate this problem, one has to combine EFIE and MFIE to obtain a combined field integral equation (CFIE). In this paper, the TE-NH is chosen which produces the best conditioned matrix for (5), substitute (2) into (6), we obtain the TE formulation

$$P_{mn} = \iint_S \mathbf{f}_m \cdot \left( -\frac{1}{2}\mathbf{w}_n(r) - \iint_S \mathbf{f}_n \times \nabla' G_0(\mathbf{r}, \mathbf{r}') \mathrm{d}S' \right) dS = -\frac{1}{2} B_{mn} + \iint_S \mathbf{f}_m \cdot \iint_S \mathbf{f}_n \times \nabla G_0(\mathbf{r}, \mathbf{r}') \mathrm{d}S' dS \quad (10)$$

$$Q_{mn} = \iint_S \mathbf{f}_m \cdot \left( -jk_0 \iint_S \mathbf{f}_n G_0(\mathbf{r}, \mathbf{r}') \mathrm{d}S' - \iint_S \frac{j}{k_0} \nabla' \cdot \mathbf{f}_n(\mathbf{r}') \nabla G_0(\mathbf{r}, \mathbf{r}') \mathrm{d}S' \right) dS = -jk_0 \iint_S \mathbf{f}_m \cdot \iint_S \mathbf{f}_n G_0(\mathbf{r}, \mathbf{r}') \mathrm{d}S' dS - \frac{1}{jk_0} \iint_S \nabla \cdot \mathbf{f}_m \iint_S \nabla' \cdot \mathbf{f}_n(\mathbf{r}') G_0(\mathbf{r}, \mathbf{r}') \mathrm{d}S' dS \ . \quad (11)$$

And from (7), the NH formulation

$$Q_{mn} = \left\langle \mathbf{f}_m, \frac{1}{2}\mathbf{f}_n(r) \right\rangle + \left\langle \mathbf{f}_m, \hat{n} \times \iint_S \mathbf{f}_n \times \nabla G_0(\mathbf{r}, \mathbf{r}') \mathrm{d}S' \right\rangle , \quad (12)$$

$$P_{mn} = -\hat{n} \times \mathbf{f}_m, jk_0 \iint_S \mathbf{f}_n G_0(\mathbf{r}, \mathbf{r}') \mathrm{d}S' - \iint_S \frac{j}{k_0} \nabla' \cdot \mathbf{f}_n(\mathbf{r}') \nabla G_0(\mathbf{r}, \mathbf{r}') \mathrm{d}S' \ . \quad (13)$$

The computational complexity of (5) consists of two parts: the part associated with FEM is $O(N)$ and the part related to BIE is $O(N_s^{\,2})$, where $N_s$ denotes the number of unknowns on the truncation boundary. The dense matrices [$\boldsymbol{P}$] and [$\boldsymbol{Q}$] generated by the BIE are bottleneck of the FE-BI method, which severely limit the capacity of the FE-BI method in dealing with electrically large objects. Fortunately, this problem can be solved iteratively, where the required the MVP are performed efficiently by the MLFMM, which reduces the memory requirement and the computational complexity to $O(N_s \log N_s)$ for the BIE. Conventionally, to implement the MLFMM, an octree first needs to construct. The entire object is first enclosed in a large box, which is divided into eight smaller boxes. Each sub-box is then recursively subdivided into eight smaller cubes until the edge length of the finest cube is about half of a wavelength. The interaction between these boxes can be divided into two cases: two cubes are near each other sharing at least one edge point, the interaction between the two groups are computed by MoM. Otherwise, two cubes are well-separated from each other if the ratio of the cube-center-distance to the cube size is greater than or equal to 2. The interactions between boxes are calculated using the MLFMM.

The basic formulae to calculate the matrix entries for the far groups in MLFMM are given by

$$P_{ij} = (\frac{1}{2\lambda})^2 \int V_{im}^{P} T_{mm'}(\hat{k} \cdot \hat{r}_{mm'}) \cdot V_{jm'} d^2\hat{k} \ , \quad (14)$$

$$Q_{ij} = (\frac{1}{2\lambda})^2 \int V_{im}^{Q} T_{mm'}(\hat{k} \cdot \hat{r}_{mm'}) \cdot V_{jm'} d^2\hat{k} \ , \quad (15)$$

where

$$T_{mm'}(\hat{k} \cdot \hat{r}_{mm'}) = \sum_{l=0}^{L} (-j)^l (2l+1) h_l^{(2)}(k_0 r_{mm'}) \cdot P_l(\hat{r}_{mm'} \cdot \hat{k}) \ , \quad (16)$$

$$V_{im}^{P} = \int_S e^{-j\mathbf{k}_0 \cdot \mathbf{r}_{im}} [-\hat{k} \times \mathbf{f}_i + (\bar{\mathbf{I}} - \hat{k}\hat{k}) \cdot (\hat{n} \times \mathbf{f}_i)] dS \ , \quad (17)$$

$$V_{im}^{Q} = \int_S e^{-j\mathbf{k}_0 \cdot \mathbf{r}_{im}} \left[ -\left(\bar{\mathbf{I}} - \hat{k}\hat{k}\right)\mathbf{f}_i - (\hat{k} \times \hat{n} \times \mathbf{f}_i) \right] dS \ , \quad (18)$$

$$V_{jm'} = \int_S e^{j\mathbf{k}_0 \cdot \mathbf{r}_{jm'}} \mathbf{f}_j dS \ . \quad (19)$$

Although the MLFMM for the BIE part has reduced the complexity of MoM from $O(N^2)$ to $O(N\log N)$, allowing the solution of large problems

with limited computational resources compared with the MoM. However, for problems with millions of unknowns, it is still not easy to solve it with FE-BI on a single processor. Thus, it is helpful to increase computational resource by assembling parallel computing platforms and, at the same time, by paralleling FE-BI.

### A. Novel preconditioner in FE-BI

For equation (5), there are two approaches to solve it. One is the direct solver [22]; the other is the iterative solver. For large-scale problems, it is impractical to solve the matrix equation with a large number of unknowns using the direct solver. This difficulty can be circumvented by solving the matrix equation using the Krylov subspace iterative method, which requires the MVP in each iteration step. In the past, several iterative methods, including the conjugate gradient (CG), the biconjugate gradient (BCG), the stabilized biconjugate gradient (BCGS), and the generalized minimal residual (GMRES) have been employed. Unfortunately, since the BIE produces a dense matrix, the final FE-BI system matrix consists of a partly-full matrix and a partly-sparse matrix. The FE-BI matrix is usually ill-conditioned and requires a large number of iterations to reach convergence. Therefore for electrically large objects, iterative solvers should be adopted with efficient preconditioners. There are many preconditioners that have been developed to speed up the convergence rate of the GMRES solution, e.g. the block-diagonal can help to partially alleviate this difficulty, but they are not effective enough to yield a highly efficient solution. In [11], a FE-ABC preconditioner has been proposed and proven to be highly efficient for the FE-BI. However, a certain distance should be set between the absorbing boundary and the scattering objects to improve the efficiency of the preconditioner. This will bring the increase of the unknowns for the FE-BI. In this paper, an efficient preconditioner is constructed by the finite-element part and the near-field part of the boundary integral, both can be easily obtained from the matrix of the FE-BI with no additional computing cost and memory requirement since the main contribution of the impedance matrix for the boundary integral is given by the near-field part. Therefore, the preconditioning matrix is constructed by both the FEM matrix and the near-field part in the sparse pattern of the FEM matrix. Numerical results are presented to show the high effectiveness of the proposed method.

In this section, we consider solving the FE-BI matrix equation (5) with the MLFMM accelerated by the Krylov iterative method. In order to speed up the convergence rate of the Krylov iterative method, the preconditioning matrix $\boldsymbol{M}^{-1}$ is used to transform (5) into an equivalent form

$$\boldsymbol{M}^{-1}\boldsymbol{A}\boldsymbol{x} = \boldsymbol{M}^{-1}\boldsymbol{b}\,, \tag{20}$$

where

$$\boldsymbol{A} = \begin{bmatrix} \boldsymbol{K}_{\mathrm{II}} & \boldsymbol{K}_{\mathrm{IS}} & 0 \\ \boldsymbol{K}_{\mathrm{SI}} & \boldsymbol{K}_{\mathrm{SS}} & \boldsymbol{B} \\ 0 & \boldsymbol{P} & \boldsymbol{Q} \end{bmatrix} \quad \boldsymbol{x} = \begin{bmatrix} \boldsymbol{E}_{\mathrm{I}} \\ \boldsymbol{E}_{\mathrm{S}} \\ \boldsymbol{J}_{\mathrm{S}} \end{bmatrix} \quad \boldsymbol{b} = \begin{bmatrix} 0 \\ 0 \\ \boldsymbol{b} \end{bmatrix}.$$

With $\tilde{\boldsymbol{A}} = \boldsymbol{M}^{-1}\boldsymbol{A}$ and $\tilde{\boldsymbol{b}} = \boldsymbol{M}^{-1}\boldsymbol{b}$, equation (20) can be written as the following form

$$\tilde{\boldsymbol{A}}\boldsymbol{x} = \tilde{\boldsymbol{b}}\,. \tag{21}$$

$\boldsymbol{M}^{-1}$ is a matrix for preconditioning the matrix $\boldsymbol{A}$ from the left. The purpose of preconditioning is to make the condition number of the matrix $\tilde{\boldsymbol{A}}$ better than the original matrix $\boldsymbol{A}$. Thus, the Krylov iterative method for the equation (21) can get a fast convergence.

An effective preconditioner $\boldsymbol{M}$ [22-23] should be a good approximation of matrix $\boldsymbol{A}$ and easy to construct. Since the main contribution of the impedance matrix for the boundary integral is given by the near-field part. The preconditioner is constructed by the finite-element part and the near-field of the BIE matrix in sparse pattern as shown in (22); both can be easily obtained from the FE-BI matrix with no additional computing cost and memory requirement.

$$\boldsymbol{M} = \begin{bmatrix} \boldsymbol{K}_{\mathrm{II}} & \boldsymbol{K}_{\mathrm{IS}} & 0 \\ \boldsymbol{K}_{\mathrm{SI}} & \boldsymbol{K}_{\mathrm{SS}} & \boldsymbol{B} \\ 0 & \boldsymbol{P}' & \boldsymbol{Q}' \end{bmatrix}. \tag{22}$$

Then (20) can be written as follows

$$\begin{bmatrix} \boldsymbol{K}_{\mathrm{II}} & \boldsymbol{K}_{\mathrm{IS}} & 0 \\ \boldsymbol{K}_{\mathrm{SI}} & \boldsymbol{K}_{\mathrm{SS}} & \boldsymbol{B} \\ 0 & \boldsymbol{P}' & \boldsymbol{Q}' \end{bmatrix}^{-1} \begin{bmatrix} \boldsymbol{K}_{\mathrm{II}} & \boldsymbol{K}_{\mathrm{IS}} & 0 \\ \boldsymbol{K}_{\mathrm{SI}} & \boldsymbol{K}_{\mathrm{SS}} & \boldsymbol{B} \\ 0 & \boldsymbol{P} & \boldsymbol{Q} \end{bmatrix} \begin{Bmatrix} \boldsymbol{E}_I \\ \boldsymbol{E}_S \\ \boldsymbol{J}_S \end{Bmatrix} = \begin{bmatrix} \boldsymbol{K}_{\mathrm{II}} & \boldsymbol{K}_{\mathrm{IS}} & 0 \\ \boldsymbol{K}_{\mathrm{SI}} & \boldsymbol{K}_{\mathrm{SS}} & \boldsymbol{B} \\ 0 & \boldsymbol{P}' & \boldsymbol{Q}' \end{bmatrix}^{-1} \begin{Bmatrix} 0 \\ 0 \\ \boldsymbol{b} \end{Bmatrix}. \tag{23}$$

In order to reduce the computational complexity of the MVP, the second matrix in the left terms of (23) can be replaced according to the following

equation

$$\begin{bmatrix} \boldsymbol{K}_{\mathrm{II}} & \boldsymbol{K}_{\mathrm{IS}} & 0 \\ \boldsymbol{K}_{\mathrm{SI}} & \boldsymbol{K}_{\mathrm{SS}} & \boldsymbol{B} \\ 0 & \boldsymbol{P} & \boldsymbol{Q} \end{bmatrix} = \begin{bmatrix} \boldsymbol{K}_{\mathrm{II}} & \boldsymbol{K}_{\mathrm{IS}} & 0 \\ \boldsymbol{K}_{\mathrm{SI}} & \boldsymbol{K}_{\mathrm{SS}} & \boldsymbol{B} \\ 0 & \boldsymbol{P}' & \boldsymbol{Q}' \end{bmatrix} - \begin{bmatrix} 0 & 0 & 0 \\ 0 & 0 & 0 \\ 0 & \boldsymbol{P}-\boldsymbol{P}' & \boldsymbol{Q}-\boldsymbol{Q}' \end{bmatrix}, \quad (24)$$

and (24) can be sequentially transformed to the following form

$$\left\{ \boldsymbol{I} + \begin{bmatrix} \boldsymbol{K}_{\mathrm{II}} & \boldsymbol{K}_{\mathrm{IS}} & 0 \\ \boldsymbol{K}_{\mathrm{SI}} & \boldsymbol{K}_{\mathrm{SS}} & \boldsymbol{B} \\ 0 & \boldsymbol{P}' & \boldsymbol{Q}' \end{bmatrix}^{-1} \begin{bmatrix} 0 & 0 & 0 \\ 0 & 0 & 0 \\ 0 & \boldsymbol{P}-\boldsymbol{P}' & \boldsymbol{Q}-\boldsymbol{Q}' \end{bmatrix} \right\} = \begin{bmatrix} \boldsymbol{K}_{\mathrm{II}} & \boldsymbol{K}_{\mathrm{IS}} & 0 \\ \boldsymbol{K}_{\mathrm{SI}} & \boldsymbol{K}_{\mathrm{SS}} & B \\ 0 & \boldsymbol{P}' & \boldsymbol{Q}' \end{bmatrix}^{-1} \begin{Bmatrix} 0 \\ 0 \\ \boldsymbol{b} \end{Bmatrix}, \quad (25)$$

where $\boldsymbol{P}'$ and $\boldsymbol{Q}'$ stand for the near-field part drawing from the total matrix of boundary integral $\boldsymbol{P}$ and $\boldsymbol{Q}$ in the sparse pattern of FEM matrices $\boldsymbol{B}$ and $\boldsymbol{K}_{SS}$, respectively.

For sequential implementations of the FE-BI running on a single processor, the calculation of $\boldsymbol{M}^{-1}$ can be obtained by the UMFPACK strategy [24]. However, for large-scale problems, the direct solver $\boldsymbol{M}^{-1}$ may require prohibitive memory and the time used to construct the matrix $\boldsymbol{M}^{-1}$ will be very long. Fortunately this cost can be alleviated by parallelization. In this paper, we use the parallel LU factorization to construct the preconditioner matrix $\boldsymbol{M}^{-1}$, after decomposing the matrix $\boldsymbol{M}$ in the form of $\boldsymbol{M} = \boldsymbol{L}\bullet\boldsymbol{U}$. The preconditioning operation is performed in each step by solving $\boldsymbol{L}\bullet\boldsymbol{U}\bullet\boldsymbol{v} = \boldsymbol{w}$, the preconditioning operation $\boldsymbol{v} = \boldsymbol{M}^{-1}\boldsymbol{w}$ is computed by solving the linear system $\boldsymbol{L}\bullet\boldsymbol{U}\bullet\boldsymbol{v} = \boldsymbol{w}$, it is performed at two distinct steps: solve $\boldsymbol{L}\boldsymbol{x} = \boldsymbol{w}$ and $\boldsymbol{U}\boldsymbol{v} = \boldsymbol{x}$ successively. This two-step is processing in parallization. We call this preconditioning iteration as a forward and backward preconditioning iteration.

## B. Efficient parallelization of FE-BI matrix

Because of the complicated structure of the FE-BI matrix, parallelization of FE-BI is not trivial. Simple parallelization schemes usually lead to inefficient solutions due to dense communications and unbalanced distribution of the workload among processors. For high efficiency parallelization, two parts must be considered in detail. The first part is to partition the MoM matrices among the distribute computers. The second part is to construct the preconditioner matrices among the distribute computers. For the FEM matrix $[\boldsymbol{K}_{\mathrm{II}}]$, $[\boldsymbol{K}_{\mathrm{IS}}]$, $[\boldsymbol{K}_{\mathrm{SI}}]$, $[\boldsymbol{K}_{\mathrm{SS}}]$, and $[\boldsymbol{B}]$, which denotes the corresponding highly sparse FEM matrix. This estimation needs very small memory and CPU time; thus, all the FEM matrices are computed on one processor.

For the surface MoM matrices generated by the BIE are a bottleneck of the FE-BI, which severely limits the capacity of the FE-BI method in dealing with electrically large objects. Although the MLFMM allows for it to solve large problems with limited computational resources, to further improve the capacity of the MLFMM for electrically large objects, one of robust ways is to increase computational resources by assembling parallel computer platforms and, at the same time, by parallelizing MLFMM.

The efficiency of the parallel FE-BI is determined by the efficiency of the parallel BIE part. In the past few years, a series of implementation tricks have been developed for efficiently parallelizing the MLFMM, these tricks are different, but the key issues in those tricks in parallelizing MLFMM are load-balancing and minimizing the communications between the processors. To obtain an efficient parallelization of MLFMM, several issues must be carefully considered to distribute the task equally among the processors. In this paper, we utilize different partitioning strategies for the lower and higher levels of the tree structure. It is natural that the parallel approach for the fine level is to distribute the boxes equally among processors, where the number of boxes is much larger than the number of processors. But it is difficult to achieve good load-balancing for the coarse level with this parallel approach, where the number of boxes is smaller than the number of processors. However, since the box size of the coarse level is big, and the number of far-field patterns for the MLFMM is large, we can partition the far-field patterns equally among all processors while replicating the boxes in every processor as paper [16]. Using this scheme for the parallel MLFMM in the far-field, good load balancing can be achieved.

The interaction matrix in MLFMM is classified

into a near-field interaction matrix and a far-field interaction matrix. After distributing the boxes to each processor in the finest level, the near-field and the far-field interaction lists can be set up in a parallel way. The near-field interaction matrix are calculated directly and stored in memory. For the far-field, the interaction is calculated in a cluster-by-cluster manner. The computation in MLFMM is done in three stages called the aggregation, translation and disaggregation stage.

***Aggregation stage:*** The far-field interaction begins with aggregating basis functions at the finest level to obtain the radiation pattern. Each processor calculates and stores the radiation and receiving patterns of the basis and testing functions included in its local box. Then each processor shifting the radiation pattern to the center of the box in the second finest level, and finally interpolating the deficient radiation pattern to obtain the radiation pattern of the box in the second-finest level. This procedure repeats until the shared levels. In the shared levels, each box is assigned to the same processor. The far-field pattern of each box is distributed equally among processors. In the distributed levels, even though a local interpolation is used, some of the far-field patterns may locate in other processors. Therefore one-to-one communications are needed to get the required data.

***Translation stage:*** The translation stage is one of the most important stages in the parallelization MLFMM; since the boxes are distributed among the processors; one to one communications are required between the processors for the translation stage. To eliminate this overhead, each processor is loaded with extra boxes called the ghost boxes. For example, if box $i$ at processor $a$ needed the far-field samples of box $j$ at processor $b$, maybe another box at processor $a$ also needed the far-field samples of box $j$, to reduce the communication between the processors; we allocate space for the box $j$ at processor $a$. When the far-field samples of box $j$ is received by processor $a$, we store it in the memory, this ensure that the same data is not transferred more than once. In the shared levels, the far-field samples of each cluster are distributed equally among the processors. Therefore, there is no need for communication between the processors at the translation stage in the shared levels.

***Disaggregation stage:*** The disaggregation stage is the generally the inverse of the aggregation stage, the incoming fields are calculated at the centre of each box from the top of the tree structure to the lowest level using the anterpolation. Some of the far-field samples obtained from the anterpolation operation should be sent to other processors in the distributed levels, Similar to the communications during the aggregation stage, this procedure repeats until the finest level.

## III. NUMERICAL RESULTS

In this section, several numerical examples are presented to demonstrate the efficiency of the proposed method. All experiments are performed on two distributed-memory computers; each computer involves 8 processors, each processor has 6 gigabytes (GB) of memory with 3.0GHz clock rate. The resulting linear systems are solved iteratively by the GMRES (30) solver with a relative residual of $10^{-3}$ in double precision.

### A. The accuracy of the proposed method

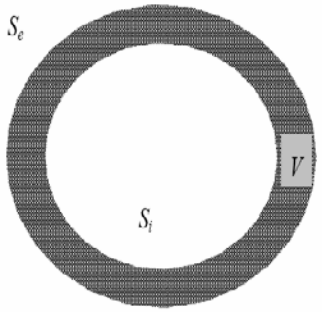


Fig. 1. A PEC sphere coated with a single-layer dielectric.

First, the proposed method is used to analyze scattering from a perfect conductor (PEC) sphere having a diameter of $16\lambda$, the sphere is coated with a 0.1m thick dielectric layer having a relative permittivity of $\varepsilon_r = 2 - i$ and $\mu_r = 1$ as shown in Fig. 1, $S_i$ is the surface of the PEC sphere. A 400MHz plane wave is incident at $\theta_{inc} = 0$, $\phi_{inc} = 0$ and the observed scattering angles are $\theta_s = 0 \sim 180^\circ$ at $\phi_s = 0^\circ$. During the FE-BI calculation for this example, the boundary integral is carried out on the outer surface of the dielectric sphere. The total number of unknowns is 3,540,000, consisting of

2,710,000 for the finite-element and 830,000 for the boundary integral. We first assume that the sphere coated with an air, thus, the bistatic radar cross section (RCS) of the coated sphere is equal to a PEC sphere. As shown in Fig. 2, the numerical result of the bistatic RCS of the sphere is in a good agreement with the Mie solution. Figure 3 shows the bistatic RCS of the sphere coated with dielectric, the dielectric is characterized by $\varepsilon_r = 2 - i$ and $\mu_r = 1$. It can also be found that there is a good agreement with the Mie solution. It involves 52 iterations for this problem to reach convergence.

Solutions are performed on 1, 4, 8, 16, and 32 processors, respectively. Table I lists the total processing times including the setup time and iterative solution parts, and the parallelization efficiency obtained for 4, 8, 16, and 32 processors with respect to 1 processor. Ideally, the speed of a simulation with $P$ processors is $P$ times higher compared with a single processor and the efficiency is 100%. However, from Table I we can see that when the number of processors increases, the efficiency of the FE-BI decreases. This is because with the number of processors increases, although the time for matrix computing decreases correspondingly, the data communication time in the translation stage between the computer increases quickly when the number of processors increases. This becomes the bottleneck in the parallelization of FE-BI.

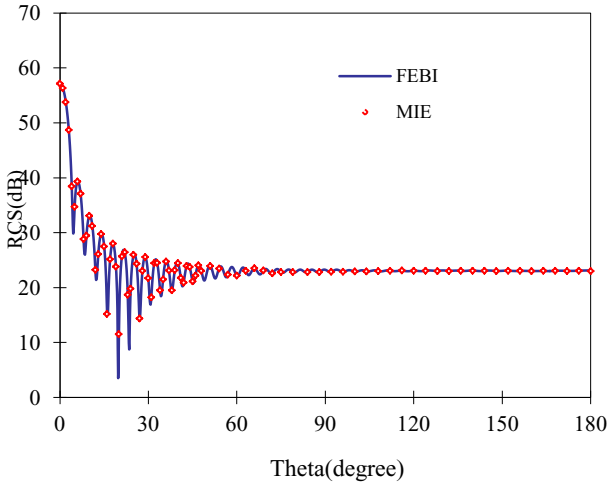


Fig. 2. Bistatic RCS of the conduct sphere at 400 MHz.

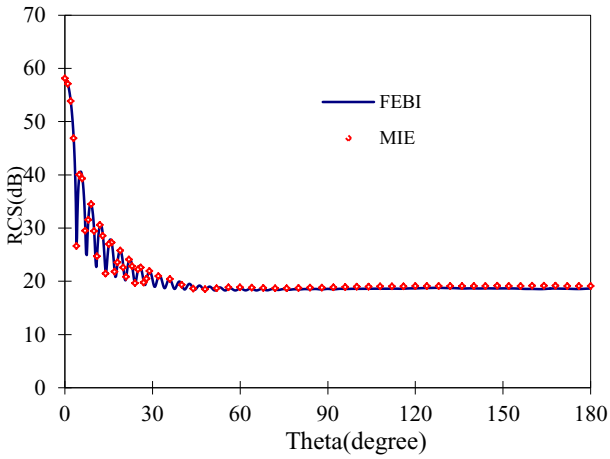


Fig. 3. Bistatic RCS of the coated sphere at 400 MHz.

Table I: Total processing time and parallelization for the solution of the sphere discretized with 3,540,000 unknowns

| Sphere (Radius:16 $\lambda$ , Number of unknowns: 3,540,000) | | | | | |
|---|---|---|---|---|---|
| Number of Processors | 1 | 4 | 8 | 16 | 32 |
| Total time (mintues) | 219 | 58 | 33 | 18 | 11 |
| Efficiency | 100% | 94% | 83% | 76% | 62% |

The second geometry is a coated cylinder with a diameter of 10 $\lambda$ and 20 $\lambda$ high, the cylinder is coated with 0.1m thick dielectric layer having a relative permittivity of $\varepsilon_r = 2 - i$ and $\mu_r = 1$. A 500MHz plane wave is incident at $\theta_{inc} = 0$ and $\phi_{inc} = 0$, and the observed scattering angles are $\theta_s = 0 \sim 180$ at $\phi_s = 0$. After discretisation, the number of unknowns is 3,100,000, consisting of 2,260,000 for the finite-element, and 840,000 for the boundary integral. We first consider the cylinder coated with air, so the RCS of the coated cylinder is equal to a PEC cylinder, Fig. 5 shows the bistatic RCS of the cylinder coated with dielectric $\varepsilon_r = 2 - i$ and $\mu_r = 1$. The numerical results of the bistatic RCS are compared with the body of revolution (BOR). It can be seen from Fig. 4 and Fig. 5 that there is a good agreement between the parallel FE-BI and BOR. It involves 44 iterations for this problem to reach convergence. Table II lists the total processing times including the setup time and iterative solution parts, and the parallelization efficiency obtained for 4, 8, 16, and 32 processors with respect to 1 processor. From the two examples

above, we can see that the parallelization of the FE-BI provides an efficient approach to solve large-scale electromagnetic scattering problems.

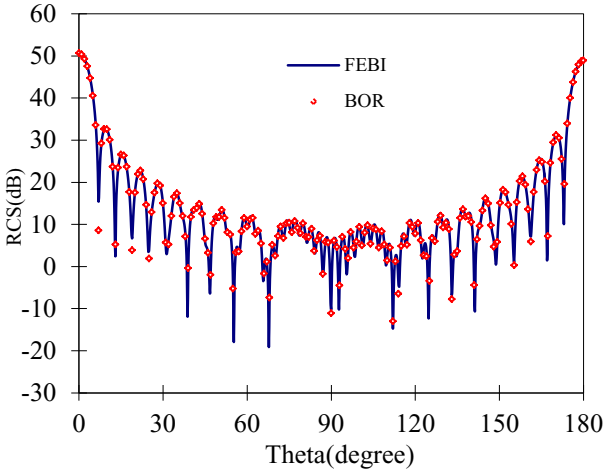


Fig. 4. Bistatic RCS of the PEC cylinder at 500 MHz.

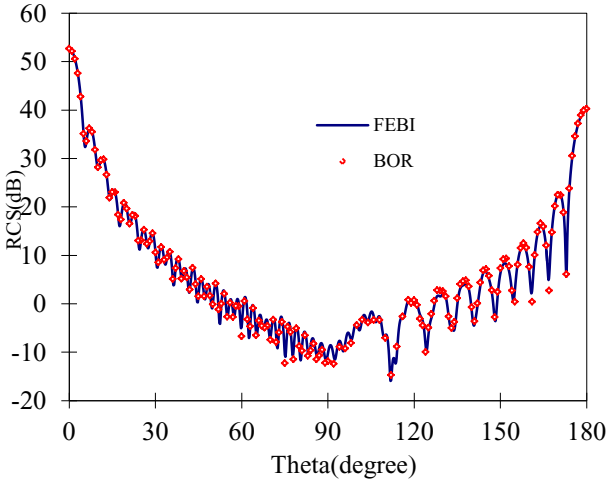


Fig. 5. Bistatic RCS of the coated cylinder at 500 MHz.

Table II: Total processing time and parallelization for the solution of the cylinder discretized with 3,100,000 unknowns

| Cylinder (Diameter of 10 $\lambda$ and 20 $\lambda$ high , Number of unknowns: 3,100,000) | | | | | |
|---|---|---|---|---|---|
| Number of Processors | 1 | 4 | 8 | 16 | 32 |
| Total time (mintues) | 171 | 45 | 26 | 14 | 9 |
| Efficiency | 100% | 95% | 82% | 76% | 59% |

## B. Solution of the real-life problem

To further show the capacity of our parallel FE-BI code, finally, we present the solutions of a real-life problem involving an airplane as shown in Fig. 6. The airplane is coated with a 0.02 wavelength thick dielectric layer having a relative permittivity of $\varepsilon_r = 4$ and $\mu_r = 2 - i$. A 600MHz plane wave is incident at $\theta_{inc} = 120^\circ$, $\phi_{inc} = 270^\circ$ and the observed scattering angles are $\theta_s = 120^\circ$ at $\phi_s = 0 \sim 360^\circ$. The bistatic RCS of the coated airplane is presented in Fig. 6. After the setup, it takes about 24 minutes, and the iterative solution involves 49 iterations to solve the problem on 16 processors.

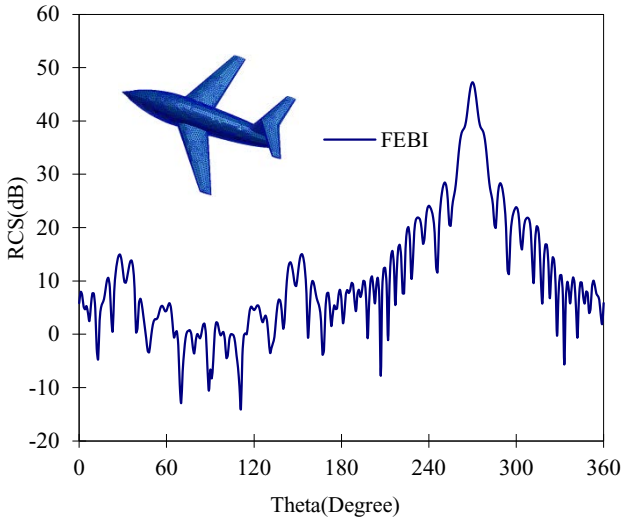


Fig. 6. Bistatic RCS of the coated airplane at 600 MHz.

## IV. CONCLUSIONS

In this paper, we consider fast and accurate solutions of large-scale scattering problems discretized with millions of unknowns using a parallel FE-BI on distributed-memory computers. The parallel near-field preconditioner is used to accelerate the convergence speed of the FE-BI matrix iteration. The capacity of the parallel FE-BI has been demonstrated by computing several coated geometries, i.e. a sphere, a cylinder, and an airplane. From the numerical results, we can see that the proposed parallel FE-BI is efficient for solving the scattering of electrically large objects.

## REFERENCES


[1] M. M. Botha and J. M. Jin, "On the Variational Formulation of Hybrid Finite Element-Boundary Integral Techniques for Electromagnetic Analysis," *IEEE Trans. Antennas and Propag.,* vol. 52, no. 11, pp. 3037-3047, November 2004.

[2] C. Guo and T. H. Hubing, "Development and Application of a Fast Multipole Method in a Hybrid FEM/MoM Field Solver," *Applied Computational Electromagnetic Society (ACES) Journal,* vol. 19, no. 3, pp. 126-134, November 2004.

[3] X. Q. Sheng, J. M. Jin, J. M. Song, C. C. Lu, and W. C. Chew, "On the Formulation of Hybrid Finite-Element and Boundary-Integral Methods for 3D Scattering using Multi-Level Fast Multipole Algorithm," *IEEE Antennas and Propagation Society International Symposium.,* pp. 236 – 239, vol. 1,1998.

[4] X. Q. Sheng, J. M. Jin, J. M. Song, C. C. Lu, and W. C. Chew, "On the Formulation of Hybrid Finite-Element and Boundary-Integral Methods for 3-D Scattering," *IEEE Trans. Antennas and Propag.,* vol. 46, no. 3, pp. 303 – 311, March 1998.

[5] P. Demarcke and H. Rogier, "Hybrid Finite Element-Boundary Integral Method Accelerated by the NSPW-MLFMA," *Electromagnetic Theory (EMTS),* 2010 URSI International Symposium on, pp. 463 - 466, 2010.

[6] H. Chen, Z. H. Fan, R. S. Chen, Z. N. Jiang, and M. M. Li, "Adaptive Mixed-Form Fast Multipole Method for the Analysis of Electromagnetic Scattering," *Applied Computational Electromagnetic Society (ACES) Journal,* vol. 25, no. 11, November 2010.

[7] R. Coifman, V. Rokhlin, and S. M. Wandzura, "The Fast Multipole Method for the Wave Equation: A Pedestrian Prescription," *IEEE Trans. Antennas and Propag.,* vol. 35, no. 3, pp. 7-12, June. 1993.

[8] J. M. Song, C. C. Lu, and W. C. Chew, "Multilevel fast multipole algorithm for Electromagnetic scattering by large complex objects," *IEEE Trans. Antennas and Propag.,* vol. 45, no.10, pp. 1488-1493, October 1997.

[9] C. C. Lu and W. C. Chew, "A Multilevel Algorithm for Solving Boundary Integral Equations of Wave Scattering," *Micro. Opt. Tech. Lett.,* vol. 7, pp. 466-470, July 1994.

[10] J. M. Song and W. C. Chew, "Multilevel Fast-Multipole Algorithm for Solving Combined Field Integral Equation of Electromagnetic Scattering," *Micro. Opt. Tech. Lett.,* vol. 10, pp. 14-19, Sept. 1995.

[11] J. Liu and J.-M. Jin, "A Highly Effective Preconditioner for Solving the Finite Element Boundary Integral Matrix Equation of 3-D Scattering," *IEEE Trans. Antennas and Propag.,* vol. 50, no. 9, pp. 1212-1221, September 2002.

[12] H. Zhao, J. Hu, and Z. Nie, "Parallelization of MLFMA with Composite Load Partition Criteria and Asynchronous Communication," *Applied Computational Electromagnetic Society (ACES) Journal,* vol. 25, no. 2, pp. 167-173, February 2010.

[13] H. Fangjing, N. Zaiping, and H. Jun, "An Efficient Parallel Multilevel Fast Multipole Algorithm for Large-scale Scattering Problems," *Applied Computational Electromagnetic Society (ACES) Journal,* vol. 25, no. 4, pp. 381-387, April 2010.

[14] K. C. Donepudi and J. M. Jin et al, "A higher Order Parallelized Multilevel Fast Multipole Algorithm for 3-D Scattering," *IEEE Trans. Antennas and Propag.,* vol. 49, no. 7, pp. 1069-1078, July 2001.

[15] W. Rankin and J. Board, "A Potable Distributed Implementation of the Parallel Multipole Tree Algorithm." *Proceedings of IEEE Symposimu on High Performance Distributed Computing.,* pp. 17-22,1995.

[16] X. M. Pan and X. Q. Sheng, "A Sophisticated Parallel MLFMM for Scattering by Extremely Large Targets," *IEEE Trans. Antennas and Propag.,* vol. 50, no. 3, pp. 129-138, June 2008.

[17] O. Ergul and L. Gurel, "Efficient Parallelization of the Multilevel Fast Multipole Algorithm for the Solution of Large-Scale Scattering Problems," *IEEE Trans. Antennas and Propag.,* vol. 56, no. 8, pp. 2335-2345, August 2008.

[18] O. Ergul and L. Gurel, "A Hierarchical Partitioning Strategy for an Efficient Parallelization of the Multilevel Fast Multipole Algorithm," *IEEE Trans. Antennas and Propag.,* vol. 57, no. 6, pp. 1740-1750, June 2009.

[19] J. Fostier and F. Olyslager, "An Asynchronous Parallel MLFMA for Scattering at Multiple Dielectric Objects," *IEEE Trans. Antennas and Propag.,* vol. 56, no. 8, pp. 2346-2355, August 2008.

[20] S. M. Rao, D. R. Wilton, and A. W. Glisson, "Electromagnetic Scattering by Surfaces of Arbitrary Shape," *IEEE Trans. Antennas and Propag.,* vol. 30, no. 3, pp. 409-418, 1982.

[21] B. J. Fasenfest, F. Capolino, and D. R. Wilton, "Preconditioned GIFFT: A Fast MoM Solver for Large Arrays of Printed Antennas," *Applied Computational Electromagnetic Society* (*ACES) Journal,* vol. 21, no. 3, pp. 276-283, November 2006.

[22] Z. N. Jiang, Z. H. Fan, D. Z. Ding, R. S. Chen, and K. W. Leung, "Preconditioned MDA-SVD-MLFMA for Analysis of Multi-scale Problems,"

*Applied Computational Electromagnetic Society (ACES) Journal,* vol. 25, no. 11, November 2010.

[23] P. L. Rui, R. S. Chen, D. X. Wang, E. K. N. Yung, "A Spectral Multigrid Method Cobined with MLFMM for Solving Elelctromegnetic Wave Scattering Problems," *IEEE Trans. Antennas and Propag.,* vol. 55, no. 9, pp. 1-7, September 2007.

[24] T. A. Davis "Algorithm 832: UMFPACK, an Unsymmetric-Pattern Multifrontal Method," *ACM Trans. Math.Softw.*, 30, pp. 196-199, 2003.

**Zhen-Hong Fan** was born in Jiangsu, the People's Republic of China in 1978. He received the M.Sc. and Ph.D. degrees in Electromagnetic Field and Microwave Technique from Nanjing University of Science and Technology (NJUST), Nanjing, China, in 2003 and 2007, respectively. During 2006, he was with the Center of Wireless Communication in the City University of Hong Kong, Kowloon, as a Research Assistant. He is currently an associated Professor with the Electronic Engineering of NJUST. He is the author or coauthor of over 20 technical papers. His current research interests include computational electromagnetics, electromagnetic scattering and radiation.

**Ming Chen** was born in Anhui, China. He received the B.S. degree in Physics from Anhui University in 2006, and is currently working toward the Ph.D. degree at Nanjing University of Science and Technology (NJUST), Nanjing, China. His current research interests include computational electromagnetics, antennas, and electromagnetic scattering and propagation.

**Ru-Shan Chen** was born in Jiangsu, P. R. China. He received his B.Sc. and M.Sc. degrees from the Dept. of Radio Engineering, Southeast University, in 1987 and in 1990, respectively, and his Ph.D. from the Dept. of Electronic Engineering, City University of Hong Kong in 2001. He became a Teaching Assistant in 1990 and a Lecturer in 1992. Since September 1996, he has been a Visiting Scholar with the Department of Electronic Engineering, City University of Hong Kong, first as Research Associate, then as a Senior Research Associate in July 1997, a Research Fellow in April 1998, and a Senior Research Fellow in 1999. From June to September 1999, he was also a Visiting Scholar at Montreal University, Canada. In September 1999, he was promoted to Full Professor and Associate Director of the Microwave & Communication Research Center and in 2007, he was appointed Head of the Dept of Communication Engineering, Nanjing University of Science & Technology (NJUST). His research interests mainly include microwave/millimeter-wave systems, measurements, antenna, RF-integrated circuits, and computational electromagnetics. He is a Senior Member of the Chinese Institute of Electronics (CIE). He received the 1992 third-class science and technology advance prize given by the National Military Industry Department of China, the 1993 third class science and technology advance prize given by the National Education Committee of China, the 1996 second-class science and technology advance prize given by the National Education Committee of China, and the 1999 first-class science and technology advance prize given by JiangSu Province as well as the 2001 second-class science and technology advance prize. At NUST, he was awarded the Excellent Honor Prize for academic achievement in 1994, 1996, 1997, 1999, 2000, 2001, 2002, and 2003. He has authored or co-authored more than 200 papers, including over 140 papers in international journals. He is the recipient of the Foundation for China Distinguished Young Investigators presented by the National Science Foundation (NSF) of China in 2003. In 2008, he became a Chang-Jiang Professor under the Cheung Kong Scholar Program awarded by the Ministry of Education, China.

**Dazhi Ding** was born in Jiangsu, the People's Republic of China. He received the B.S. and Ph.D. degrees in Electromagnetic Field and Microwave Technique from Nanjing University of Science and Technology (NJUST), Nanjing, China, in 2002 and 2007, respectively. During 2005, he was with the Center of Wireless Communication in the City University of Hong Kong, Kowloon, as a Research Assistant. He is currently a Lecturer with the Electronic Engineering of NJUST. He is the author or coauthor of over 20 technical papers. His current research interests include computational electromagnetics, electromagnetic scattering and radiation.

# Improving the Convergence of the Wave Iterative Method by Filtering Techniques

**H. Hrizi[1], L. Latrach[1], N. Sboui[1], A. Gharsallah[1], A. Gharbi[1], and H. Baudrand[2]**

[1] Electronics Laboratory, Department of Physics, Faculty of Sciences in Tunis, 2092 El Manar Tunisia
noureddine.sboui@fst.rnu.tn

[2] Electronics Laboratory EN SEEIHT in Toulouse France

***Abstract*** ─ Among the numerical methods used in the electromagnetic modeling of high frequency electronic circuits, we include the wave concept iterative method. In this paper, we propose to improve the convergence speed of this method when modeling a complex structure. This method requires a maximum number of iterations, noted "Nmax", to achieve the convergence to the optimal value. Our goal is to reduce the number of iterations calculated by this method to the value "Nmin" in order to reduce the computing time and to improve the convergence speed. This is done by adding a new algorithm based on filtering techniques.

***Index Terms*** ─ Adaptive and autoregressive Filtering, LMS algorithm, rapid convergence, WCIP method.

## I. INTRODUCTION

The wave concept iterative method (WCIP) has shown efficiency in solving problems of electromagnetism and analysis of radio frequency circuits (RF) [1-4]. Although this method is absolutely convergent, the number of iterations is relatively high and it needs much time for multilayer or complex structures requiring a fine mesh as demonstrated in [5-7], the numerical complexity is related to the number of cells describing the circuit. For example, for structures of 512x512 cells, it takes 24 minutes to perform 1000 iterations. This result is calculated by a machine having a microprocessor Intel(R) Pentium(R) Dual Core CPU 2x2.16GHz and 3 GB of RAM. In this case of complex structures, the WCIP method takes much time to give good results. To avoid this problem, the techniques of adaptive filtering are an effective means to ensure a rapid convergence to the optimal value with a minimal error. Adaptive filtering is a powerful tool in signal processing, digital communications, and automatic control [8-10]. This tool has been applied in various fields such as system identification, prediction, inverse modeling, and the interference cancellation. We use the adaptive algorithm least mean square (LMS) because it is the simplest one in terms of calculation. In addition, it is the most efficient algorithm in terms of minimization criterion of mean squared error [11-12]. To improve the classical WCIP method, we use a new algorithm based on adaptive and autoregressive filtering. We aim at reducing the number of iterations in this method; hence, we reduce the computing time and we improve the convergence speed of the method.

## II. THEORETICAL STUDY

### A. Summary of the WCIP method

The WCIP method is developed in detail in [1-7]. It is an integral method based on the wave concept and it is used in solving problems of electromagnetic modeling. It is noted "WCIP" because it treats the waves instead of electromagnetic fields. It is called iterative because it establishes a recurrent relation between incident and reflected waves. This method is different from

*Submitted On: December 7, 2010*
*Accepted On: September 17, 2011*

the other integral methods (method of moments, Galerkin method ...) because it does not use the scalar product or the matrix inversion. Thus, the method defines two operators; one is defined in the space domain and the other in the spectral domain. The fast Fourier mode transformation (FMT) and the reverse transformation $FMT^{-1}$ insure the transition from one area to another. Applied in guided spaces, it allows us to define the impedance seen by the source of a waveguide. We use this method to study the electromagnetic modeling of a frequency selective surface (FSS) having a complex structure as in Fig. 1.

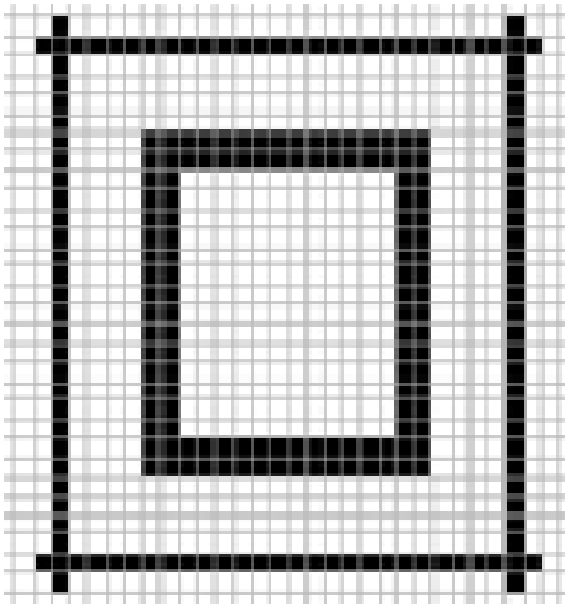

Fig. 1. Unit cell of an FSS structure.

The convergence of the WCIP method is reached after a maximum number of iterations called "Nmax". In our study, we will try to minimize the number of iterations calculated by this method to the value "Nmin" in order to have a fast and better convergence with a minimum calculation time. The remaining iterations until “Nmax” will be treated by a new adaptive filtering algorithm which provides a rapid convergence towards the best result with minimum error. This reduces the computation time and improves the convergence speed of this method. It is important to clarify the definition of the term "convergence speed" that will be the time to run the number of iterations required to converge "close enough" to the optimal result.

## B. Functional blocks of the new algorithm

The new proposed algorithm is composed of two functional blocks as illustrated by Fig. 2 below. The first block is an autoregressive (AR) filter and the second is an adaptive filtering block.

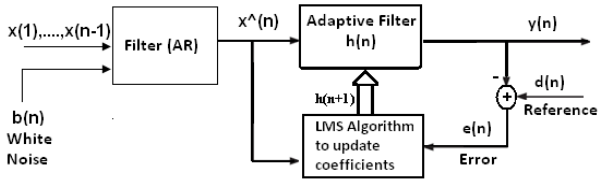


Fig. 2. Functional block of the new algorithm.

The AR filter block is used to model the input signal. This modeling is necessary to predict and regenerate the missing samples in an uncompleted input signal having length equal to “Nmin”. The prediction of $\hat{x}(n)$ at the instant “n” is from the signal at previous time [x(n-1), x(n-2), ...] in addition to the value of the white Gaussian noise at the same time “n”. Thus the prediction and estimation of samples $\hat{x}(n+1)$, $\hat{x}(n+2)$, $\hat{x}(n+3)$... can generate the following sequence samples from $\hat{x}(N\min+1)$ to $\hat{x}(N\max)$. We must choose the optimal order of the AR model that gives the best prediction of the input signal. It remains to estimate the coefficients of the AR filter, this is obtained from the equations of "Yule-Walker” for an AR filter; this uniquely defines the coefficients of the AR filter that are the most suitable for modeling the input signal. The iterations from “1” to “Nmin” are calculated by the classical WCIP method. As in the next equation, the prediction of the signal samples in the following iterations from “Nmin+1” to “Nmax” is realized by the AR filter using a Gaussian white noise $b(n)$ :

$$\hat{x}(n) = \sum_{i=1}^{m} a(i)x(n-i) + b(n), \qquad (1)$$

where $\hat{x}(n)$ is an estimation of $x(n)$ in the iteration” $n$” and “a(1), a(2),……., a(m)” are the coefficients of the AR filter in the following transfer function, the value “m” is the order of this filter :

$$H(z) = \frac{1}{(1 + \sum_{k=1}^{k=m} a(k).z^{-k})}. \qquad (2)$$

Concerning the second block, it is an adaptive filter whose coefficients are changing in function of external signals. A filter is called adaptive if its coefficients are modified and updated in each new sample of the input signal. As in Fig. 2, we have an input x(n), the desired response (reference) d(n) and the error e(n) which is the difference between d(n) and the filter output y(n). The error e(n) serves to control (adjust) the values of filter coefficients. To estimate y(n) from x(n) the adaptive filter uses the programmable coefficients h(n) but to estimate the next sample y(n+1) the filter uses the new coefficients h(n+1) which will be calculated by an adaptive algorithm as we show below. We use the adaptive filter to ensure a rapid convergence to the optimal value with a minimum square error.

In our study, we choose the LMS (least-mean-square) adaptive algorithm developed by Widrow and Hoff in 1959. This algorithm is certainly the most popular adaptive algorithm that exists due to its simplicity [11-12]. As in Fig. 2, the LMS algorithm updates the coefficients $h(n)$ of the adaptive filter transfer function in every new iteration as in the following relation:

$$h(n+1) = h(n) + \mu X(n)e(n) . \quad (3)$$

The coefficients $h(n) = [h_0(n), h_1(n), ....h_{L-1}(n)]^T$ are defined in the iteration "$n$" and the coefficients $h(n+1)$ are defined in the iteration "$n+1$". The input vector is: $X(n) = [x(n), x(n-1), ....., x(n-L+1)]^T$, $L$ is the order of the adaptive filter, "$\mu$" is the adaptation step. The error value "$e(n) = d(n) - y(n)$" is relative to a reference signal $d(n)$. As below, the value $y(n)$ is the output in the iteration "$n$":

$$y(n) = h^T(n)X(n) . \quad (4)$$

The adaptive filter coefficients "$h(n) = [h_0(n), h_1(n), ....h_{L-1}(n)]^T$" are changed in each new iteration until they become stable and equal to "$\mathrm{h_{opt}}$". That's how we define the stability and the convergence of the adaptive filter; it is represented by the next equation:

$$\lim_{n\to\infty} E\{\mathrm{h(n)}\} = \mathrm{h_{opt}} . \quad (5)$$

We aim at finding the condition of the stability and the convergence of the adaptive filter so we have to minimize the following function:

$$\mathrm{J(n)} = \left\|\mathrm{h(n+1) - h(n)}\right\|^2 . \quad (6)$$

We consider the following constraint:

$$\mathrm{h^T}(n+1)X(n) = d(n) . \quad (7)$$

The solution of the problem is obtained by the multiplier λ of Lagrange. In fact, we want to minimize in reference to h(n+1) as in the following equations:

$$\mathrm{J(n)} = \left\|\mathrm{h(n+1) - h(n)}\right\|^2 + \lambda[d(n) - \mathrm{h^T}(n+1)X(n)], \quad (8)$$

$$\frac{\partial J(n)}{\partial h(n+1)} = 2[h(n+1) - h(n)] - \lambda X(n) = 0_{Lx1} . \quad (9)$$

We obtain the next result:

$$h(n+1) = h(n) + \frac{\lambda}{2} X(n) . \quad (10)$$

The constraint becomes as in the next equation:

$$d(n) = h^T(n+1)X(n) = h^T(n)X(n) + \frac{\lambda}{2} X^T(n)X(n) . \quad (11)$$

Also, we have:

$$d(n) = e(n) + y(n) = e(n) + h^T(n)X(n) . \quad (12)$$

Thus, we find the following expression of λ:

$$\lambda = \frac{2e(n)}{X^T(n)X(n} .$$

(13)

Finally, we obtain the equation of the LMS algorithm:

$$\mathrm{h(n+1) = h(n) + \frac{\lambda}{2} X(n) = h(n) + \frac{1}{X^T(n)X(n} X(n)e(n)} . \quad (14)$$

In fact, to have the best control of the filter coefficients updating, we introduce a positive factor $\alpha$ , $(0 < \alpha < 2)$ :

$$h(n+1) = h(n) + \frac{\alpha}{X^T(n)X(n} X(n)e(n) . \qquad (15)$$

In comparison with equation (3), we obtain the following result:

$$\frac{\alpha}{X^T(n)X(n} = \frac{\alpha}{\sum_{l=0}^{l=L-1} x^2(n-l)} \approx \frac{\alpha}{L\sigma_x^2} = \mu . \quad (16)$$

This value $\mu$ is called the adaptation step of the LMS algorithm. We consider the condition of $\alpha$ $(0 < \alpha < 2)$. It gives the next relation:

$$0 < \mu < \frac{2}{L\sigma_x^2} . \qquad (17)$$

This condition ensures the LMS algorithm convergence and the adaptive filter stability. So the best choice of the adaptation step $\mu$ provides the stability and the convergence of the LMS algorithm to the optimal results with minimal error as in equation (17). This choice of the adaptation step $\mu$ depends on the power $\sigma_x^2$ of the input signal and the adaptive filter order $L$. Thus, the performance of the LMS algorithm depends on three factors: the adaptation step $\mu$, the power of the input signal, and the order $L$ of the adaptive filter.

As shown in Fig. 3, the idea is to add to the classical WCIP algorithm a new algorithm describing an AR filter and an adaptive filter based on the LMS algorithm. Thus, the algorithm of the new method will be noted as an adaptive wave concept iterative process (A-WCIP). We introduce an input sequence that has a length equal to "Nmin", the iterations of this sequence are calculated by the WCIP algorithm.

The new "A-WCIP" algorithm predicts the result of the remaining iterations until achieving the convergence to the optimal value with "Nmax" iterations.

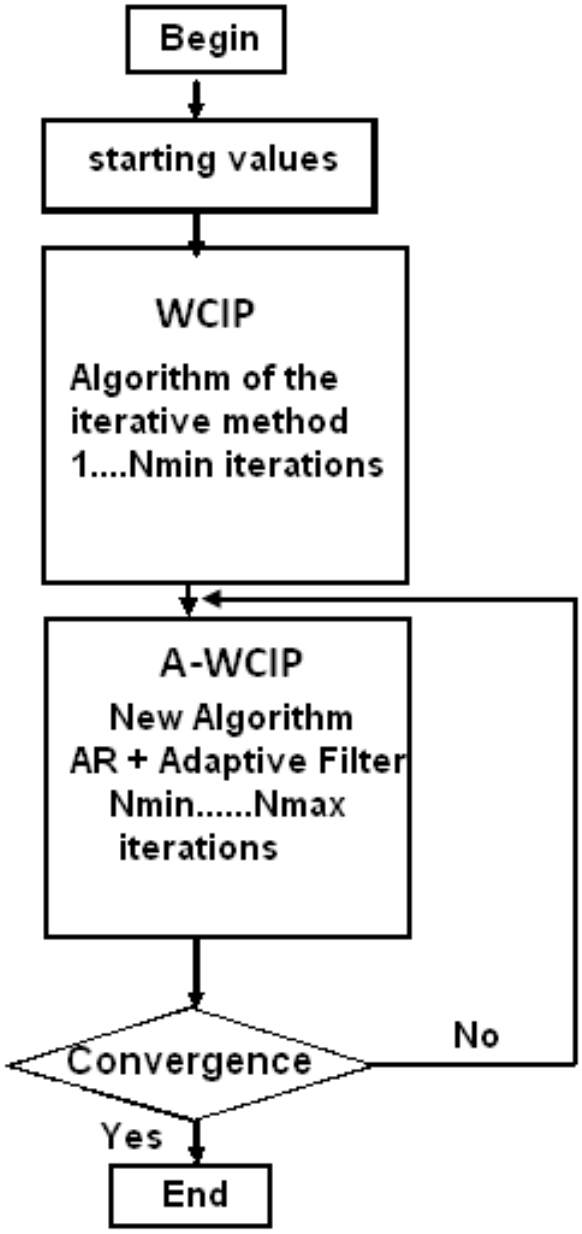


Fig. 3. The new "A-WCIP" approach.

The best conditioning of our system is done first by a good selection of the optimal order "m" of the AR filter. Then, it is done by a good choice of the adaptation step "$\mu$" of the LMS algorithm, which depends on the input energy $\sigma_x^2$ and the order "$L$"of the adaptive filter. We conclude that the conditioning of this system is mainly based on the nature of the input signal. This is an important point of our approach because it ensures that the system is adapted to all types of input signals that vary from one frequency to another, especially that

we are testing a wide frequency range. This provides stability and convergence of our system, whatever the conditions of the input signal.

Therefore, with the new algorithm, we improve the convergence of the classical iterative method which will calculate only a limited number of iterations equal to "Nmin". The number "Nmax" of iterations needed to reach the convergence will be achieved by the new A-WCIP algorithm which is a very rapid algorithm. Thus, an important gain in computing time will be accomplished by this new approach.

## III. SIMULATIONS AND RESULTS

The input signal $x(n)$ in the last theoretical part will be designated in the next part by the coefficients of the diffraction matrix $S_{11}$ or $S_{21}$.

### A. Convergence improvement

In Figs. 4 and 5, the coefficients $S_{11}$ and $S_{21}$ are represented as a function of the number of iterations by both methods ("WCIP" and "A-WCIP") in order prove that the new method gives also good results.

First, the classical WCIP method uses only the WCIP algorithm to calculate "Nmax=200" iterations. We conclude that the maximum number of iterations necessary to achieve the convergence is equal to 200 iterations. This number is relatively high because the electronic circuit studied has a complex structure. So in this case to have good results, the wave iterative method needs a big number of iterations (Nmax=200 iterations). Thus, this method takes much time to obtain the optimal result. So to reduce the computing time necessary to have a good result, we need to reduce the number of iterations calculated by the WCIP algorithm to the value "Nmin". The remaining iterations are calculated by the new "A-WCIP" algorithm, which does not take much time to reach the convergence.

Then, we use the new "A-WCIP" method to calculate the same maximum number of iterations (Nmax=200 iterations). This new method is composed of two algorithms: the classical WCIP algorithm to which we add the new filtering algorithm. In the new "A-WCIP" approach, the number of iterations calculated by the classical WCIP algorithm is reduced to "Nmin=50" iterations. The maximum number of iterations is achieved by the new filtering algorithm (Nmax=200). The adaptive filter takes the output of the AR filter as input. As a result, the final output of the global new system "A-WCIP" must converge to the optimal values of $S_{11}$ and $S_{21}$ with minimum errors.

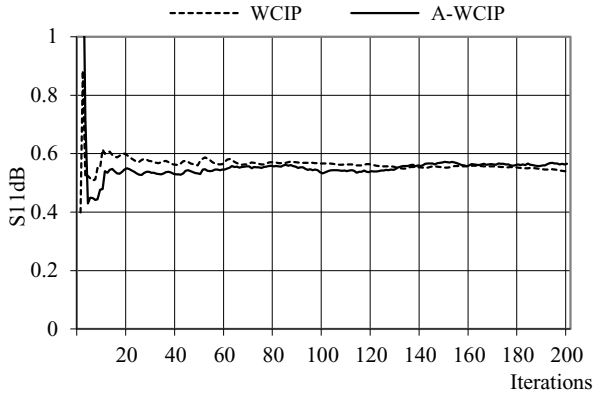


Fig. 4. Variation of $S_{11}$ by both methods.

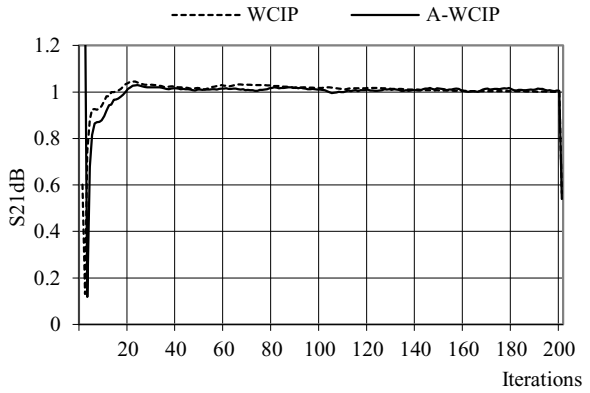


Fig. 5. Variation of $S_{21}$ by both methods.

Here, we compare the results given by the two methods in order to prove that the new "A-WCIP" method provides good results. Of course, the new approach is faster than the classical one because it uses the WCIP algorithm to calculate "Nmin=50" iterations and it uses the filtering algorithm to calculate the remaining iterations until reaching the number "Nmax=200". However, the classical method uses only the WCIP algorithm to calculate 200 iterations which takes much time.

### B. Comparison in terms of computing time

In the next paragraph, we use the classical WCIP method to calculate 1000 iterations (Nmax=1000) and we use the new "A-WCIP"

method to calculate the same number of iterations (Nmax=1000, Nmin=400). In Table 1, we observe an important gain in convergence time when calculating $S_{11}$ and $S_{21}$ values after 1000 iterations by the two methods. This gain of time is provided by the new "A-WCIP" method because we add a rapid adaptive filtering algorithm "LMS" in this method. The mesh used in this structure is 512x512 cells. We use a machine having a microprocessor Intel(R) Pentium(R) Dual Core CPU 2x2.16GHz and 3GB of RAM.

Table 1: Comparison of time between the two methods

| **The used method** | **Computing time (mn)** |
|---|---|
| "A-WCIP" | 10 mn |
| "WCIP" | 24 mn |
| Gain of Time | 58,33% |

### C. Comparison in terms of the average error

In Table 2, we represent the values of the average error calculated on the reflection and transmission coefficients $S_{11}$ and $S_{21}$. The band of frequency is from 10GHz to 15GHz. The error is calculated when using the new "A-WCIP" filtering method in comparison with the classical WCIP method. We choose two different values of "Nmin" (25 and 50). The number "Nmin" represents the minimum number of iterations calculated by the WCIP algorithm in the new "A-WCIP" method. The maximum number of iterations is equal to 200 iterations. We find that the average error in comparison with the classical WCIP method is limited. This proves the effectiveness and robustness of our approach. Finally, we ensure the convergence to an optimum result very close to the desired value with a minimum average error in each frequency.

Table 2: Comparison in terms of the average error

| **Nmax** | **Nmin** | **Average error $S_{11}$ (dB)** | **Average error $S_{21}$ (dB)** |
|---|---|---|---|
| 200 | 25 | 2,782 | 0,893 |
| 200 | 50 | 1,646 | 0,399 |

### D. Variation of $S_{11}$ and $S_{21}$ calculated by the new method in function of frequency

In Figs. 6 and 7, we represent the variation of the coefficients $S_{11}$ and $S_{21}$ in function of frequency. These coefficients are calculated by our new "A-WCIP" method. These results are compared with those calculated by the classical "WCIP" method in order to prove that our results are close to the best and optimal results. The maximum number of iterations calculated by the two methods is equal to 200 iterations (Nmax=200). In the new method, we test two values of "Nmin" (25 and 50 iterations) and we obtain good results in comparison with the WCIP method.

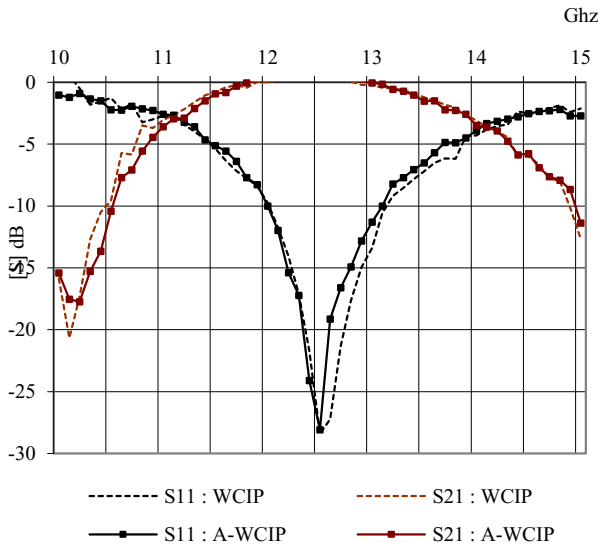


Fig. 6. $S_{21}$ and $S_{11}$variations in function of frequency with Nmax= 200, Nmin= 25 iterations.

Thus in our new A-WCIP method, the WCIP algorithm is used to calculate only 25 or 50 iterations and the following iterations are calculated by the adaptive filtering algorithm until achieving 200 iterations. In the classical WCIP method, we use only the WCIP algorithm to calculate all the 200 iterations. If we compare the two methods, we conclude that the number of iterations in the classical WCIP algorithm is reduced from 200 to 25 iterations in the new approach. Thus, we achieve our principal goal which is the reduction of the number of iterations in the WCIP algorithm. That is why we obtain a good reduction of computing time in the new A-WCIP method. Finally, we obtain a fast convergence with minimum average error.

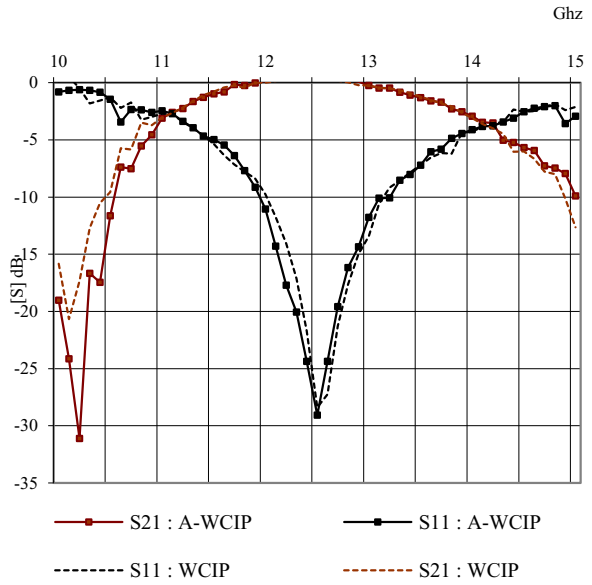


Fig. 7. $S_{21}$ and $S_{11}$variations in function of frequency with Nmax= 200, Nmin= 50 iterations.

## IV. CONCLUSION

In our study, the convergence speed of the classical WCIP algorithm has been improved. In the new "A-WCIP" method, the WCIP algorithm has to calculate only a minimum number "Nmin" of iterations that can be reduced from 200 to 25 iterations. The remaining iterations after "Nmin" are treated by the new filtering algorithm to achieve the convergence to the optimal value after "Nmax=200" iterations. Thus, we have a very fast convergence in comparison with the classical WCIP method in which the WCIP algorithm calculates all the 200 iterations. Finally, a very significant reduction in computing time has been obtained. Thus, we ensure a rapid convergence with a limited average error hence the efficiency and robustness of our new approach.

## REFERENCES

[1] N. Sboui, A. Gharsallah, H. Baudrand, and A. Gharbi, ''Glabal Modeling of Microwave Active Circuits by an Efficient Iterative Procedure," IEE Proc-Microw. Antenna Propag., vol. 148, no. 3, June 2001.

[2] N. Sboui, A. Gharsallah, H. Baudrand, and A. Gharbi, ''Design and Modeling of RF MEMS Switch by Reducing the Number of Interfaces,'' Microw. and Opt. Technol. Lett vol. 49, no. 5, pp. 1166-1170, May 2007.

[3] N. Sboui, L. Latrach, A. Gharsallah, H. Baudrand, and A. Gharbi, "A 2D Design and Modeling of Micro strip Structures on Inhomogeneous Substrate," Int. Journal of RF and Microwave Computer –Aided Engineering, vol. 19, no. 3, pp. 346-353, May 2009.

[4] N. Sboui, A. Gharsallah, H. Baudrand, and A. Gharbi, "Global Modeling of Periodic Coplanar Waveguide Structure for Filter Applications Using an Efficient Iterative Procedure," Microwave and Opt. Technol. Lett, vol. 43, no. 2, pp. 157-160, 2004.

[5] N. Sboui, A. Gharsallah, A. Gharbi, and H. Baudrand, "Analysis of Double Loop Meander Line by Using Iterative Process," Microw. Optical Technical Letters, vol. 26, pp. 396-399, June 2000.

[6] L. Latrach, N. Sboui, A. Gharsallah, H. Baudrand, and A. Gharbi, "A Design and Modelling of Microwave Active Screen Using a Combination of the Rectangular and Periodic Waveguides Modes," Journal of Electromagnetic Waves and Applications, vol. 23, no. 11-12, 2009.

[7] L. Latrach, N. Sboui, A. Gharsallah, H. Baudrand, and A. Gharbi, "Analysis and Design of Planar Multilayered FSS with Arbitrary Incidence," Applied Computational Electromagnetic Society Journal, vol. 23, no. 2, pp. 149-154, June 2008.

[8] W. Byrne, P. Flynn, R. Zapp, and M. Siegel, "Adaptive Filter Processing in Microwave Remote Heart Monitors," IEEE Trans. on Biomed. Enginee., vol. BME-33, no. 7, July 1986.

[9] J. Luukko and K. Rauma, "Open-Loop Adaptive Filter for Power Electronics Applications," IEEE Trans. on Indust. Electronics, vol. 55, no. 2, Feb. 2008.

[10] A. Ogunfunmi and A. M. Peterson, "On the Implementation of the Frequency-Domain LMS Adaptive Filter," IEEE Trans. On Circuits, Systems-II Analog, and Digital Signal Processing, vol. 39, no. 5, May 1992.

[11] M. Godavarti and O. Alfred Hero, "Partial Update LMS Algorithm," IEEE Trans. on Signal Processing, vol. 53, no. 7, July 2005.

[12] J. Daniel Allred, H. Yoo, V. Krishnan, W. Huang, and V. David Anderson, "LMS Adaptive Filters using Distributed Arithmetic for High Throughput," IEEE Trans. on Circuits and Systems-I REGULAR PAPERS, vol. 52, no. 7, July 2005.

# Perforated Dielectric Resonator Antenna Reflectarray

**S. H. Zainud-Deen[1], S. M. Gaber[2], A. M. Abd-Elhady[3], K. H. Awadalla[1], and A. A. Kishk[4]**

[1]Department of Electronics and Electrical Engineering
Menoufia University, Meouf, Egypt
anssaber@yahoo.com

[2] Department of Electronics and Computer Engineering
Higher Cairo Institute for Engineering, Egypt

[3] Department of Electronics and Electrical Engineering
Benha University, Egypt

[4] Department of Electrical Engineering
University of Mississippi, USA

***Abstract*** ─ A wideband perforated rectangular dielectric resonator antenna (RDRA) reflectarray is presented. The arrays of RDRA are formed from one piece of materials. Air-filled holes are drilled into the material around the RDRA. This technique of fabricating RDRA reflectarray using perforations eliminates the need to position and bond individual elements in the reflectarray and makes the fabrication of the RDRA reflectarray feasible. The ground plane below the reflectarray elements is folded as a rectangular concave surface so that an air-gap is formed between the RDRA elements and the ground plane in order to increase the bandwidth. Full-wave analysis using the finite integration technique is applied. Three cases are studied. In the first one, the horn antenna is placed at the focal point to illuminate the reflectarray and the main beam in the broadside direction. In the second one, the horn antenna is placed at the focal point and the main beam at ±30 degrees off broadside direction. In the third one, an offset feed RDRA reflectarray is considered. A variable length RDRA provides the required phase shift at each cell on the reflectarray surface. The normalized gain patterns, the frequency bandwidth, and the aperture efficiency for the above cases are calculated.

***Index Terms*** ─ Dielectric resonator, reflectarray, wideband array.

## I. INTRODUCTION

High gain antennas are desired in various applications, such as satellite communications, radar systems, and radio astronomy observations. Traditionally, large parabolic reflector antennas are selected for the systems mentioned above. However, these antennas are bulky, heavy, and their geometrical shape tends to be distorted during the implementation. Microstrip reflectarrays are good alternatives to reflectors for space applications because of their low profile, simple manufacturing process, added functionalities, and low cost especially for beam shaping applications. The microstrip reflectarray is made up of a reflective array of printed patches with a certain tuning on the phase of the reflected wave to produce a focused or shaped beam when illuminated by a primary feed. By varying the resonant properties of the elements making up the array, it is possible to introduce a graded progressive phase variation upon reflection across the surface of the reflectarray. Methods to control the phase of the re-radiated wave include using elements with variable sizes [1], patches with different stub lengths [2], slots with variable lengths at the ground plane or loaded on the patch [3,4], and the variable rotation angle technique [5]. One of the primary disadvantages of microstrip reflectarrays is their relatively narrow gain bandwidth for a single layer design [6]. The

*Submitted On: March 10, 2011*
*Accepted On: October 15, 2011*

bandwidth of the microstrip reflectarray is mainly restricted by the microstrip elements, the differential phase delay, the array element spacing, and the feed antenna bandwidth [7]. Bandwidth can be somewhat improved by using a more complex structure consisting of multiple layers of substrates and stack patches [8].

Rectangular dielectric resonator antenna (RDRA) was proposed by Long et al. [9] in 1983. RDRAs offer many advantages, such as low-profile, low-cost, ease of excitation, and high radiation efficiency. RDRAs offer high radiation efficiency even if they are used in high frequency applications. This is because of the low ohmic losses and there are no surface waves when using this kind of antennas. Since the surface waves are not supported by RDRAs, the scan blindness problems with large microstrip arrays can be solved. The scan blindness is the signal loss due to the mutual coupling and it occurs when the main beam is steered to the low elevation angles used in microstrip array. Moreover, when the RDRA is made of a high permittivity material with slight dissipation losses, it can handle high power. The high power capability is considered as an advantage when used in radar applications [10]. RDRAs may be used at a wide range of frequencies starting from 55MHz up to 94 GHz. RDRAs can be formed in different shapes offering more design flexibility, they can be rectangular, cylindrical, hemispherical, or other regular shapes. Many investigations have been reported about the RDRAs with different shapes and their characteristics have been examined [11]. Reflectarray antennas realized by rectangular and crossed dielectric resonator for linear and circular polarizations are investigated in [12-14]

One current disadvantage of RDRAs in large arrays is related to fabrication: each individual RDRA element must be located and bonded at the appropriate position in the array. For high frequency applications where the size of the elements becomes small, their exact location becomes more critical, and this approach may not be practical. The perforated technique was used in the DRA array in order to make an array from one dielectric sheet by perforating materials between the elements [15, 16]. The effective permittivity of the dielectric resonator was altered with the perforated air-filled holes drilled into its substrate material. Perforated structure was first proposed for gain enhancement in the dielectric Fresnel lens design [17]. The concept of perforated RDRA was tested experimentally in [18].

In recent years, one major aspect of the research with RDRAs has focused on the bandwidth enhancement, and many techniques have been proposed to broaden the operating bandwidth of the RDRAs [19-21]. However, these techniques of impedance-bandwidth enhancement are all on the expense of the complex DR structures. In [22], a novel wideband rectangular RDRA is proposed, where an air gap is introduced between the rectangular RDRA and the ground by adopting a rectangular concave dip in the ground plane. It shows that using a concave dip in the ground plane instead of a planar ground plane has broadened the impedance bandwidth to 1.4 times.

This paper reports a new type of reflectarray using rectangular RDRA elements for linear polarization. Perforated substrate and rectangular concave dipped ground plane are used to improve the gain bandwidth of the reflectarray. This paper extends the investigation of perforated RDRAs by examining the performance of perforated RDRAs in the reflectarray structure.

## II. THE ARRAY STRUCTURE

Figure 1 gives the coordinate system of the reflectarray geometry with solid ground plane. The reflectarray is composed of 23x23 elements and is covering an area of 31.05 x 31.05 $cm^2$. The unit cell in reflectarray antenna consists of rectangular RDRA supported on ground plane. Each RDRA element has a width W=7 mm, a height h=3.2 mm, a relative dielectric constant, $\varepsilon_r$ =10.9, and a variable length L. This RDRA is designed to operate at 12 GHz. The cell size $L_1$= $W_1$=13.5 mm. The feeder is a pyramidal horn with dimensions of 59.9 x 29.9 x 49.5 $mm^3$. The horn antenna is placed at the focal point, 320 mm away from the reflecting surface.

A possible geometry of RDRA reflectarray fabricated by perforating a single dielectric sheet is shown in Fig. 2. The unit cell in the reflectarray antenna consists of rectangular RDRA supported on a perforated ground plane. The RDRAs are formed from a single dielectric sheet by perforating selected areas of the material.

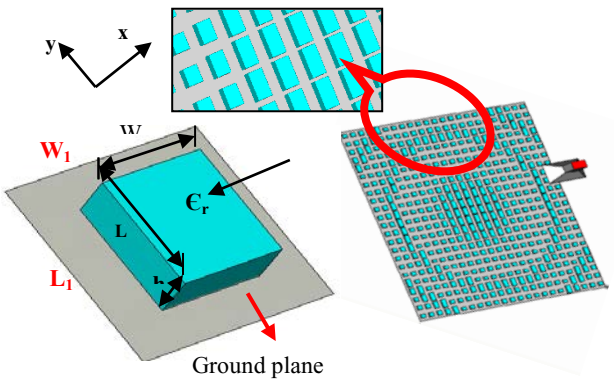


(a) RDRA cell with solid GP (b) Broadside RDRA reflectarray with solid GP

Fig. 1. The geometry of the RDRA reflectarray with solid ground plane.

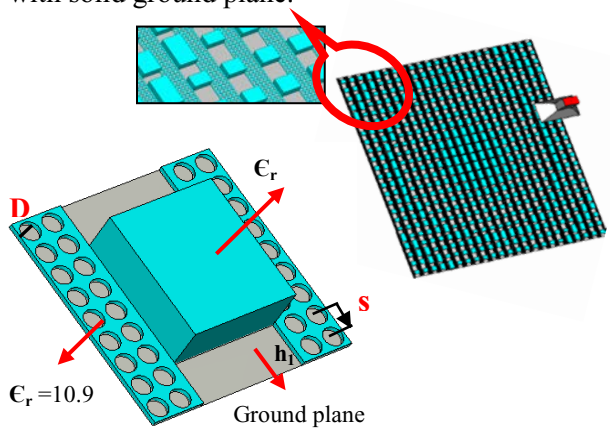


(a) RDRA cell with perforated ground plane (b) Broadside RDRA reflectarray with perforated ground plane

Fig. 2. The geometry of the RDRA reflectarray with perforated ground plane.

The diameter and spacing of the holes determines the effective dielectric constant of the material surrounding the RDRAs. This technique of fabricating RDRAs using perforations is intended for reflectarray applications, eliminating the need to position and bond individual elements and making the fabrication of RDRA reflectarray feasible. For perforated ground plane, S=1.5 mm, D=1.2 mm and $h_1$=0.35 mm. The relationship between the RDRA element length and reflecting phase shift at 12 GHz for the unit cell in Fig. 1 and Fig. 2 was determined using CST simulator [23] that depends on the finite integration technique [24, 25]. The software is used to model an infinite array of RDRA elements. This procedure assumes that the reflection from an element RDRA surrounded by RDRAs of different sizes can be approximated by the reflection of an element in an infinite array of identical RDRAs. A normal incident plane wave on a periodic infinite array was assumed to calculate the reflection phase change of one element. A typical plot of the reflection phase shift as a function of RDRA element length is shown in Fig. 3. The radius of the hole of the perforated ground plane, the distance between two holes and numbers of holes are optimized to give the results in Fig. 3. The tuning range of the reflection phase shift is 360 degrees. Excellent agreement is obtained between the results of RDRA on solid ground plane and that for perforated ground plane. Results of this study indicate that this perforation technique is a promising alternative for one using individual RDRAs elements.

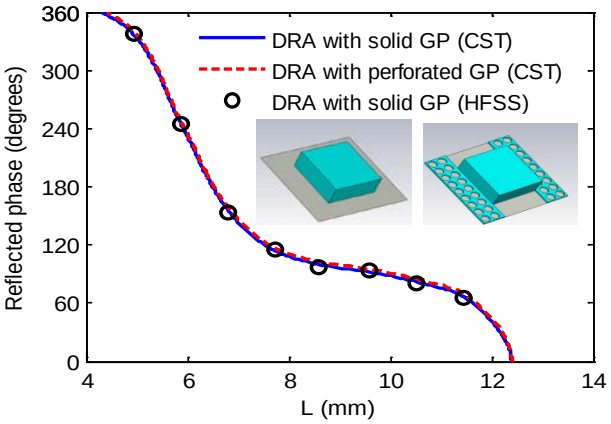


Fig. 3 Reflected phase of RDRA cell versus its length at 12 GHz, h= 3.2mm, W= 7mm, S = 1.5mm, $h_1$=0.35mm , D = 1.2mm, and $L_1$= $W_1$= 13.5mm.

## III. NUMMERICAL RESULTS

Numerical calculations were performed by using the CST simulator, the horn, and reflectarray elements are included in the calculation. The required phase shifts of reflectarray elements in the broadside RDRA reflectarray is shown in Fig. 4. The normalized gain patterns for the broadside feed reflectarray at 12 GHz in E-plane and H-plane are shown in Fig. 5. The half-power beamwidth (HPBW) of the main beam is 5 degrees. A peak gain of 29.9 dB is predicted at $\theta=0^o$. Figure 6 shows peak gain variation with frequency. A 9.1% bandwidth is achieved with 1 dB gain variation (11.4 GHz–12.5 GHz). The aperture efficiency is 50.1%.

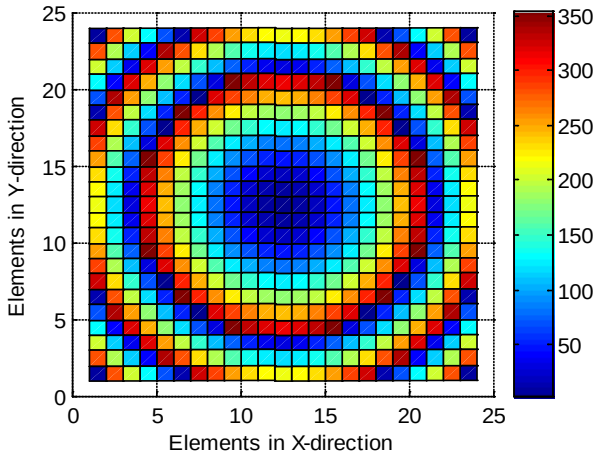


Fig. 4. The required phase shifts of the reflectarray elements.

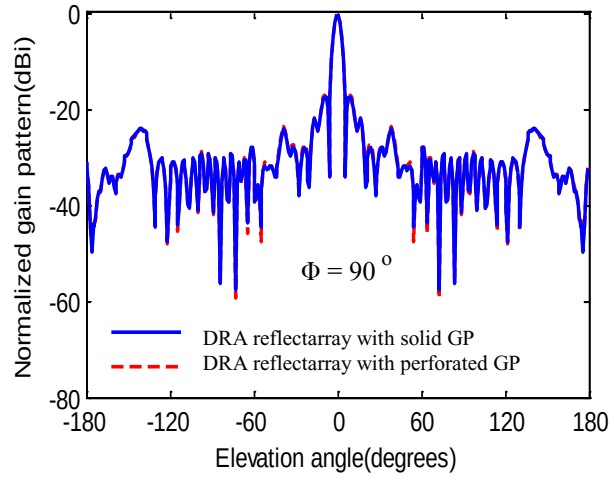


(a)

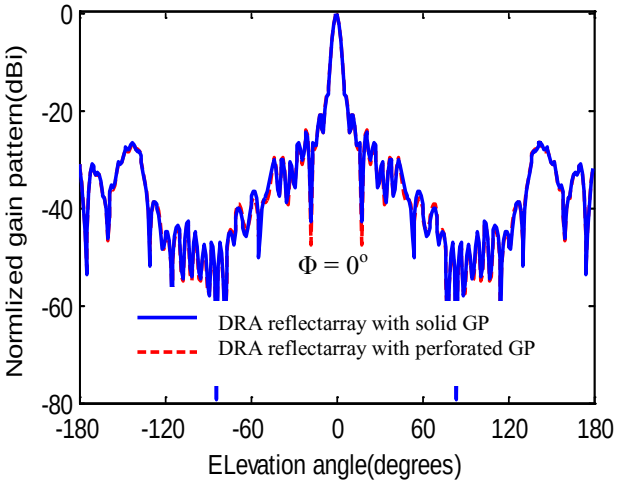


(b)

Fig. 5. Normalized gain patterns at 12GHz for 23×23 broadside reflectarray. (a) E-plane. (b) H-plane.

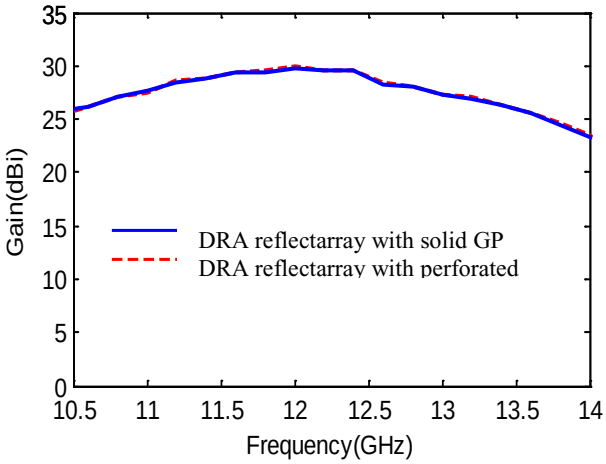


Fig. 6. The required phase shifts of the reflectarray elements.

The schematic drawing and the close up picture of the reflectarray elements with perforated ground plane and rectangular concave dip are shown in Fig. 7. An air gap is introduced between the RDRA and the ground by adopting a concave ground plane in each cell. The rectangular concave surface has dimensions $L_c$=4.5 mm and $h_c$=2 mm.

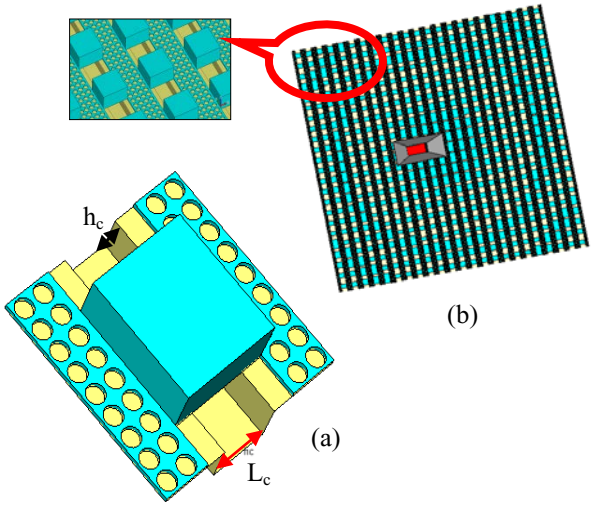


Fig. 7. (a) DRA cell with perforated GP and rectangular concave. (b) Broadside RDRA reflectarray with perforated GP and rectangular concave.

The normalized gain patterns in the E-plane and H-plane at 12 GHz frequency are illustrated in Fig. 8. The 3-dB beamwidth is 4 degrees. A peak gain of 30.6 dB is predicted at $\theta=0^o$. Simulated gain patterns at different frequencies to check the bandwidth of the array are shown in Fig. 9.

At the extreme frequencies, the gain patterns are similar with some increase in sidelobe levels and little gain variations. Figure 10 shows peak gain variation with frequency. Note the gain bandwidth is substantially improved to about 13.33%, the reflectarray can cover from 11.4 GHz to 13 GHz with 1 dB gain variation. The aperture efficiency is 57.88%.

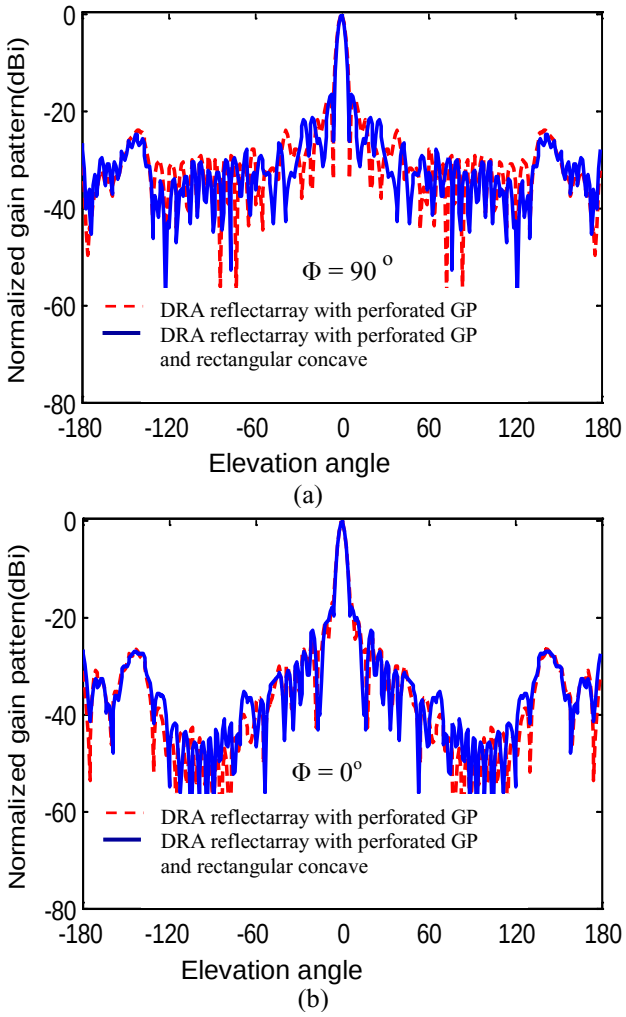


Fig. 8. Normalized gain patterns at 12GHz for 23×23 broadside RDRA reflectarray: (a)E-plane. (b) H-plane.

To minimize the feed blockage of a center-fed configuration, the reflected beam must be directed out of broadside direction. Another RDRA reflectarray with a concave ground plane with 30 degrees off broadside beam direction was designed. Figure 11 shows the construction of the 30 degrees off broadside RDRA reflectarray with perforated ground plane and rectangular concave dip.

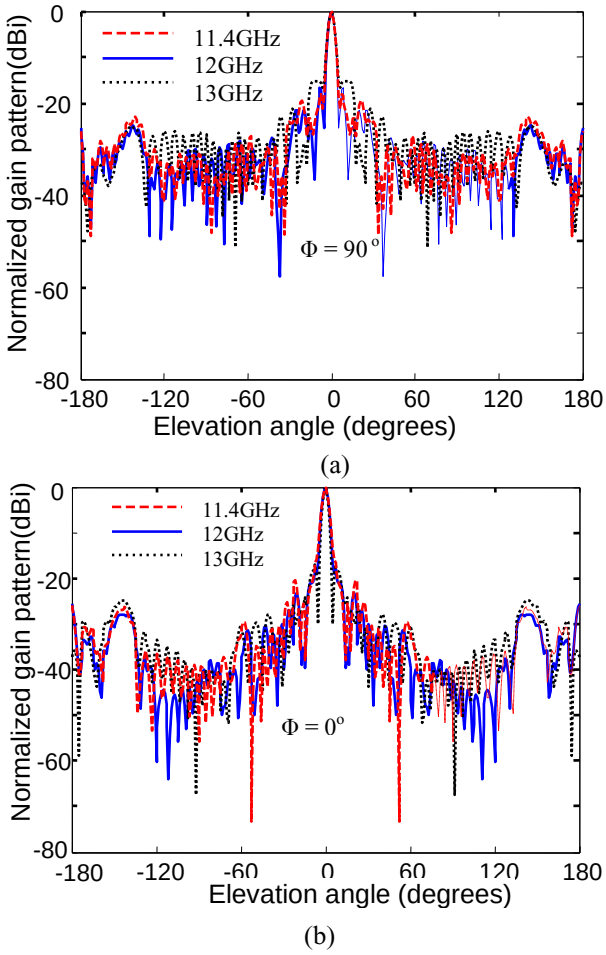


Fig. 9. Normalized gain patterns at different plane for 23×23Broadside RDRA reflectarray. (a) E-plane. (b) H-plane.

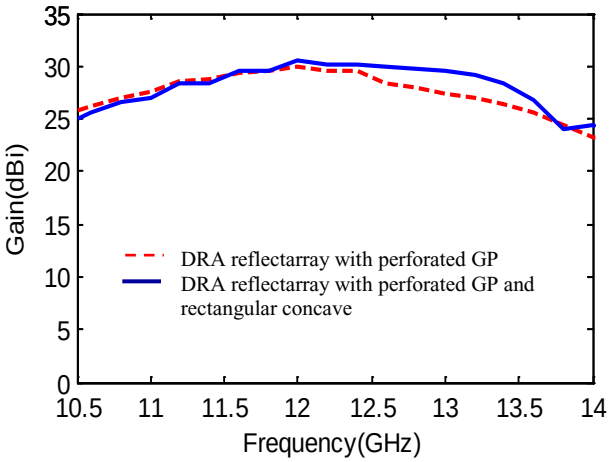


Fig. 10. Peak gain versus frequency for 23×23broadside RDRA reflectarray.

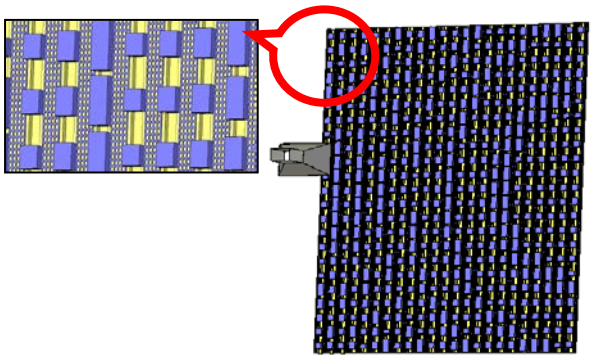

Fig. 11. 30 degrees off broadside RDRA reflectarray with perforated GP and rectangular concave.

Figure 12 shows the gain pattern on the H-plane (x-z plane). It achieves a peak gain of 29 dB. The 3 dB beamwidth is 5.5 degrees. Figure 13 shows peak gain variation with frequency. For the frequency band between 11.4 to 12.4 GHz, the gain is varying by 1 dB only. An 8.3% bandwidth is achieved. Again, the reflectarray is designed to produce main beam with tilt angle of -30 degrees from the broadside direction. The gain pattern at 12 GHz frequency for -30 degrees off broadside direction RDRA reflectarray is shown in Fig. 14. Figure 15 shows peak gain variation with frequency. The aperture efficiency is 40.6%.

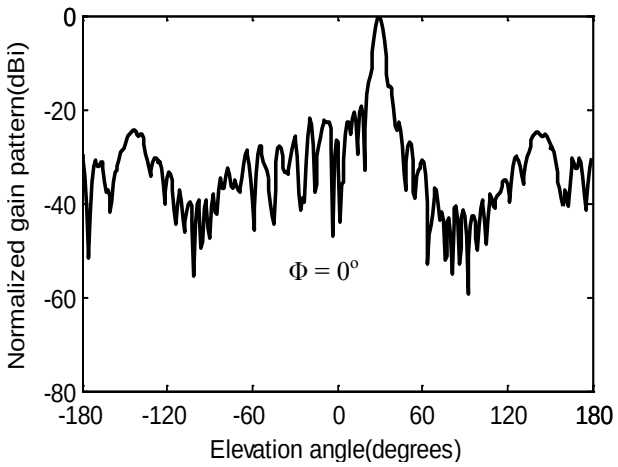


Fig. 12. H-plane patterns at 12GHz for 30 degrees off broadside RDRA reflectarray.

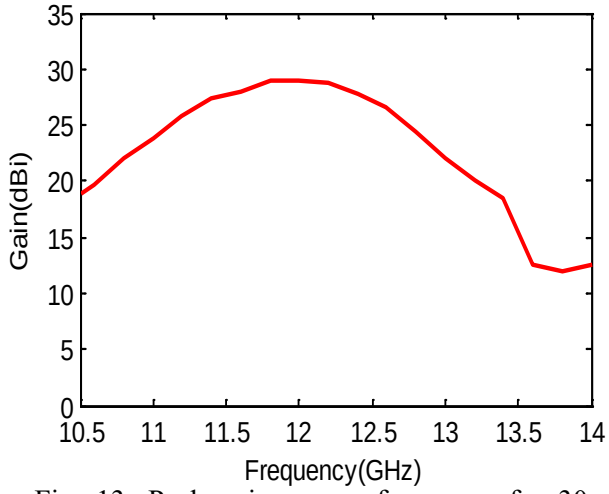


Fig. 13. Peak gain versus frequency for 30 degrees off broadside RDRA reflectarray.

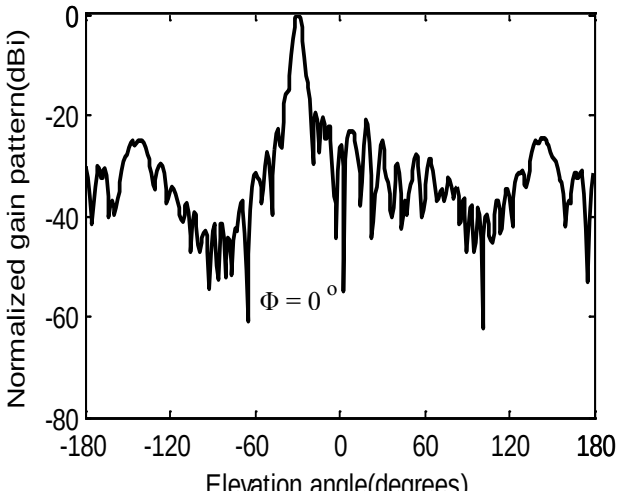


Fig. 14. H-plane patterns at 12GHz for -30 degrees off broadside RDRA reflectarray.

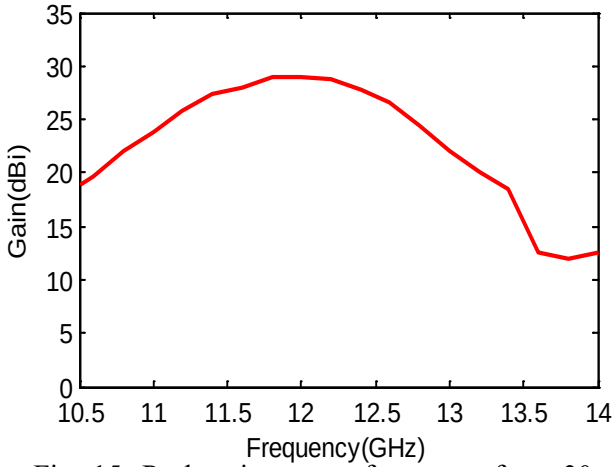


Fig. 15. Peak gain versus frequency for -30 degrees off broadside RDRA reflectarray.

Figure 16 shows the offset feed RDRA reflectarray with perforated ground plane and rectangular concave dip. The reflectarray is fed by linearly polarized pyramidal horn antenna at a tilt angle of 17° as to minimize the feeder blockage. The gain patterns in the E-plane and H-plane at 12 GHz frequency are illustrated in Fig. 17. The 3-dB beamwidth is 5.5 degrees. The computed peak gain is 30 dB. Figure 18 shows the peak gain variation with frequency. For the frequency band between 11.4 to 12.7 GHz, the gain is varying by 1 dB only. The gain bandwidth is approximately 10.9% and the aperture efficiency is 47%.

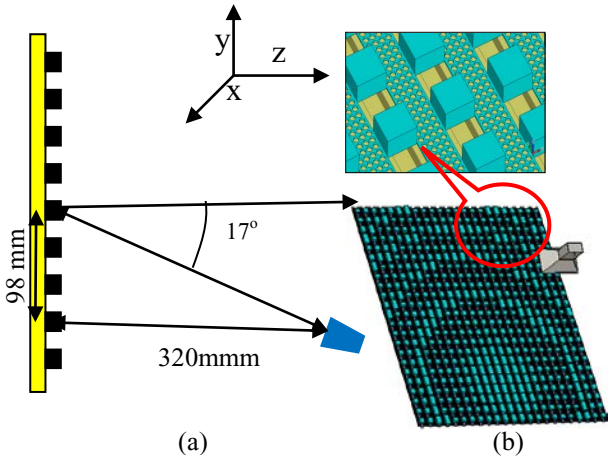


Fig. 16. (a) Offset feed broadside reflectarray with solid GP. (b) Offset feed broadside reflectarray with perforated Gp and rectangular.

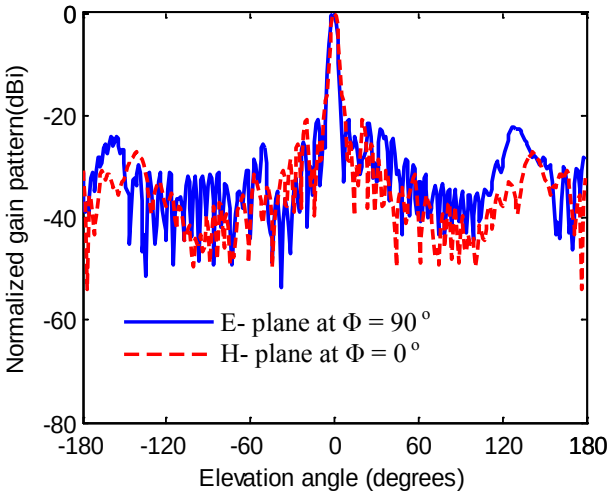


Fig. 17. Normalized gain patterns at 12GHz for 23×23 broadside RDRA reflectarray.

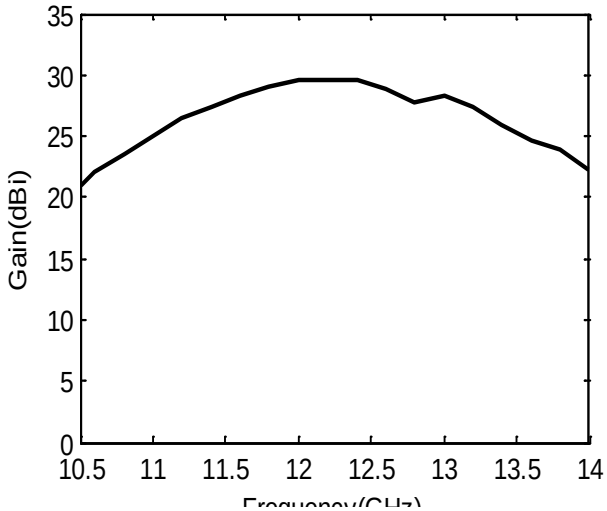


Fig.18. Peak gain versus frequency for 17 degrees offset feed broadside RDRA reflectarray.

## VI. CONCLUSION

Perforated dielectric resonator antenna reflectarray was designed for linear polarization at 12 GHz. The RDRA elements are formed from one piece of material. Air-filled holes are drilled into the material around the RDRA. The performance of the array is similar to that achieved by one using individual RDRA. A novel wideband RDRA is proposed, where an air gap is introduced between the RDRA and ground by introducing a concave ground plane dip. A 23x23 reflectarray is used. The reflectarray is illuminated by a linearly polarized pyramidal horn. In this paper, a variable length RDRA was used to achieve the required phase shift at each cell on the reflectarray surface. To avoid the feed blockage of a center-fed configuration, the reflectarray was center fed and the beam peak location was designed to be ± 30 degrees off boresight. Also, the antenna was offset fed by a linear polarized pyramidal horn. The gain bandwidth is approximately 10.9% and the aperture efficiency is 47%.

## REFERENCES

[1] D. M. Pozar and T. A. Metzler, "Analysis of a Reflectarray Antenna using Microstrip Patches of Variable Size," *Electronics Letters*., vol. 29, pp. 657-658, Apr. 1993.

[2] R. D. Javor, X. D. Wu, and K. Chang, "Design and Performance of a Microstrip Reflectarray Antenna," *IEEE Trans. Antennas Propagat*., vol. 43, pp. 932-939, Sept. 1995.

[3] M. R. Chaharmir, J. Shaker, M. Cuhaci, and A. Sebak, "Reflectarray with Variable Slots on Ground Plane," *IEE Proceedings Microwave Antennas Propagat.*, vol. 150, pp. 436-439, Dec. 2003.

[4] D. Cadoret, A. Laisné, R. Gillard, and H. Legay, "A New Reflectarray Cell using Microstrip Patches Loaded with Slots," *Microwave Optical Technol. Lett.*, vol. 44, no. 3, pp. 270-272, Feb. 2005.

[5] J. Huang and R. Pogorzelski, "A Ka-Band Microstrip Reflectarray with Elements Having Variable Rotation Angles," *IEEE Trans. Antennas Propagat.*, vol. 46, pp. 650-656, May 1998.

[6] J. Huang, "Analysis of a Microstrip Reflectarray Antenna for Microspacecraft Applications," *TDA Progress Report* 42-120, pp.153-173, Feb. 1995.

[7] J. Huang and J. A. Encinar, Reflectarray Antennas, John Wiley & *Sons, Inc., Hoboken,* NJ, 2007.

[8] J. A. Encinar, "Design of Two-Layer Printed Reflectarrays using Patches of Variable Size," *IEEE Trans. Antennas Propagat.*, vol. 49, pp.1403-1410, Oct. 2001.

[9] S. A. Long, M. W. McAllister, and L. C. Shen, "The Resonant Cylindrical Dielectric Cavity Antenna," *IEEE Trans. Antennas Propagat*, vol. 31, no. 3, pp. 406-412, March 1983.

[10] A. A. Kishk, "Dielectric Resonator Antenna, A Candidate for Radar Applications," *IEEE Radar Conference*, pp. 258-264, 2003.

[11] A. Petosa, *Dielectric Resonator Antenna Handbook,* Artech House, Boston, USA, 2007.

[12] S. H. Zainud-Deen, A. M. Abd-Elhady, A. A. Mitkees, and A. A. Kishk, "Design of Dielectric Resonator Reflectarray using Full-Wave Analysis," *26th National Radio Science Conference (NRSC 2009),* Faculty of Engineering, Future Univ., Egypt, B10, pp. 1-9, March 2009.

[13] A. M. Abd-Elhady, S. H. Zainud-Deen, A. A. Mitkees, and A. A. Kishk, "X-Band Linear Polarized Aperture-Coupled DRA Reflectarray," *2010 International Conference on Microwave and Millimeter Wave Technology*, Chengdu, China, 2010.

[14] A. M. Abd-Elhady and W. Hong "Ka-band Linear Polarized Air Via Reflectarray," *1st Middle East Conference on Antennas and Propagation, (MECAP),* Cairo, Egypt, 2010.

[15] A. Petosa, A. Ittipiboon, and S. Thirakoune, "Perforated Dielectric Resonator Antennas," *Electronics Letters*, vol. 38, no. 24, pp. 1493-1495, Nov. 2002.

[16] A. Petosa, S. Thirakoune, and A. Ittipiboon, "Array of Perforated Dielectric Resonator Antennas," *IEEE Antennas and Propagation Symp., Monterey*, CA, USA, pp. 1006-1009, 2004.

[17] A. Petosa, A. Ittipiboon, and S. Thirakoune, "Investigation on Arrays of Perforated Dielectric Fresnel Lenses," *IEE Proceedings Microwave Antennas Propagat.,* vol. 153, no. 3, pp. 270-276, June 2006.

[18] R. Chair, A. A. Kishk, and K. F. Lee, "Experimental Investigation for Wideband Perforated Dielectric Resonator Antenna," *Electronics Letters*, vol. 42, no. 3, Feb. 2006.

[19] A. A. Kishk, Y. Yin, and W. Glisson, "Conical Dielectric Resonator Antennas for Wideband Applications," *IEEE Trans. Antennas Propagat.*, vol. 50, no. 4, pp. 469–474, April 2002.

[20] R. Chair, A. A. Kishk, K. F. Lee, and C. E. Smith, "Wideband Flipped Staired Pyramid Dielectric Resonator Antennas," *Electronics Letters*., vol. 40, pp. 581–582, May 2004.

[21] A. A. Kishk, "Experimental Study of Broadband Embedded Dielectric Resonator Antennas Excited by a Narrow Slot," *IEEE Antennas Wireless Propagat. Lett.*, vol. 4, pp. 79–81, 2005.

[22] X.-L. Liang and T. A. Denidni, "Wideband Rectangular Dielectric Resonator Antenna with a Concave Ground Plane," *IEEE Antennas Wireless Propagat. Lett.*, vol. 8, pp. 367-370, 2009.

[23] CST Microwave Studio, *www.cst.com*, 2009.

[24] L. Di Rienzo, N. Ida, and S. Yuferev, "Surface Impedance Boundary Conditions of High Order of Approximation for the Finite Integration Technique," *Applied Computational Electromagnetic Society (ACES) Journal*, vol. 22, no. 1, pp. 53-59, March 2007.

[25] A. Ciccomancini Scogna and M. Strydom, "Computational Electromagnetic Field Calculation by Means of Finite Integration," *Applied Computational Electromagnetic Society (ACES) Journal*, vol. 22, no. 2, pp. 17-41, 2007.

# Design of a Planar UWB Antenna with New Band Enhancement Technique

**Rezaul Azim[1, 2], Mohammad Tariqul Islam[2], and Norbahiah Misran[1]**

[1] Department of Electrical, Electronic, and Systems Engineering
Universiti Kebangsaan Malaysia, 43600 UKM Bangi, Malaysia
rezaulazim@yahoo.com

[2] Institute of Space Science (ANGKASA)
Universiti Kebangsaan Malaysia, 43600 UKM Bangi, Malaysia
titareq@yahoo.com

***Abstract*** ─ A planar antenna and a technique for enhancing its bandwidth for UWB applications have been proposed in this paper. The proposed antenna which has a compact structure and the total size of 30 × 22 $mm^2$ consists of a square patch and a partial ground plane. Numerical study shows that the bandwidth of the proposed antenna can be controlled mainly by the patch size and width of the feeding line. The cutting triangular shape slots on the top edge of the ground plane help to increase the bandwidth by 43.6% (3.89 GHz). The measured -10 dB return loss bandwidth of the proposed antenna ranges from 2.95 GHz to 15.45 GHz which covers the entire UWB band. The nearly stable radiation pattern with a maximum gain of 5.9 dBi makes the proposed antenna suitable for being used in UWB communication.

***Index Terms*** ─ Microstrip feed-line, partial ground plane, planar antenna, ultra-wideband.

## I. INTRODUCTION

Ultra-wideband (UWB) technology has been regarded as one of the most prolific wireless technologies having the capability of revolutionizing a high data rate transmission. A number of new techniques to support high data rate in wireless communication for the next generation technologies have been rapidly increasing after the release of 3.1–10.6 GHz unlicensed band for UWB communication by the Federal Communication Commissions (FCC). UWB also have wide applications in short range and high speed wireless communication, such as ground penetrating radars, microwave imaging system, wireless local area networks (WLAN), communication systems for military, and short pulse radars for automotive even or robotics and in all these applications antenna with wideband plays a vital role. As a key component of UWB systems, the antennas with wide bandwidth have been investigated by both academia and industry.

The design of a compact, lightweight antenna for wideband applications is still a major challenge. Many coplanar waveguide-fed and microstrip line- fed antennas have been proposed for UWB applications. Several bandwidth enhancement techniques-have also been considered, such as associating several radiating elements to form an array antenna[1], using log periodic arrays in which the different elements are deduced from a homothetic ratio in order to reach the desired bandwidth [2], introduction of a capacitive coupling between the radiating element and the ground plane [3], addition of slots on the side of the radiating element [4-5], using a tapered feed line [6], notching the ground plane and/or the patch [7-8], modifying the shape of the radiating element and adding a shorting pin [9]. However the antennas mentioned above are not planar structured as they were set above a big ground plane which resulted in increased antenna size and cannot be easily embedded into wireless devices or cannot be integrated with other RF circuits.

*Submitted On: June 13, 2011*
*Accepted On: October 26, 2011*

Recently other techniques have also been examined to enhance the antenna bandwidth, including the insertion of a modified trapezoid-shaped slot in the patch [10], the use of trident-shaped feeding strip and a tapered impedance transformer [11] and embedding a pair of notches in the two lower corners of the patch and the notch structure in the upper edge of the ground plane [12]. The use of two bevel slots on the upper edge and two semicircle slots on the bottom edge of the ground plane [13], insertion of a rectangular slot on the top side of the ground plane[14] and a half-bowtie radiating patch with staircase shape [15] have also been reported for the bandwidth enhancement. Techniques such as adding steps to the lower edge of the patch [16], inclusion of circular ring-shaped patch [17], the insertion of additional stub to the one side of circular patch [18], and addition of the slit on one side of the radiating element [19] have also been reported for bandwidth enhancement in planar monopole antennas. Recently, it was demonstrated in [20] that by etching two rectangular slots in the ground plane, the total bandwidth of the monopole antenna can be significantly increased up to the surface current distribution to ameliorate the antenna's impedance bandwidth.

Many of the above mentioned printed UWB antennas consisting of a planar radiator and system ground plane is essentially an unbalanced design, where the electric currents are distributed on both the radiator and the ground plane so that the radiation from the ground plane is inevitable. Therefore, the performance of the printed UWB antenna is significantly affected by the shape and size of the ground plane in terms of the operating frequency, impedance bandwidth, and radiation patterns [21- 23].

In this paper, a technique to enhance the bandwidth of a microstrip-fed planar monopole antenna has been proposed. The monopole antenna fed by a 50Ω microstrip feed line is fabricated on the FR4 substrate. To improve the bandwidth, the top side of the partial ground plane has been modified to form a sawtooth-shape and by this modification it is found that, the bandwidth is enhanced by 43.6% compared the initial design. The proposed antenna is easy to be integrated with microwave circuitry for a low manufacturing cost.

## II. ANTENNA DESIGN

The geometries of square patch planar monopole antennas that are considered in this paper are shown in Fig. 1. The planar monopole antennas are chosen in this paper due to their remarkably compact size, low spectral power density, simplicity, stable radiation characteristics, and easy to fabricate and very easy to be integrated with microwave circuitry for low manufacturing cost. A shortcoming of this structure is limited bandwidth. The objectives of this paper are to modify the structure of the ground plane and incorporate the techniques to increase the bandwidth.

The configuration in Fig. 1 (a) is the first antenna used for a parametric study. The almost square patch with dimension $W \times L$ is printed on a $30 \times 22$ $mm^2$ low cost FR4 PCB substrate of thickness 1.6 *mm*, with relative permittivity 4.6 and loss tangent 0.02. The radiating patch is 6.75 *mm* away from the left edge of the substrate. A microstrip feed line of width $w_f$ which is 3.75 *mm* away from the left edge of the substrate is also printed in the same side of the patch as a radiator. The partial ground plane having side length $L_G$ is printed on the other side of the substrate. The length of the microstrip feed line is fixed at 7.25 *mm* to achieve a 50Ω characteristic impedance.

The patch size of the proposed antenna is the first parameter to optimize for widest bandwidth while the other parameters are kept constant. The results in Fig. 2 show that, the increase of patch size is resulting in a reduction of the bandwidth. It is also seen that that decrease in patch size from a certain value gives a better return loss value at the cost of bandwidth reduction. A patch size of 14.5 $\times$ 14.75 $mm^2$ is taken as the optimized value.

The width of microstrip feed line is the most sensitive parameter which influences the bandwidth most. It can be seen from the Fig. 3 that, when the feeding width increases the bandwidth decreases dramatically giving two distinct frequency bands with lower return loss values. The bandwidth also decreases when the feeding width is decreased from a certain value. A feeding width of 3 *mm* is the best fitting to give the widest impedance bandwidth.

To compact the antenna it is desirable that the ground plane must have the minimum size. The dimensions of the partial ground plane are the next parameters to be optimized which influence the

return loss as well as the bandwidth. A change in the ground plane size offers a simple way to improve the antenna performance, but at the cost of increasing the antenna volume. From Fig. 4, it is observed that, when the ground plane dimensions increases the bandwidth decreases. Again, the bandwidth is decreases with the decrement of ground plane dimension from a certain value though it provides the lowest return loss values. The ground plane dimension of 30 × 7.5 $mm^2$ is taken as the optimized value to give the widest bandwidth. From the optimization of these parameters it is seen from the Fig. 5 that, the antenna without any slot in the ground plane is capable tuning from 3.04 GHz to 11.94 GHz providing an impedance bandwidth of 8.89 GHz.

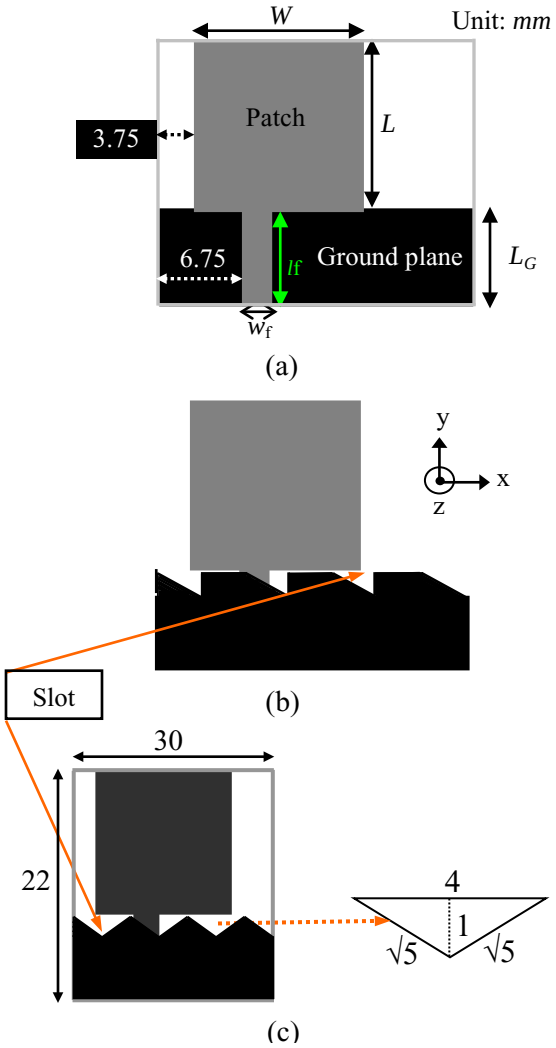


Fig. 1. Geometries of the proposed planar antenna (a) initial design, (b) with straight slots, and (c) final design with sawtooth shape slots in ground plane.

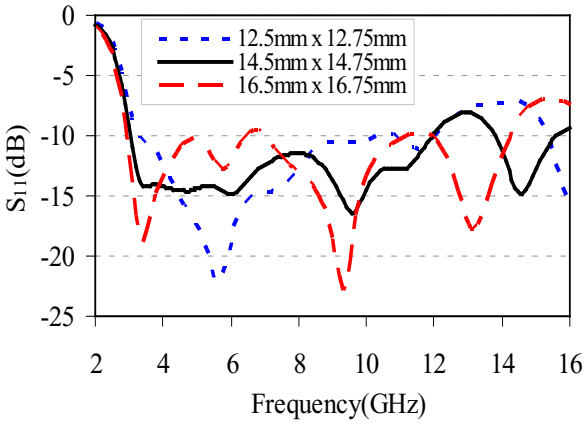


Fig. 2. Simulated *S* parameters for different patch sizes (*W*×*L*).

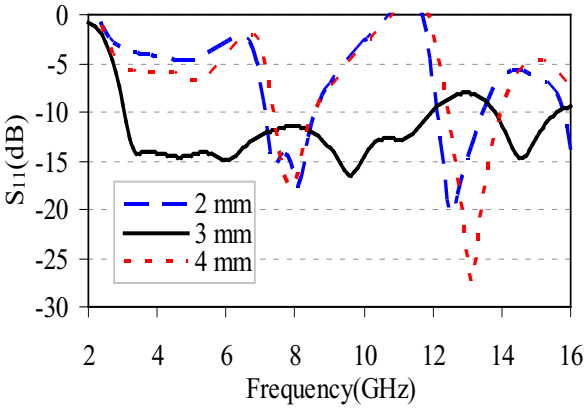


Fig. 3. Simulated *S* parameters for different feeding width, $W_f$.

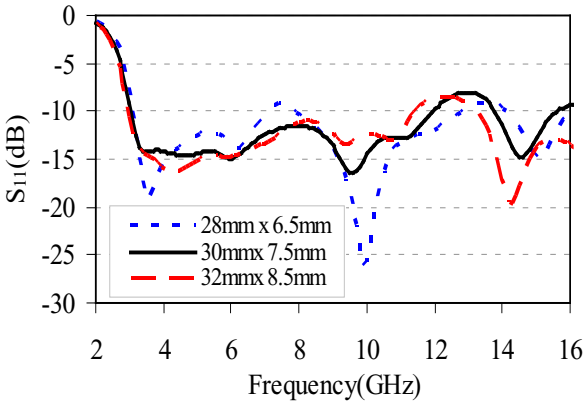


Fig. 4. Simulated *S* parameters for different ground plane size (*W*×$L_G$).

To improve the bandwidth of the antenna, triangular shape slots are introduced at the top side of the ground plane. The resultant antenna is shown in Fig. 1(b). The return losses in Fig. 5 shows that the triangular slots of dimension $2 \times 1 \times \sqrt{5}$ $mm^3$ has small effect on the lower edge frequency while it increase the upper edge frequency of the operating band and the antenna can provide an impedance bandwidth of 9.48 GHz operating from 2.96 to 12.44 GHz. Compared to the initial design without slot in the ground plane, the antenna with triangular slots on the top edge of the ground plane can enhance the bandwidth by 0.59 GHz.

To enhance the bandwidth further, the top edge of the partial ground plane is reshaped to form a sawtooth shape top edge, as shown in Fig. 1(c). The optimized dimension of the triangular shape slot is $4 \times \sqrt{5} \times \sqrt{5}$ $mm^3$. From the return loss curve shown in Fig. 5, it is seen that the modified ground plane with sawtooth shape top edge has little effect on lower edge frequency while it significantly influences the upper edge frequency of the operating band. It is also seen from Fig. 5 that the antenna with modified ground plane can be operated from 2.92 GHz to 15.70 GHz providing an impedance bandwidth of 12.78 GHz. It is also observed that, introduction of triangular shaped slots not only widens the bandwidth but also reduces the return loss. The insertion of slots in the top edge of the ground plane increases the gap between the radiating patch and the ground plane and as a result the impedance bandwidth increases further due to extra electromagnetic coupling in between the radiating element and the ground plane. Compared to the result associated with the initial design, the antenna with a modified sawtooth shape ground plane can increase the bandwidth by 43.6% (3.89 GHz) as shown in Fig. 5. From Figs. 2-5, the effect of a triangular shape slots on the top edge of the partial ground plane can be thoroughly comprehended. From Fig. 2, it can be seen that the first two resonant frequencies are tunable by the patch size and square patch capable of supporting multiple resonant modes. Second, it is also clear from the Figs. that the third resonance is determined by slots on the ground plane and the slots almost have no effect on the first two resonant frequencies. As the size of the slots increases, the return loss value at third resonant frequency also increases.

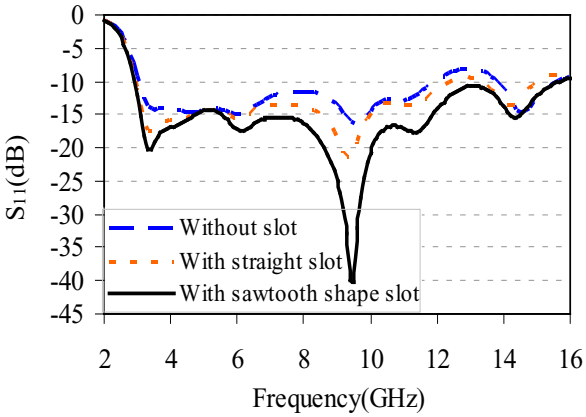


Fig. 5. *S* parameters without, with straight and with sawtooth shape slot in the ground plane.

## III. EXPERIMENTAL RESULTS AND DISCUSSION

The performance of the proposed antenna has been analyzed and optimized by commercially available method of moments based full-wave electromagnetic simulator IE3D ver. 12.3 from Zeland. The antenna was subsequently prototyped for experimental verification as shown in Fig. 6. The antenna has been measured in an anechoic chamber using Satimo hybrid StarLab 16 near field antenna measurement system and Agilent E8362C PNA series vector network analyzer [24]. To achieve untruncated extent near field sampling using a probe array, the spherical scanning system was utilized for this near-field antenna measurement system and is shown in Fig. 7.

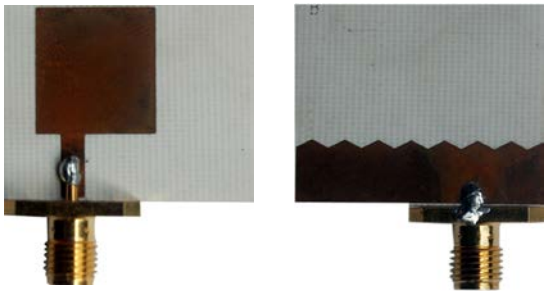

Top view Bottom view

Fig. 6. Photograph of the realized antenna.

Fig. 7. Antenna measurement setup in StarLab.

Using standard spherical wave expansion techniques, the antenna radiation can be fully defined by a set of modal coefficients. These modal coefficients are fed to software employing a ray propagation technique. Probe array technologies are now accepted as an efficient and accurate tool for antenna measurements.

Figure 8 shows the measured and simulated return losses. The simulated -10 dB return loss bandwidth ranges from 2.92 GHz to 15.70 GHz (137.3%). This wideband characteristic of the printed compact planar monopole antenna is confirmed in measurement, with only a small shift of the lower and upper edge frequency to 2.95 GHz and 15.45 GHz, respectively.

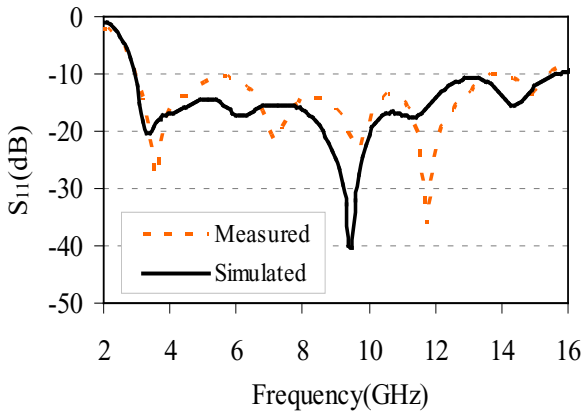


Fig. 8. Measured and simulated *S* parameters.

The disparity between the measured and simulated results is possibly attributed due to manufacturing tolerance and imperfect soldering effect of the SMA connector. It also may be due to the effect of the feeding cable, which is used in the measurements but not considered in simulation. The measured peak gain of the proposed realized antenna at boresight (+z direction) in the frequency range of 3 to 11 GHz is shown in Fig. 9. It is observed that the antenna has a good gain with a maximum value of 5.9 dBi at 9.4 GHz. The average gain is 3.92 dBi and the measured gain variations are less than ± 2 dBi. The measured radiation efficiency of the proposed antenna at boresight ($\theta$=$0^0$, $\varphi$=$0^0$) is shown in Fig. 10. The antenna has a maximum of 90.2% radiation efficiency. The gain and radiation efficiency of the proposed antenna are affected by the size of the partial ground plane.

Figure 11 shows the measured radiation patterns of the proposed antenna in two principal planes-namely, *xz*- and *yz*- planes for three resonant frequencies of 3.3, 6.2, and 9.4 GHz. It is observed that the radiation patterns of the proposed antenna present approximately omnidirectional and stable radiation characteristics in *xz*-plane over the operating band. Although some harmonic is introduced at higher frequencies, in *yz*-plane radiation patterns are about the same as that of a monopole antenna. The dips that observed mainly in $E_\varphi$ both in *xz*- and *yz*-plane could be due to the fact that the microstrip feed line is directly printed below the slotted partial ground plane (along *y*-axis).

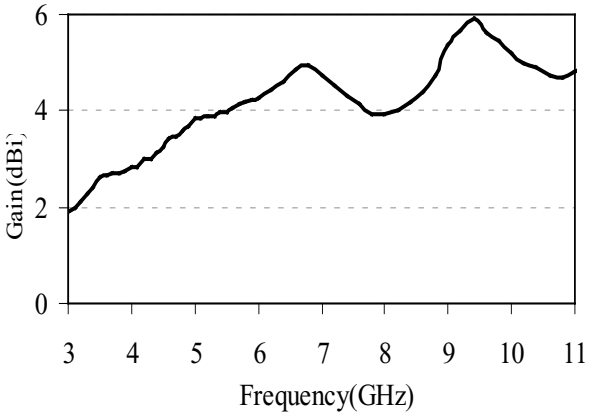


Fig. 9. Measured peak antenna gain.

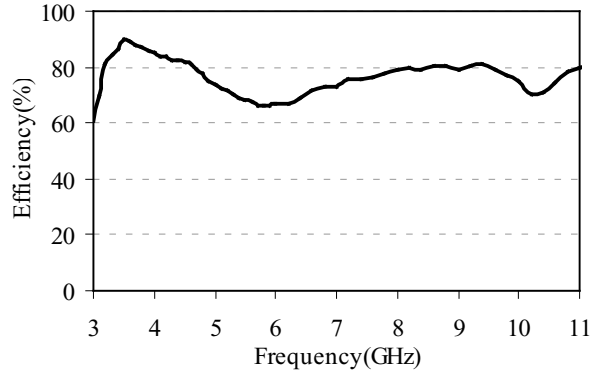


Fig. 10. Measured radiation efficiency.

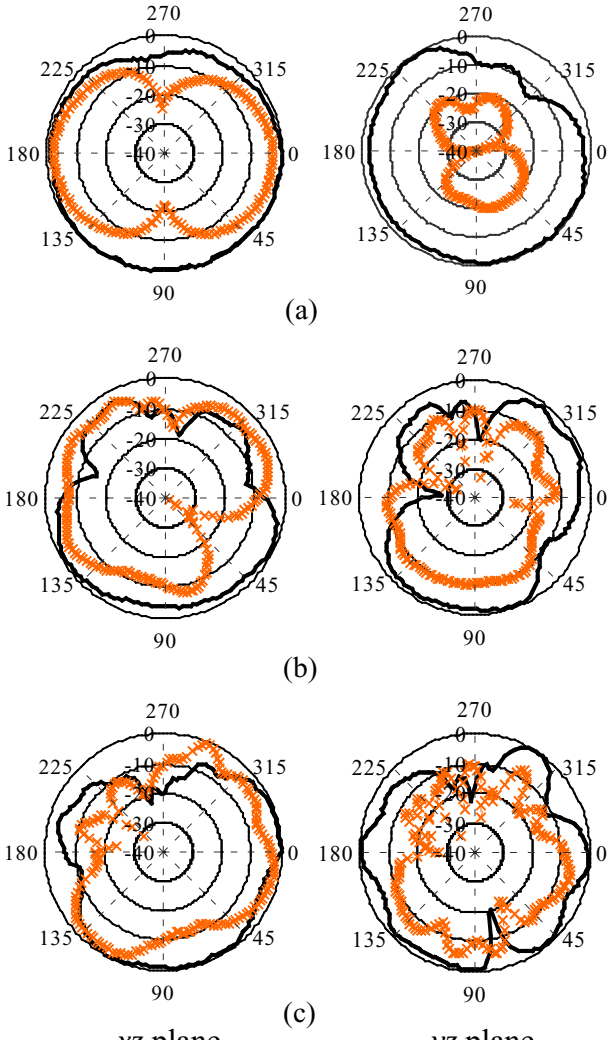


Fig. 11. Measured radiation patterns at (a) 3.3, (b) 6.2, and (c) 9.4 GHz [— $E_\theta$, ···x·x·x $E_\varphi$].

## IV. CONCLUSION

A compact planar antenna and a technique to enhance the impedance bandwidth have been proposed and implemented. The proposed planar antenna having a total size of 30 × 22 $mm^2$ is printed on an inexpensive FR4 substrate. The technique, cutting triangular shape slots on the top edge of the ground plane helps to increase the bandwidth by 43.6 %( 3.89 GHz). Measurement shows that, the proposed antenna with the modified sawtooth shaped ground plane has the -10 dB return loss bandwidth ranges from 2.95 GHz to 15.45 GHz (12.5 GHz) which covers the entire UWB band. The stable radiation patterns with a maximum gain of 5.9 dBi makes the proposed antenna suitable for being used in UWB communication.

## ACKNOWLEDGMENT

The authors would like to thank the Ministry of Higher Education Malaysia for sponsoring this work partially under Commonwealth Scholarship and Fellowship Plan.

## REFERENCES

[1] C. A. Balanis, *Antenna Theory Analysis and Design*, John Wiley & Sons, New York, 1997.

[2] M. K. Rahim and P. Gardner, "The Design of Nine Element Quasi Microstrip Log Periodic Antenna," *RF and Microwave conference,* Malaysia, pp. 132 – 135, October 2004.

[3] H. Rmili and J. M. Floc'h, "Design and Analysis of Wideband Double-Sided Printed Spiral Dipole Antenna with Capacitive Coupling," *Microwave and Optical Technology Letters,* vol. 50, no. 5, pp. 1312-1317, May 2008.

[4] A. K. Shackelford, K. F. Lee, and K. M. Luk, "Design of Small Size Wide-Bandwidth Microstrip Patch Antennas," *IEEE antennas and Propagation Magazine*, vol. 45, no. 1, pp. 75-83, February 2003.

[5] J. Y. Chiou, J. Y. Sze, and K. L. Wong, "A Broad-Band CPW Fed Strip Loaded Square Slot Antenna," *IEEE Transactions on Antennas and Propagation,* vol. 51, no. 4, pp. 719 – 721, April 2003.

[6] R. S. Kshetrimayum and R. Pillalamarri, "Novel UWB Printed Monopole Antenna with Triangular Tapered Feed Lines," *IEICE Electronics express*, vol. 5, no. 8, pp. 242- 247, April 2008.

[7] S. Tourette, N. Fortino, and G. Kossiavas, "Compact UWB Printed Antennas for Low Frequency Applications Matched to Different

Transmission Lines," *Microwave and Optical Technology Letters*, vol. 49, no. 6, pp. 1282-1287, June 2007.

[8] X. Zhang, W. Wu, Z. H. Yan, J. B. Jiang, and Y. Song, "Design of CPW-Fed Monopole UWB Antenna with a Novel Notched Ground," *Microwave and Optical Technology Letters,* vol. 51, no. 1, pp. 88-91, January 2009.

[9] M. N. Shakib, M. T. Islam, and N. Misran, "Stacked Patch Antenna with Folded Patch Feed for Ultra-Wideband Application," *IET Microw. Antennas Propag.* vol. 4, no. 10, pp. 1456–1461, October 2010.

[10] M. Ojaroudi, G. Kohnehshahri, and J. Noory, "Small Modified Monopole Antenna for UWB Application," *IET Microwave Antennas and Propagation,* vol. 3, no. 5, pp. 863-869, August 2009.

[11] Q. Wu, R. Jin, J. Geng, and M. Ding, "Printed Omni-Directional UWB Monopole Antenna with Very Compact Size," *IEEE Transactions on Antennas and Propagation,* vol. 56, no. 3, pp. 896–899, March 2008.

[12] J. Jung, W. Choi, and J. Choi, "A Small Wideband Microstrip-Fed Monopole Antenna," *IEEE Microwave and Wireless Components Letters,* vol. 15, no. 10, pp. 703–705, October 2005.

[13] C. Y. Hong, C. W. Ling, I. Y. Tarn, and S. J. Chung, "Design of a Planar Ultrawideband Antenna with a New Band-Notch Structure," *IEEE Transactions on Antennas and Propagation,* vol. 55, no. 12, pp. 3391–3396, December 2007.

[14] R. Azim, M. T. Islam, and N. Misran, "Printed Planar Antenna for Wideband Applications," *Journal of Infrared Millimeter and Terahertz Waves*, vol. 31, no. 8, pp. 969-978, August 2010.

[15] Y. J. Cho, K. H. Kim, D. H. Choi, S. S. Lee, and S.-O. Park, "A Miniature UWB Planar Monopole Antenna with 5-GHz Band-Rejection Filter and the Time-Domain Characteristics," *IEEE Transactions on Antennas and Propagation*, vol. 54, no. 5, pp. 1453–1460, May 2006.

[16] R. Zaker, C. Ghobadi, and J. Nourinia, "Novel Modified UWB Planar Monopole Antenna with Variable Frequency Band-Notch Function," *IEEE Antennas and Wireless Propagation Letters*, vol. 7, pp. 112–114, 2008.

[17] L. Liu, S. W. Cheung, R. Azim, and M. T. Islam, "A Compact Circular-Ring Antenna for Ultra-Wideband Applications," *Microwave and Optical Technology Letters*, vol. 53, no. 10, pp. 2283-2288, October 2011.

[18] K. P. Ray and Y. Ranga, "Ultrawideband Printed Elliptical Monopole Antennas," *IEEE Transactions on Antennas and Propagation, vol. 55,* no. 4, pp. 1189-1192, April 2007.

[19] J. Choi, K. Chung, and Y. Roh, "Parametric Analysis of a Band-Rejected Antenna for UWB Applications," *Microwave and Optical Technology Letters,* vol. 47, no. 3, pp. 287-290, November 2005.

[20] J. Wang, X. Sun, and K. Okada, "UWB Circular Monopole Omni-Directional Antenna with a Slot for Radiation Pattern Improvement," *IEEE conference on Ultra-Wideband*, Singapore, pp. 478–482, September 2007.

[21] R. Azim, M. T. Islam, and N. Misran, "A Planar Monopole Antenna for UWB Applications," *International Review of Electrical Engineering*, vol. 5, no. 4, pp. 1848-1852, 2010.

[22] J. Liu, K. P. Esselle, and S. Zhong, "An Extremely Wideband Rectangular Monopole Antenna with a Modified Microstrip Feed," *Fourth European Conference on Antennas and Propagation (EuCAP),* Spain, pp. 1-5, April 2010.

[23] R. Azim, M. T. Islam, N. Misran, S. W. Cheung, and Y. Yamada, "Study of Planar UWB Antenna with Multi-slotted Ground Plane," *Microwave and Optical Technology Letters*, vol. 53, no. 5, pp. 966-968, May 2011.

[24] L. J. Foged and A. Giacomini, "Wide Band Dual Polarized Probes for Near and Far Field Measurement Systems," *IEEE Antennas and Propagation Society Int. Symp.* CA, pp. 5-11, July 2008.

# A Novel UWB Out-of-Phase Four-Way Power Divider

**Bing Xiao, Jing-Song Hong, and Bing-Zhong Wang**

The Institute of Applied Physics
University of Electronic Science and Technology of China, Chengdu, 610054
bxuestc@gmail.com

***Abstract*** ─ A novel ultra-wideband (UWB) out-of-phase four-way power divider is presented. To achieve a division over a large frequency range, T-junctions formed by slotlines and microstrip lines are utilized. Based on the transmission-line equivalent-circuit method, we derive the design equations of the proposed power divider. Furthermore, all measured results are in good agreement with the predicted design equations and simulations. In addition, based on the power divider, a completely novel feed network is proposed to improve the narrow band property of microstrip antenna array.

***Index Terms*** ─ Four-way, microstrip, power divider, slotline, ultra-wideband (UWB).

## I. INTRODUCTION

An ultra-wideband (UWB) radar system has the merits of high range resolution, powerful penetration, low probability of intercept and robust jamming immunity, for they transmit signals across a much wider frequency than conventional radar systems. The most common technique for generating a UWB signal is to transmit pulses with very short durations (less than 1 nanosecond). These very short pulses need a wider transmitter bandwidth as conventional radar systems. Thus, a wideband feed network is essential in a wideband antenna system.

Power dividers are fundamental components used in antenna array feed networks. However, for a microstrip antenna array, bandwidth is a key limiting factor. That's probably because of quantities of quarter wavelength transformations in the feed network and the mutual coupling of antenna elements. Thus, an efficient wide band power divider serves significant contribution to wideband antenna arrays [1].

In [2], a 10-section 10-chip Wilkinson power splitter was proposed with very good return loss, isolation and insertion loss when avoiding different phase velocities in even and odd mode.

In [3], the authors have shown a compact two-way UWB power divider formed by a slotline and two microstrip lines accompanied by a wideband microstrip-slotline transition. It is a three-port network with one input port and two output ports with 180° phase difference.

Based on the above design, in this letter, the configuration of a UWB uniplanar four-way power divider is presented accompanied by simple design rules. Opposite to traditional wideband Wilkinson dividers and multilayer dividers [4], by utilizing the wideband property of microstrip-slotline mutual coupling, this design does not use neither resistive elements nor multilayer substrate. Thus, it is preferred when constructing a feed network of a wideband microstrip antenna array.

In the presented design, the input port exhibits a return loss better than -10 dB across UWB range as demonstrated via simulations and measurements. Because of the inherent properties of a lossless five-port circuit [5], which are governed by unitary properties of its scattering matrix, it cannot offer a perfect match at all its five ports as its counterpart with resistors. Furthermore, isolation between its output ports is compromised by the quality of match of its input and output ports. The better the match at the input and output ports, the worse is the isolation between the output ports.

*Submitted On: August 22, 2011*
*Accepted On: October 16, 2011*

## II. ANALYSIS AND DESIGN

The configuration of the proposed power divider is shown in Fig. 1. The divider utilizes a T-junction formed by a microstrip line and two arms of slotline, and other two T-junctions formed by a slotline and two arms of microstrip line. All ports of the divider are in the form of microstrip line and at the top layer of the printed circuit board, whereas the ground plane is at the bottom layer. There is a narrow rectangle slot in the ground crossing with microstrip lines. Each end of the slot is ended with a radial stub. The slot is responsible for guiding the wave from the input port to four output ports. The signals are coupled and divided from the microstrip line to two opposite directions in the slotline, and then signals of each side couple from the slotline to two arms of the microstrip line which are in equal magnitude but of 180 ° difference in phase.

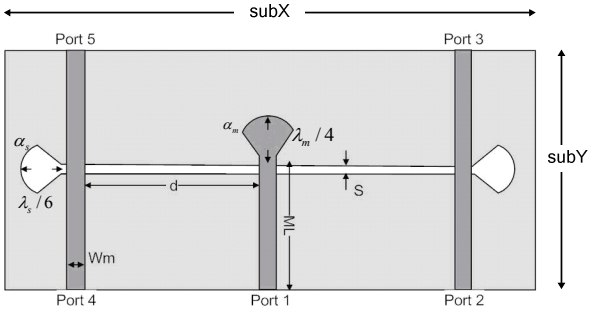


Fig. 1. Configuration of the proposed power divider.

The characteristic impedance of all the input and output ports $Z_{m0}$ is designed as 50 Ω. The slotline length is $2d$, but $d$ is an unconstrained parameter, here it is chosen as 0.88 $\lambda_s$ ($\lambda_s$ is the guided wavelength in slotline at the center frequency of 6.8 GHz). Due to the limitation of fabrication precision, we choose a 0.4 mm slotline which has a characteristic impedance of 112 Ω.

In order to efficiently (without reflections) couple the signals from the microstrip line to slotline, the end of the microstrip line is a radial line stub. It is utilized instead of a circular disk in [3] mainly because the radial line stub has an additional variety of flare angle $\alpha_m$. The flare angle $\alpha_m$ is an important parameter for impedance and bandwidth tuning, whereas the radius of the radial open stub is set to be approximately a quarter guided wavelength of the microstrip line. The stub (input impedance $Z_{ms}$) exhibits a virtual short-circuit and inductance [6].

In order to efficiently couple a signal from the slotline to two microstrip lines, the end of the slotline is a radial stub. For the same reason, the flare angle $\alpha_s$ of the radial stub can be tuned for better result of impedance and bandwidth. The radius of the radial open stub is set as $\lambda_s/6$ for quarter-wavelength transformation to broaden the bandwidth [7]. The stub (input impedance $Z_{ss}$) exhibits a virtual open-circuit and capacitance.

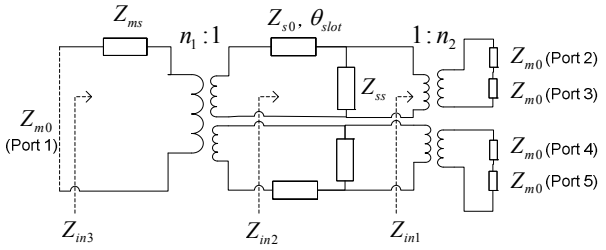


Fig. 2. The equivalent circuit of the proposed power divider.

The fundamental behavior can be explained by examining the corresponding equivalent circuits of the power divider shown in Fig. 2, $Z_{in1}$, $Z_{in2}$ and $Z_{in3}$ are input impedances at different locations. $Z_{s0}$ is the characteristic impedance of slotline, whereas $\theta_{slot}$ is the electrical length of slotline length $d$. The microstrip-slotline transition is modeled by an ideal transformer with turn ratio $n_1$ and $n_2$. The approximate value of $n$ has been calculated from [8] and $n$ depends on the properties of microstrip and slotline. For the input and output microstrip ports have the same characteristic impedance, it can be calculated that $n_1 = n_2 = n = 0.9449$.

In the equivalent circuit, the coupling from microstrip line to slotline is equivalent as parallel connection, whereas the coupling from slotline to microstrip line is equivalent as series connection [9]. Though corresponding formulas are available, for simplicity and accuracy, the input impedance of microstrip stub $Z_{ms}$ and input impedance of slotline stub $Z_{ss}$ are simulated by an electromagnetic simulator (HFSS V12).

Thus, the equations are established as follows. When $Z_{in3}=Z_{m0}$, a best transmission from input port to output ports is achieved.

$$Z_{in1} = \frac{2}{n^2} \cdot Z_{m0}, \tag{1}$$

$$Z_{in2} = Z_{s0} \cdot \frac{\frac{Z_{ss} \cdot Z_{in1}}{Z_{ss} + Z_{in1}} + jZ_{s0} \tan\theta_{slot}}{Z_{s0} + j\frac{Z_{ss} \cdot Z_{in1}}{Z_{ss} + Z_{in1}} \cdot \tan\theta_{slot}}, \tag{2}$$

$$Z_{in3} = \frac{n^2}{2} \cdot Z_{in2} + Z_{ms}. \tag{3}$$

Based on the above equations, the detailed dimensions of the proposed power divider are shown in Table 1.

Table 1. Detailed dimensions of the proposed power divider

| Substrate: RO4003C $\varepsilon_r$=3.38 tanδ=0.002 h=0.8mm | | | | |
|---|---|---|---|---|
| *subX* | *subY* | $\lambda_s/6$ | $\lambda_m/4$ | $W_m$ |
| 90mm | 30mm | 7mm | 8.3mm | 1.8mm |
| $\alpha_s$ | $\alpha_m$ | *d* | *ML* | *S* |
| 124deg | 134deg | 30mm | 15mm | 0.4mm |

## III. RESULTS AND DISCUSSION

The validity of the presented design method was tested by a prototype, as is shown in Fig. 3. It has an overall dimension of 90 mm × 30 mm. The manufactured power divider was tested via simulations and measurements. The simulations were performed using HFSS V12, whereas the measurements were done using a vector network analyzer. The simulated and measured performances of the power divider are shown in Figs. 4-8. The measured return loss for the input port of the device is better than 10dB except for the high frequency band, because firstly the soldered SMA connectors lead to additional loss, secondly, the fabrication variation also results in some discrepancy between the simulated and measured results. The developed device exhibits an average insertion loss at the four output ports equal to 2dB across the 3.1-10.6 GHz band. Isolations between the output ports are more than 5dB (direct connected port 2, 3 and port 4, 5) and 11dB (indirect connected others ports).

Concerning the phase performance of the developed device, as is analyzed, the measured results indicate that the output signals from two direct connected ports have an 180° phase shift across the 3.1-10.6 GHz band.

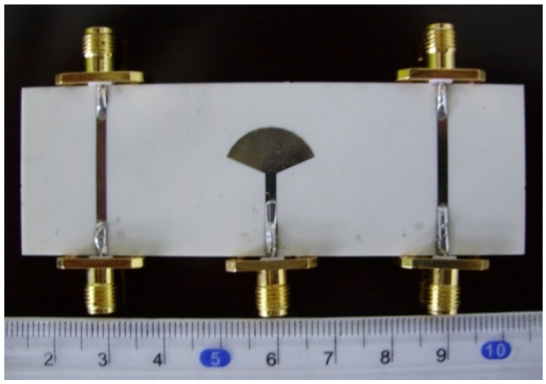

(a)

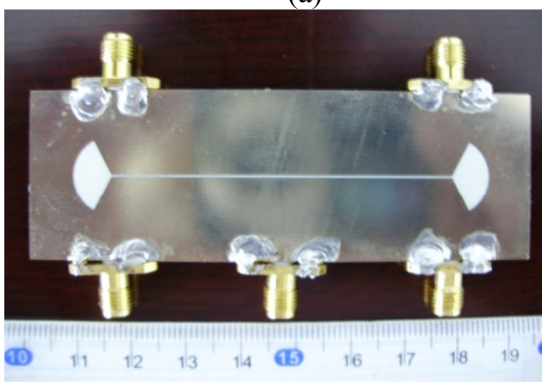

(b)

Fig. 3. Photograph of the proposed power divider: the top view (a) and the bottom view (b).

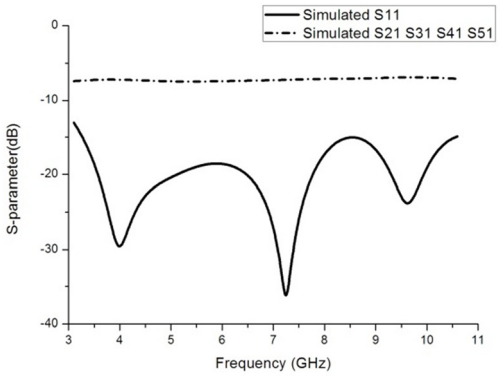


Fig. 4. Simulated return loss and insertion loss of the power divider.

We wish the presented analysis serves as an useful purpose for the band expansion of feed network of antenna array. In Fig. 9, we propose a completely novel in phase wideband feed network for 4 × 4 antenna array. It is composed of five power dividers as mentioned above. Every output port of the central power divider is linked by the input port of a new power divider. Considering the

180° phase difference of the output ports, ultra λm /2 length of microstrip is added to keep the output ports in phase. As every single power divider has the UWB property and simple structure, we believe the proposed feed network will have a good wideband property.

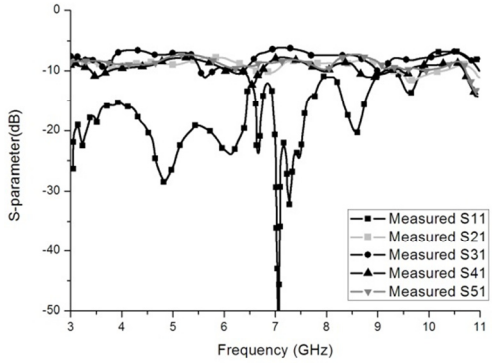


Fig. 5. Measured return loss and insertion loss of the power divider.

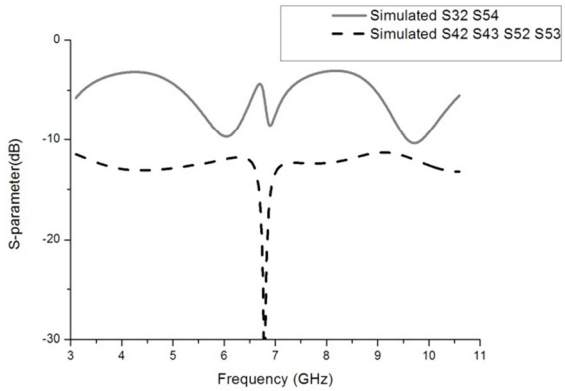


Fig. 6. Simulated isolation of the power divider.

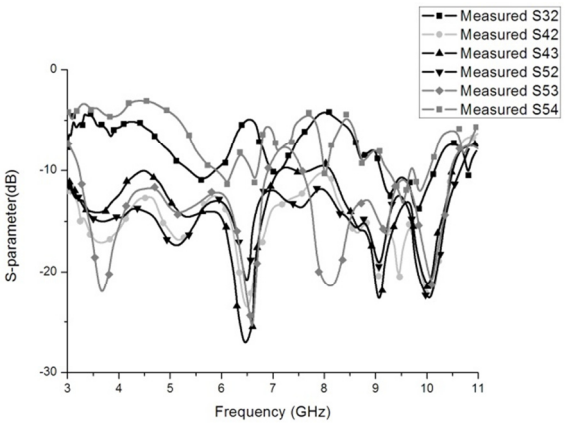


Fig. 7. Measured isolation of the power divider.

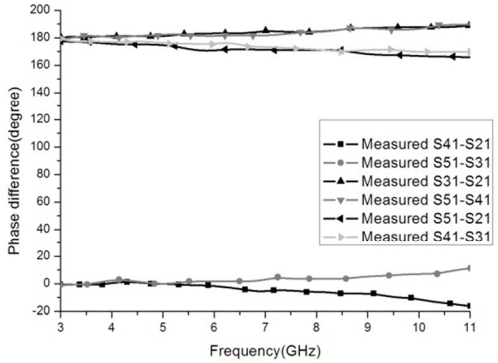


Fig. 8. Measured phase difference between the output ports.

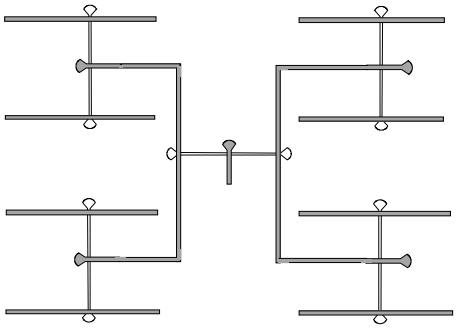

Fig. 9. A novel in-phase wideband feed network.

## IV. CONCLUSION

A novel out-of-phase four-way power divider with UWB performance has been presented. The proposed device utilizes microstrip-slotline coupled structures. The simulated and measured results of the manufactured device have shown an UWB performance concerning the return loss, insertion loss and isolation. The design equations of the proposed UWB power divider have also been derived based on the transmission-line equivalent-circuit method. In addition, based on the power divider, a completely novel feed network is proposed to improve the narrow band property of microstrip antenna array.

## ACKNOWLEDGMENT

This work was supported by the National Natural Science Foundation of China (No. 61172115 and No. 60872029), the High-Tech Research and Development Program of China (No. 2008AA01Z206), the Aeronautics Foundation of China (No. 20100180003), and the Fundamental Research Funds for the Central Universities (No. ZYGX2009J037).

## REFERENCES


[1] V. Demir, D. Elsherbeni, D. Kajfez, and A. Z. Elsherbeni, "Efficient Wideband Power Divider for Planar Antenna Arrays," *Applied Computational Electromagnetic Society (ACES) Journal*, vol. 21, no. 3, pp. 318 – 324, November 2006.

[2] S. Ibrahimpasic and M. Hasanovic, "Modeling and Simulation of Wilkinson Power Splitter in Suspended Stripline," *Applied Computational Electromagnetic Society (ACES) Journal*, vol. 25, no. 10, pp. 888– 893, October 2010.

[3] M. E. Bialkowski and A. M. Abbosh, "Design of a Compact UWB Out-of-Phase Power Divider," *Microwave and Wireless Components Letters, IEEE*, vol. 17, pp. 289-291, 2007.

[4] K. Song and Q. Xue, "Novel Ultra-Wideband (UWB) Multilayer Slotline Power Divider with Bandpass Response," *Microwave and Wireless Components Letters, IEEE*, vol. 20, pp. 13-15, 2010.

[5] D. M. Pozar, *Microwave engineering*, Wiley-India, 2009.

[6] F. Giannini, R. Sorrentino, and J. Vrba, "Planar Circuit Analysis of Microstrip Radial Stub (Short Paper)," *Microwave Theory and Techniques, IEEE Transactions on*, vol. 32, pp. 1652-1655, 1984.

[7] B. Schuppert, "Analysis and Design of Microwave Balanced Mixers," *Microwave Theory and Techniques, IEEE Transactions on*, vol. 34, pp. 120-128, 1986.

[8] K. C. Gupta, R. Garg, I. J. Bahl, and P. Bhartia, "Microstrip Lines and Slotlines (Formulas 6.3-6.7)," 1979.

[9] P. Soltysiak and J. Chramiec, "Design of Broadband Transitions from Microstrip to Slotline," *Electronics Letters*, vol. 30, pp. 328-329, 1994.


**Bing Xiao** is a graduate student major in Radio Physics in the University of Electronic Science and Technology of China now. His research interests include antenna technology and wireless communication technique.

**Jing-song Hong** received the B.Sc. degree in Electromagnetics from Lanzhou University, China, in 1991, and the M.Sc. and Ph. D. degrees in Electrical Engineering from the University of Electronic Science and Technology of China (UESTC), in 2000 and 2005, respectively. He is now a professor with UESTC. From 1991 to 1993, he was a Circuit Designer with the Jingjiang Radar Factory, Chengdu, China. From 1993 to 1997, he was a Testing Engineer with SAE Magnetics (HK) Ltd, Guangdong, China. From 1999 to 2002, he was a Research Assistant with the City University of Hong Kong. His research interest includes the use of numerical techniques in electromagnetics and the use of microwave methods for materials characterization and processing.

**Bing-zhong Wang** received the B.S.E.E., M.S.E.E., and Ph.D. degrees from the University of Electronic Science and Technology of China (UESTC), Chengdu, in 1982, 1984, and 1988, respectively, all in Electrical Engineering. He joined the Institute of Applied Physics, UESTC, in 1984. From 1984 to 1988, he was a Research Assistant, and his research dealt with the millimeter-wave transmission lines and millimeter-wave integrated circuits. From 1988 to 1990, he served as a Lecturer/Research Associate in the Institute of Applied Physics at UESTC, conducting researches in electromagnetic scattering. From August 1990 to January 1992, he was with the Department of Electrical Engineering, University of Wisconsin-Milwaukee, where he was a Visiting Scientist in the Signal Propagation Research Laboratory and engaged in research on the theoretical modeling of the electromagnetic behavior of high-speed integrated circuits. He returned to UESTC in 1992 as an Associate Professor and was promoted as a Full Professor in June 1995. From August 1996 to August 1997, he was a Visiting Research Fellow in the Department of Electronic Engineering at the City University of Hong Kong. From January 2000 to March 2000, he was a Visiting Professor in the Electromagnetic Communication Research Laboratory, Pennsylvania State University, and University Park. His current research interests are in the areas of computational electromagnetics, numerical modeling and simulation of the electromagnetic behavior in high speed integrated circuits and electronic packages, EMC analysis, electromagnetic modeling by artificial neural networks, computer aided design for passive microwave and millimeter wave integrated circuits, and antenna design.

# Fundamental and Magnetic Force Analysis of an External Rotor Switched Reluctance Motor

**H. Torkaman, N. Arbab, H. Karim, and E. Afjei**

Department of Electrical and Computer Engineering, Shahid Beheshti University, G.C. Tehran, Iran
Emails: H_Torkaman@sbu.ac.ir, Arbab.nasim@gmail.com, H-Karim@ieee.org, E_Afjei@sbu.ac.ir

***Abstract*** ─ This paper presents a novel three-phase 6/8 external rotor switched reluctance motor. Such a construction not only leads to reduce the total weight and volume, but also increases the total efficiency in a small size motor. Three dimensional finite element method is applied to evaluate the main characteristics of the proposed motor such as magnetic flux density, flux linkage, self-inductance, mutual inductance, and output torque. Moreover, this paper investigates the radial force components of the motor. This assessment is carried out under different forced current levels with the respect to critical rotor positions. From the motor analysis results, it is considered that the proposed motor has great advantages over the conventional type in its magnetic profiles.

***Index Terms*** ─ External rotor configuration, radial force, switched reluctance motor, three dimensional finite element method.

## I. INTRODUCTION

The salient features of a switched reluctance motor (SRM) such as the lack of a coil or a permanent magnet on the rotor, a simple structure and high reliability, makes it a suitable candidate for operation in harsh or sensitive applications [1, 2]. However, due to the operation in the magnetic saturation region, the high performance torque control of this type of motor is a critical issue for smooth running. A comprehensive magneto static modeling and analysis in different conditions can improve the operating performance for the entire motor control system [3-6].

In general, there are four distinct types of SRMs: namely, regular doubly salient cylindrical [7], disc-type [8], multi-layer, and linear motors [9]. This classification stems from the general shape of the motor. The regular cylindrical type of SR motor has salient poles on both stator and rotor, and the windings are wrapped around the stator poles. Direct current motors with disc rotors are widely used and have been proposed for SR motors as well. The need for disc type arises in applications where the spacing is of the primary concern. The multilayer SR motor consists of three magnetically independent layers or phases. Each layer comprises of a stationary part and a rotating piece known as stator and rotor, respectively.

Regarding the conventional design, the air gap radius is limited by the space needed for the coils inside the stator furthermore by the cooling inside the housing surrounding the laminations. The external rotor design has the benefit that coils and cooling can be placed near the shaft, increasing the possible air gap radius [10]. As a result, the external rotor switched reluctance motors (ERSRM) own the comparative advantage of having higher output torque at low speed and also elevated motor efficiency. Additionally, ERSRMs are suitable in-wheel motors for electric vehicles (EVs) because they provide great flexibility in motion control [11].

Basis of ERSRMs is on tendency of the polarized rotor pole in achieving full alignment position with the excited stator pole which provokes a whirling mode of the motor [8, 12]. Tangential and radial forces are two components of this magnetism force. The tangential force transforms into the rotational torque. Generally, in balanced motor operation, the total of radial force is zero at ideal mode. However, faulty operation caused by structural or environmental motivations gives rise to unbalance radial forces which are undesired and they result in motor vibrations. For instance, unbalanced external load or off-centered rotor leads to form asymmetrical air gap and then acoustic noise of the motor, due to produced radial force [13].

*Submitted On: February 16, 2011*
*Accepted On: October 20, 2011*

Authors in the previous works have proposed several SRM structures such as; a new multilayer SRM [14], a novel field assisted SRM/G [15], and also in [16] a novel switched reluctance generator (SRG) is compared with a BLDC. Furthermore, the magnetic characteristics of the various SRMs are evaluated in [17-23] under normal and faulty conditions. Therefore, in this paper, the magnetic profiles of the new SRM with external rotor are obtained and analyzed. In this regard, due to nonlinear and complex magnetic treatments of SRMs, three dimensional finite element method (3D-FEM) is utilized for precise analysis and evaluation of the magnetic characteristics.

## II. THE ERSRM STRUCTURE

As stated before, the purpose of this paper is to evaluate a small size switched reluctance motor with an external rotor. A proper design method for the SRM is imperative to overcome its disadvantages. The suitable method will definitely improve the potentials of SRM in various adjustable speed drive applications. Like other motors, the SRM has specific characteristics that make it appropriate for certain applications and inappropriate for others. The degree of appropriateness of a SRM for any application depends on the objectives and application's requirements.

The analytical design equation and some specific ratios for this study, are adapted from [24] and the IEC71 standard. These design equations are used to evaluate different SRM traits considering magnetic saturation. The approximations and some simplifications are adopted during the development of analytical design equations are vindicated with FEM analysis. It is worth to be pointed out that the maximum torque density, minimum flux leakage, and efficiency are among the various design objectives in this study.

In this motor, the stator and rotor cores are made by non-oriented steel lamination to reduce the eddy current effects and skin effects as well as hysteresis losses. The laminations of the stator and rotor and their dimensions are shown in Fig. 1 and Table I, respectively.

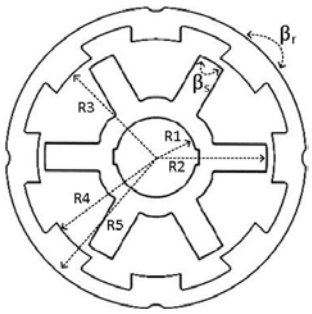


Fig. 1. The lamination and dimensions of proposed ERSRM.

Table 1. The dimensions of proposed ERSRM

| Parameters | value |
|---|---|
| Number of phases | 3 |
| R1 | 8 mm |
| R2 | 22.2 mm |
| R3 | 22.5 mm |
| R4 | 25.5 mm |
| R5 | 28.5 mm |
| βs | 14.5˚ |
| βr | 24˚ |
| Minimum air gap | 0.3 mm |

ERSRM consists of eight salient poles in rotor with no windings, while the stator has six salient poles which include windings wrapped around them. In this type of SRM, rotor is placed outside instead of the stator; both stator and rotor have salient poles such as conventional SRMs. Based on this structure, the motor named 6/8 ERSRM.

## III. FEM MODELING AND RESULTS

To evaluate the motor design and performance properly, a reliable model is required. The FEM can be conveniently used to obtain the magnetic vector potential values throughout the motor in the presence of complex magnetic circuit geometry and nonlinear properties of the magnetic materials. These vector potential values can be processed to obtain the field distribution, torque, and flux leakage. In this paper, the field analysis was performed using a Magnet CAD package [25]. This package is based on the variation energy minimization technique to solve for the magnetic vector potential. The technique utilized by the MagNet package is based on the variational energy minimization technique to solve for the electric vector potential. In this method, the electric vector potential is known as $T-\Omega$ formulation.

Magnetic flux density is derived for different rotor position through a variety of forced currents.

The amplitude of magnetic flux density for 2A forced current is shown in Fig. 2 at different critical positions (unaligned, half aligned, and fully aligned positions).

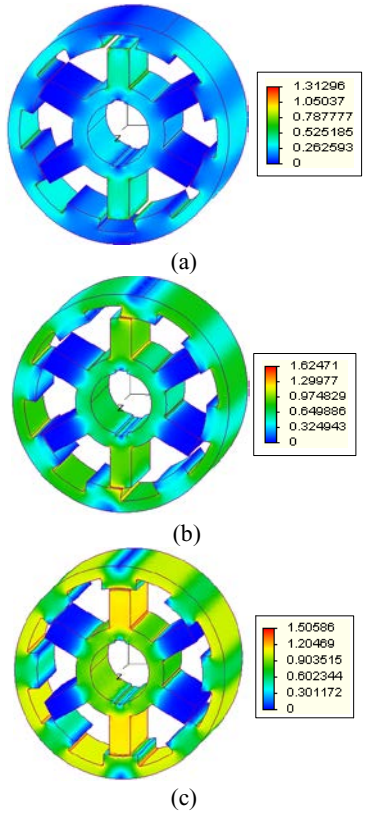


Fig. 2. Flux density distribution at: a) unaligned, b) half aligned, and c) fully aligned positions.

As seen from Fig. 2, when rotor moves from an unaligned position to a half aligned position, the maximum flux densities in stator/rotor poles are increased from 0.65 to 1.62 Tesla; it means the flux density in a half aligned position is 2.5 times higher than an unaligned position. It shows the power of the generation axial force between stator and rotor poles. This fact helps us to produce high torque value and improved motor speed.

In an SRM, inductance is a function of rotor position and stator current. At an aligned position or at higher current levels, the ferromagnetic material in the stator and rotor poles begins to saturate. As a result of the secondary effects such as saturation, fringing, and leakage, nonlinearities are introduced in the connection between inductance, rotor position, and current. At an unaligned position, phase inductance has a minimum value due to high reluctance offered by large air gap. Magnetic saturation is unlikely to occur at an unaligned position, and thus, the flux linkage shows a linear behavior until the start of overlap. Where rotor poles completely overlap with stator poles, at a fully aligned position, magnetic field density tends to saturate at high current levels. It makes flux linkage a nonlinear function of position and stator current. This behaviour is shown in Fig. 3.

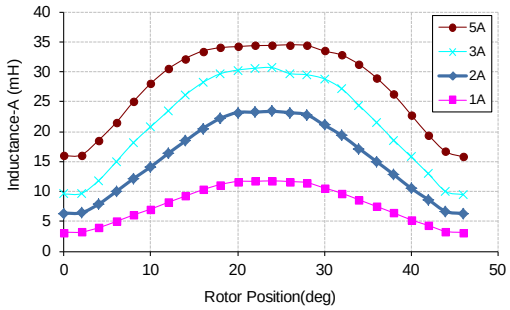


Fig. 3. Self-inductance of phase A vs. rotor position under various forced currents.

As shown in Fig. 3, with increasing forced current from 1 to 5 Amperes, the self-inductance in phase A goes up from 12 to 35mH (in maximum value). Furthermore, it illustrates the shape of inductance in the low currents is linear but in high current is nonlinear because of saturation phenomena. As seen from Fig. 3, by exciting at the position where the slope of inductance always increases, the ERSRM always produces high positive torque and can rotate continuously with minimum ripple.

Suppose two coils are placed near each other, the same as coils in the proposed motor. Since the two coils are close to each other, some of the magnetic field lines through the former coil will also pass through the other coil. As a result, there will be an induced electro motive force associated with the changing magnetic flux in the second coil. The fact that a change in the current of a coil affects the voltage and current in another coil is defined as mutual inductance. In a proposed motor, when phase A is excited and two other phases are off, mutual inductance appears in two other inactive phases (B,C) as shown in Figs. 4 and 5.

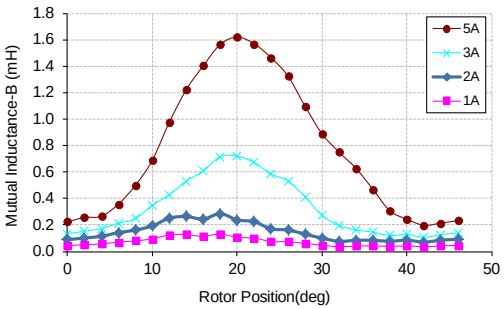


Fig. 4. Mutual inductance of phase B vs. rotor position under various forced currents.

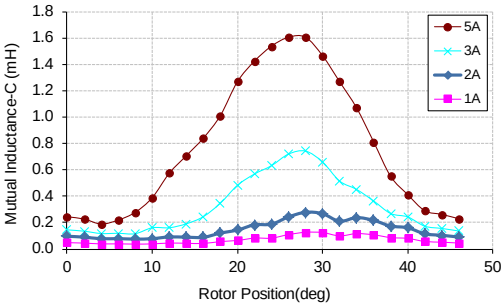


Fig. 5. Mutual inductance of phase C vs. rotor position under various forced currents.

As it is depicted from Figs. 4 and 5, the mutual inductances in coils B1, B2, C1, and C2 have very low amplitude, as the maximum mutual inductance is 1.6mH in 5A forced current. In addition, the mutual inductances in inactive phases are decreased when the current has descended. It is mentionable that this feature is very promising in this type of machine than conventional SRM to decrease the losses and improve the efficiency.

On the other side, the ratio of mutual inductance in inactive phases respect to self-inductance in active phase (A) is considerable in this machine. Figures 3 and 5 demonstrate with an increase in forced current, the produced mutual inductance in the phase B respect to self-inductance in phase A (in maximum value of $(L_{B1}/L_{A1})\times 100\%)$ increases from 0.7% to a maximum of 4.5% (for $i=0.1A$ to $i=5A$). Similarly, this manner is repeated in the phase C respect to phase A. This means the induced flux to inactive phases in idle mode have very low amplitude which it has originated from structure and dimension of the designed ERSRM. In motor designs, the inductance ratio (mutual inductance/ self-inductance) should be minimized, so the proposed ERSRM is usually guaranteed for a well-designed motor.

In a SRM, inductance and reluctance are functions of a phase current, which causes the establishment of flux and rotational motion. At an aligned position and higher current levels, magnetic iron begins to saturate. Due to saturation, fringing, and leakage, nonlinearities are introduced. At an unaligned position, phase inductance has minimum value as a result of high reluctance presented by large air gap. Since the stator and rotor poles overlap, pole corners display local saturation due to concentration of flux into the relatively small area of the pole corners and hence flux linkage curve begin to be nonlinear. When rotor poles completely overlap with stator poles, at fully aligned position, stator/rotor poles and stator yoke saturate at high current levels making flux linkage a nonlinear function of position and current.

Saturation effects tend to lower the aligned inductance, which in effect, decreases the rate of change of inductance. As torque is proportional to slope of inductance, saturation lowers the torque produced at given current on one hand; while on other hands it improves the ratio of mechanical energy to the energy supplied by a controller. For the numerical calculation of torque, this paper uses the flux profiles obtained from 3D-FEM simulations and measurements.

Based on the fundamentals of torque concept, Fig. 6 shows the static torque profiles for the ERSRM from 1 to 5 A.

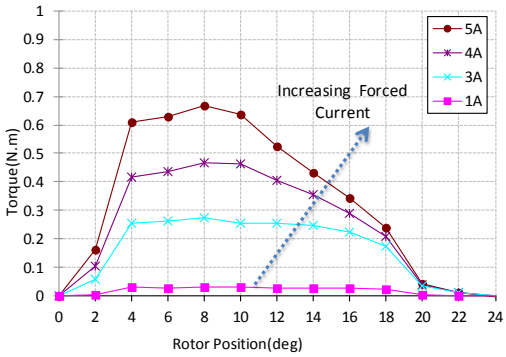


Fig. 6. Static torque vs. rotor position under various forced currents.

As expected from torque equations, rising current must result in a linear increase in torque, but as it is shown in Fig. 6, it does not. Because, the stator/pole cores are imported in the

nonlinearly region in high amplitude of current and motor is operating in the saturation zone.

It is shown, the torque per ampere ration in this motor is good for this volume. It is worthy to mention that the increment of torque per ampere ratio reduces the volt-ampere which is required for the motor control converter.

As seen from Fig. 6, higher torque curve has been obtained for the 5A current. This means, with increasing the forced current the torque will be increased, also its ripple will be greater than before. In solving this issue, the controller unit as well as switching angle must be modified. Also, considering the maximum torque per ampere for control strategy leads to smooth torque control of an ERSRM.

## IV. Magnetic Force Characteristic Analysis

The predicted radial and tangential force characteristics of the ERSRM are presented by this part. First of all, some descriptions of these forces calculation should be pointed out. The calculations of the radial forces are based on Maxwell stress tensor. The radial and tangential forces based on Maxwell stress tensor are given by (1), and (2), respectively.

$$f_n = \frac{1}{2\mu_0}(B_n^2 - B_t^2), \quad (1)$$

$$f_t = \frac{1}{2\mu_0} B_n B_t, \quad (2)$$

where $f_n$, $f_t$ are the produced radial and tangential forces, respectively. The $B_n$, $B_t$ and $\mu_0$ are the normal component, the tangential component of the flux densities, and the absolute permeability, respectively.

It can be concluded that the $B_n$ and $B_t$ should be equal in healthy motor and ideal condition, which results in zero value for their differences as well as radial force. This ideal condition does not appear in all machines, because of their asymmetric structure, assembly errors, and load fluctuations. Therefore, it is noticeable that the maintaining of radial force in minimum value is essential to avoid producing noise and vibration.

According to equation (2), it can be predicted that the maximum radial force occurs at the fully aligned position since the radial field component reaches its maximum value while the tangential field component is on its minimum value. In order to achieve the accurate results from this method, a circle contour was chosen in the middle of the air gap. It is worth noting that the resulted force is independent of the integration path. Maxwell's equations indicate that studying the components of the flux density is crucial in order to understand the force generation process.

For the first step of this analysis, the variations of radial field component versus contour position under different forced currents are calculated for ERSRM. These profiles are shown in Fig. 7, for unaligned, half aligned, and fully aligned rotor positions.

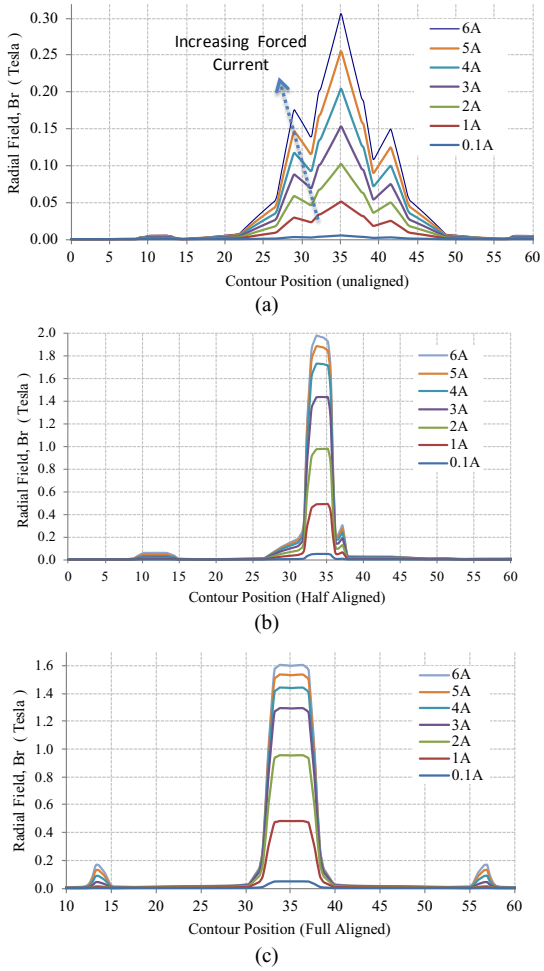


Fig. 7. Radial field component vs. contour position under different forced currents: a) unaligned, b) half, and c) fully aligned positions.

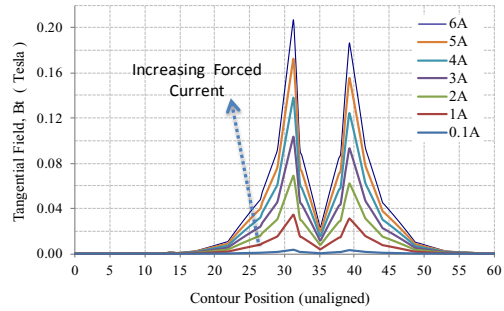


(a)

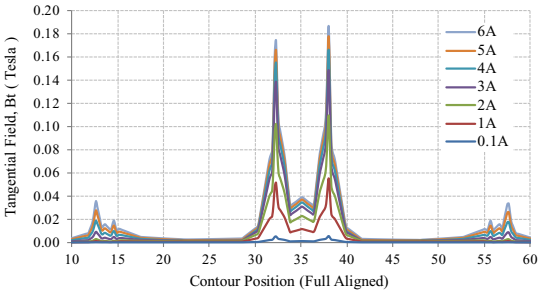


(b)

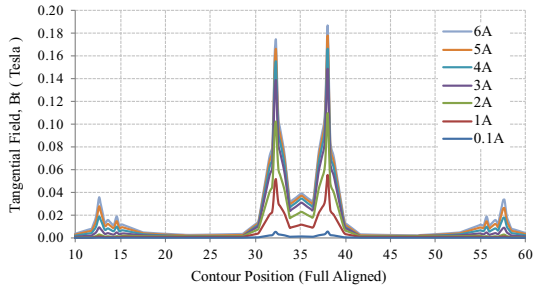


(c)

Fig. 8. Tangential field component vs. contour position under different forced currents: a) unaligned, b) half, and c) fully aligned positions.

The variations of tangential field component versus contour position under different forced currents are calculated for ERSRM. These profiles are shown in Fig. 8, for unaligned, half aligned, and fully aligned rotor positions.

As the results of Fig. 8 demonstrate, the maximum of $B_t$ occurs at respective corner tips of stator and rotor. Notably, effects of local saturation at these rotor and stator tips result in two local maxima in $B_t$. It is important to note that a largely normal force exists at this rotor position that is substantially stronger than a tangential component. As shown in Fig. 7, the amplitude of the radial field component increases nonlinearly. In fact, as the forced current enhances, the amplitude of $B_t$ and $B_n$ are increased more slowly due to the saturation effect. Radial field components ($B_n$) in an unaligned position rises with current, but the amplitude is very low namely 0.301 Tesla and is on its maximum value when the forced current is fixed at 6A.

As the rotor leaves the unaligned position toward the half aligned position, the overlap between rotor and stator poles begins. Hence, effects of local saturation are visible in the first and second peak of Fig. 8. As it is shown, the first peak decreases with the ratio of 0.76, and the second peak increases with the ratio of 1.6. As rotor leaves the half aligned position toward the fully aligned position, the maximum value of radial field component remains almost constant (in higher currents the amplitude decreases with the 0.8 ratio). Although the maximum value of radial field stays almost constant or decreases in higher currents, the width of the region within which the radial component exists increases. It means that the average radial force has its own maximum value at fully aligned position as it was expected.

Figure 9 shows the variations of total produced radial forces under 1, 4, 5, and 6 Amperes forced currents in ERSRM.

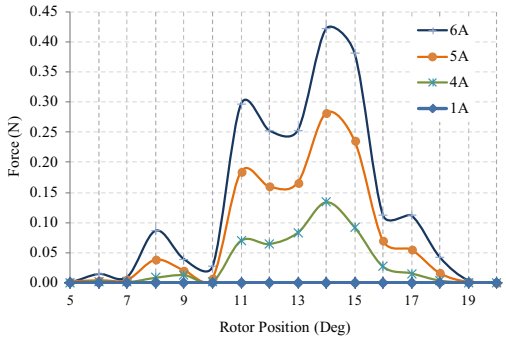


Fig. 9. Radial force vs. rotor position under different forced currents.

According to Fig. 9, it is realized that, the amplitude of the radial force is almost zero in the low level of forced current. Besides, when the level of the forced current is increased from 4 to 5 and 6A the maximum radial force has 2 and 3 times higher value than 4A current.

As it was mentioned in previous sections, the radial force produced due to the different factors may be very destructive and cause harsh effects on the control, rotor position, and performance of ERSRM. Therefore, some methods must be devised to control or compensate the produced forces. In this regard, several studies proposed the search coils which are placed on the stator poles to

produce an additional force on the opposite of radial force direction for compensating it. On the other side, kinds of accelerators are placed on the generator to investigate these forces and their amplitude and then control their values with control unite.

## V. CONCLUSION

In this paper, fundamental profiles and the distributions of radial and tangential forces inside the air gap of new external rotor SRM were obtained and analyzed. The results obtained have demonstrated the induced flux to inactive phases in idle mode have very low amplitude, which the produced mutual inductance in the idle phase respect to self-inductance in active phase is 0.7%-4.5% in maximum values. According to the results, it was realized that, the amplitude of radial force was almost zero in low level of forced current. Besides, when the level of forced current was increased from 4 to 5 and 6A, the maximum radial force has 2 and 3 times higher value than 4A current. It can be concluded that the proposed ERSRM is appropriate for various applications in small sizes.

## ACKNOWLEDGMENT

This work was supported by a grant (600/1444) from the vice-presidency of research and technology of Shahid Beheshti University.

### REFERENCES

[1] H. J. Chen, D. Q. Jiang, and J. Yang et al., "A New Analytical Model for Switched Reluctance Motors," IEEE Transactions on Magnetics, vol. 45, no. 8, pp. 3107-3113, August, 2009.

[2] M. Nguyen, Y. Jung, and H. Yang et al., "Harmonic Intensity Reduction Technique for Single Phase Switched Reluctance Motor Drives Using a New Random PWM Scheme," Journal of Power Electronics, vol. 10, no. 1, pp. 51-57, 2010.

[3] G. J. Li, J. Ojeda, and E. Hoang et al., "Comparative Studies Between Classical and Mutually Coupled Switched Reluctance Motors Using Thermal-Electromagnetic Analysis for Driving Cycles," IEEE Transactions on Magnetics, vol. 47, no. 4, pp. 839 - 847, 2011.

[4] W. Ding, D. Liang, and H. Sui, "Dynamic Modeling and Performance Prediction for Dual-Channel Switched Reluctance Machine Considering Mutual Coupling," IEEE Transactions on Magnetics, vol. 46, no. 9, pp. 3652 – 3663, 2010.

[5] J. Cai, Z. Q. Deng, and R. Y. Qi et al., "A Novel BVC-RBF Neural Network Based System Simulation Model for Switched Reluctance Motor," IEEE Transactions on Magnetics, vol. 47, no. 4, pp. 830 - 838, 2011.

[6] J. Du, D. Liang, and L. Xu et al., "Modeling of a Linear Switched Reluctance Machine and Drive for Wave Energy Conversion Using Matrix and Tensor Approach," IEEE Transactions on Magnetics, vol. 46, no. 6, pp. 1334 - 1337, 2010.

[7] W. Ding and D. Liang, "Modeling of a 6/4 Switched Reluctance Motor Using Adaptive Neural Fuzzy Inference System," IEEE Transactions on Magnetics, vol. 44, no. 7, pp. 1796-1804, 2008.

[8] F. Daldaban and N. Ustkoyuncu, "New Disc Type Switched Reluctance Motor for High Torque Density," Energy Conversion and Management, vol. 48, no. 8, pp. 2424-2431, 2007.

[9] J. H. Park, S. M. Jang, and J. Y. Choi et al., "Dynamic and Experimental Performance of Linear-Switched Reluctance Machine With Inductance Variation According to Airgap Length," IEEE Transactions on Magnetics, vol. 46, no. 6, pp. 2334 – 2337, 2010.

[10] M. D. Hennen and R. W. De Doncker, "Comparison of Outer- and Inner-Rotor Switched Reluctance Machines," in 7th International Conference on Power Electronics and Drive Systems, Thailand, pp. 702-706, 2007.

[11] L. Jiongkang and et al., "Experimental Investigation of In-Wheel Switched Reluctance Motor Driving System for Future Electric Vehicles," in 3rd International Conference on Power Electronics Systems and Applications, PESA, Hong Kong, pp. 1-6, 2009.

[12] D. Wen and L. Deliang, "Modeling of a 6/4 Switched Reluctance Motor Using Adaptive Neural Fuzzy Inference System," IEEE Transactions on Magnetics, vol. 44, no. 7, pp. 1796-1804, 2008.

[13] L. Feng-Chieh and Y. Sheng-Ming, "Instantaneous Shaft Radial Force Control with Sinusoidal Excitations for Switched Reluctance Motors," IEEE Transactions on Energy Conversion, vol. 22, no. 3, pp. 629-636, 2007.

[14] E. Afjei, H. Torkaman, and B. Mazloomnezhad, "A New Double Layer per Phase Configuration for Switched Reluctance Motor," in IEEE International Conference on Power and Energy (PECON), Kuala Lumpur, Malaysia, pp. 222-225, 2010.

[15] E. Afjei and H. Torkaman, "The Novel Two Phase Field-Assisted Hybrid SRG: Magnetio Static Field Analysis, Simulation, and Experimental Confirmation," Progress in Electromagnetics Research B, PIER, vol. 18, pp. 25-42, 2009.

[16] E. Afjei, and H. Torkaman, "Comparison of Two Types of Dual Layer Generator in Field Assisted Mode Utilizing 3D-FEM and Experimental Verification," Progress in Electromagnetics Research B, PIER, vol. 23, pp. 293-309, 2010.

[17] E. Afjei and H. Torkaman, "Finite Element Analysis of SRG under Fault Condition Oriented Towards Diagnosis of Eccentricity Fault," Applied Computational Electromagnetics Society, vol. 26, no. 1, pp. 8-16, 2011.

[18] H. Torkaman, M. S. Toulabi, and E. Afjei, "Electromagnetic Analysis of the Effects of Static Eccentricity Fault on the Radial Force Variations in Switched Reluctance Motors," International Review on Modelling and Simulations, vol. 4, no. 2, pp. 585-590, 2011.

[19] H. Torkaman, E. Afjei, and R. Ravaud et al., "Misalignment Fault Analysis and Diagnosis in Switched Reluctance Motor," International Journal of Applied Electromagnetics and Mechanics, vol. 36, no. 3, pp. 253-265, 2011.

[20] H. Torkaman and E. Afjei, "Magnetostatic Field Analysis and Diagnosis of Mixed Eccentricity Fault in Switched Reluctance Motor," Electromagnetics, Taylor and Francis, vol. 31, no. 5, pp. 368-383, 2011.

[21] H. Torkaman and E. Afjei, "Determining Degrees of Freedom for Eccentricity Fault in SRM Based on Nonlinear Static Torque Function," COMPEL:The International Journal for Computation and Mathematics in Electrical and Electronic Engineering, vol. 30, no. 2, pp. 671-685, 2011.

[22] E. Afjei and H. Torkaman, "Investigation of Electromagnetic Characteristics in External Rotor SRM under Dynamic Eccentricity Fault," International Review of Electrical Engineering, vol. 6, no. 3, pp. 1257-1263, 2011.

[23] H. Torkaman and E. Afjei, "Hybrid Method of Obtaining Degrees of Freedom for Radial Airgap Length in SRM under Normal and Faulty Conditions Based on Magnetiostatic Model," Progress In Electromagnetics Research, PIER, vol. 100, pp. 37-54, 2010.

[24] M. N. Anwar, I. Husain, and A. Radun, "A Comprehensive Design Methodology for Switched Reluctance Machines," IEEE Transactions on Industry Applications, vol. 36, no. 6, pp. 1684-1692, 2001.

[25] Magnet CAD package, "User manual," Infolytica Corporation Ltd., 2007.

# 2011 INSTITUTIONAL MEMBERS

DTIC-OCP LIBRARY
8725 John J. Kingman Rd, Ste 0944
Fort Belvoir, VA 22060-6218

AUSTRALIAN DEFENCE LIBRARY
Northcott Drive
Canberra, A.C.T. 2600 Australia

BEIJING BOOK CO, INC
701 E Linden Avenue
Linden, NJ 07036-2495

DARTMOUTH COLLEGE
6025 Baker/Berry Library
Hanover, NH 03755-3560

DSTO EDINBURGH
AU/33851-AP, PO Box 830470
Birmingham, AL 35283

SIMEON J. EARL – BAE SYSTEMS
W432A, Warton Aerodome
Preston, Lancs., UK PR4 1AX

ENGINEERING INFORMATION, INC
PO Box 543
Amsterdam, Netherlands 1000 Am

ETSE TELECOMUNICACION
Biblioteca, Campus Lagoas
Vigo, 36200 Spain

GA INSTITUTE OF TECHNOLOGY
EBS-Lib Mail code 0900
74 Cherry Street
Atlanta, GA 30332

TIMOTHY HOLZHEIMER
Raytheon
PO Box 1044
Rockwall, TX 75087

HRL LABS, RESEARCH LIBRARY
3011 Malibu Canyon
Malibu, CA 90265

IEE INSPEC
Michael Faraday House
6 Hills Way
Stevenage, Herts UK SG1 2AY

INSTITUTE FOR SCIENTIFIC INFO.
Publication Processing Dept.
3501 Market St.
Philadelphia, PA 19104-3302

LIBRARY – DRDC OTTAWA
3701 Carling Avenue
Ottawa, Ontario, Canada K1A OZ4

LIBRARY of CONGRESS
Reg. Of Copyrights
Attn: 407 Deposits
Washington DC, 20559

LINDA HALL LIBRARY
5109 Cherry Street
Kansas City, MO 64110-2498

MISSOURI S&T
400 W 14th Street
Rolla, MO 56409

MIT LINCOLN LABORATORY
Periodicals Library
244 Wood Street
Lexington, MA 02420

NATIONAL CHI NAN UNIVERSITY
Lily Journal & Book Co, Ltd
20920 Glenbrook Drive
Walnut, CA 91789-3809

JOHN NORGARD
UCCS
20340 Pine Shadow Drive
Colorado Springs, CO 80908

OSAMA MOHAMMED
Florida International University
10555 W Flagler Street
Miami, FL 33174

NAVAL POSTGRADUATE SCHOOL
Attn:J. Rozdal/411 Dyer Rd./ Rm 111
Monterey, CA 93943-5101

NDL KAGAKU
C/0 KWE-ACCESS
PO Box 300613 (JFK A/P)
Jamaica, NY 11430-0613

OVIEDO LIBRARY
PO BOX 830679
Birmingham, AL 35283

DAVID PAULSEN
E3Compliance
1523 North Joe Wilson Road
Cedr Hill, TX 75104-1437

PENN STATE UNIVERSITY
126 Paterno Library
University Park, PA 16802-1808

DAVID J. PINION
1122 E Pike Street #1217
SEATTLE, WA 98122

KATHERINE SIAKAVARA
Gymnasiou 8
Thessaloniki, Greece 55236

SWETS INFORMATION SERVICES
160 Ninth Avenue, Suite A
Runnemede, NJ 08078

YUTAKA TANGE
Maizuru Natl College of Technology
234 Shiroya
Maizuru, Kyoto, Japan 625-8511

TIB & UNIV. BIB. HANNOVER
DE/5100/G1/0001
Welfengarten 1B
Hannover, Germany 30167

UEKAE
PO Box 830470
Birmingham, AL 35283

UNIV OF CENTRAL FLORIDA
4000 Central Florida Boulevard
Orlando, FL 32816-8005

UNIVERSITY OF COLORADO
1720 Pleasant Street, 184 UCB
Boulder, CO 80309-0184

UNIVERSITY OF KANSAS – WATSON
1425 Jayhawk Blvd 210S
Lawrence, KS 66045-7594

UNIVERSITY OF MISSISSIPPI
JD Williams Library
University, MS 38677-1848

UNIVERSITY LIBRARY/HKUST
Clear Water Bay Road
Kowloon, Honk Kong

CHUAN CHENG WANG
8F, No. 31, Lane 546
MingCheng 2nd Road, Zuoying Dist
Kaoshiung City, Taiwan 813

THOMAS WEILAND
TU Darmstadt
Schlossgartenstrasse 8
Darmstadt, Hessen, Germany 64289

STEVEN WEISS
US Army Research Lab
2800 Powder Mill Road
Adelphi, MD 20783

YOSHIHIDE YAMADA
NATIONAL DEFENSE ACADEMY
1-10-20 Hashirimizu
Yokosuka, Kanagawa,
Japan 239-8686

**APPLIED COMPUTATIONAL ELECTROMAGNETICS SOCIETY JOURNAL**
**http://aces.ee.olemiss.edu**

## INFORMATION FOR AUTHORS

### PUBLICATION CRITERIA

Each paper is required to manifest some relation to applied computational electromagnetics. **Papers may address general issues in applied computational electromagnetics, or they may focus on specific applications, techniques, codes, or computational issues.** While the following list is not exhaustive, each paper will generally relate to at least one of these areas:

1. **Code validation.** This is done using internal checks or experimental, analytical or other computational data. Measured data of potential utility to code validation efforts will also be considered for publication.

2. **Code performance analysis.** This usually involves identification of numerical accuracy or other limitations, solution convergence, numerical and physical modeling error, and parameter tradeoffs. However, it is also permissible to address issues such as ease-of-use, set-up time, run time, special outputs, or other special features.

3. **Computational studies of basic physics.** This involves using a code, algorithm, or computational technique to simulate reality in such a way that better, or new physical insight or understanding, is achieved.

4. **New computational techniques** or new applications for existing computational techniques or codes.

5. **"Tricks of the trade"** in selecting and applying codes and techniques.

6. **New codes, algorithms, code enhancement, and code fixes.** This category is self-explanatory, but includes significant changes to existing codes, such as applicability extensions, algorithm optimization, problem correction, limitation removal, or other performance improvement. **Note: Code (or algorithm) capability descriptions are not acceptable, unless they contain sufficient technical material to justify consideration.**

7. **Code input/output issues.** This normally involves innovations in input (such as input geometry standardization, automatic mesh generation, or computer-aided design) or in output (whether it be tabular, graphical, statistical, Fourier-transformed, or otherwise signal-processed). Material dealing with input/output database management, output interpretation, or other input/output issues will also be considered for publication.

8. **Computer hardware issues.** This is the category for analysis of hardware capabilities and limitations of various types of electromagnetics computational requirements. Vector and parallel computational techniques and implementation are of particular interest.

Applications of interest include, but are not limited to, antennas (and their electromagnetic environments), networks, static fields, radar cross section, inverse scattering, shielding, radiation hazards, biological effects, biomedical applications, electromagnetic pulse (EMP), electromagnetic interference (EMI), electromagnetic compatibility (EMC), power transmission, charge transport, dielectric, magnetic and nonlinear materials, microwave components, MEMS, RFID, and MMIC technologies, remote sensing and geometrical and physical optics, radar and communications systems, sensors, fiber optics, plasmas, particle accelerators, generators and motors, electromagnetic wave propagation, non-destructive evaluation, eddy currents, and inverse scattering.

Techniques of interest include but not limited to frequency-domain and time-domain techniques, integral equation and differential equation techniques, diffraction theories, physical and geometrical optics, method of moments, finite differences and finite element techniques, transmission line method, modal expansions, perturbation methods, and hybrid methods.

Where possible and appropriate, authors are required to provide statements of quantitative accuracy for measured and/or computed data. This issue is discussed in "Accuracy & Publication: Requiring, quantitative accuracy statements to accompany data," by E. K. Miller, *ACES Newsletter*, Vol. 9, No. 3, pp. 23-29, 1994, ISBN 1056-9170.

### SUBMITTAL PROCEDURE

All submissions should be uploaded to ACES server through ACES web site (http://aces.ee.olemiss.edu) by using the upload button, journal section. Only pdf files are accepted for submission. The file size should not be larger than 5MB, otherwise permission from the Editor-in-Chief should be obtained first. Automated acknowledgment of the electronic submission, after the upload process is successfully completed, will be sent to the corresponding author only. It is the responsibility of the corresponding author to keep the remaining authors, if applicable, informed. Email submission is not accepted and will not be processed.

### EDITORIAL REVIEW

**In order to ensure an appropriate level of quality control**, papers are peer reviewed. They are reviewed both for technical correctness and for adherence to the listed guidelines regarding information content and format.

### PAPER FORMAT

Only camera-ready electronic files are accepted for publication. The term **"camera-ready" means that the material is neat, legible, reproducible, and in accordance with the final version format listed below.**

The following requirements are in effect for the final version of an ACES Journal paper:

1. The paper title should not be placed on a separate page.

The title, author(s), abstract, and (space permitting) beginning of the paper itself should all be on the first page. The title, author(s), and author affiliations should be centered (center-justified) on the first page. The title should be of font size 16 and bolded, the author names should be of font size 12 and bolded, and the author affiliation should be of font size 12 (regular font, neither italic nor bolded).

2. An abstract is required. The abstract should be a brief summary of the work described in the paper. It should state the computer codes, computational techniques, and applications discussed in the paper (as applicable) and should otherwise be usable by technical abstracting and indexing services. The word "Abstract" has to be placed at the left margin of the paper, and should be bolded and italic. It also should be followed by a hyphen (—) with the main text of the abstract starting on the same line.

3. All section titles have to be centered and all the title letters should be written in caps. The section titles need to be numbered using roman numbering (I. II. ….)

4. Either British English or American English spellings may be used, provided that each word is spelled consistently throughout the paper.

5. Internal consistency of references format should be maintained. As a guideline for authors, we recommend that references be given using numerical numbering in the body of the paper (with numerical listing of all references at the end of the paper). The first letter of the authors' first name should be listed followed by a period, which in turn, followed by the authors' complete last name. Use a coma (,) to separate between the authors' names. Titles of papers or articles should be in quotation marks (" "), followed by the title of journal, which should be in italic font. The journal volume (vol.), issue number (no.), page numbering (pp.), month and year of publication should come after the journal title in the sequence listed here.

6. Internal consistency shall also be maintained for other elements of style, such as equation numbering. Equation numbers should be placed in parentheses at the right column margin. All symbols in any equation have to be defined before the equation appears or right immediately following the equation.

7. The use of SI units is strongly encouraged. English units may be used as secondary units (in parentheses).

8. Figures and tables should be formatted appropriately (centered within the column, side-by-side, etc.) on the page such that the presented data appears close to and after it is being referenced in the text. When including figures and tables, all care should be taken so that they will appear appropriately when printed in black and white. For better visibility of paper on computer screen, it is good to make color figures with different line styles for figures with multiple curves. Colors should also be tested to insure their ability to be distinguished after black and white printing. Avoid the use of large symbols with curves in a figure. It is always better to use different line styles such as solid, dotted, dashed, etc.

9. A figure caption should be located directly beneath the corresponding figure, and should be fully justified.

10. The intent and meaning of all text must be clear. For authors who are not masters of the English language, the ACES Editorial Staff will provide assistance with grammar (subject to clarity of intent and meaning). However, this may delay the scheduled publication date.

11. Unused space should be minimized. Sections and subsections should not normally begin on a new page.

ACES reserves the right to edit any uploaded material, however, this is not generally done. It is the author(s) responsibility to provide acceptable camera-ready files in pdf and MSWord formats. Incompatible or incomplete files will not be processed for publication, and authors will be requested to re-upload a revised acceptable version.

**COPYRIGHTS AND RELEASES**

Each primary author must execute the online copyright form and obtain a release from his/her organization vesting the copyright with ACES. Both the author(s) and affiliated organization(s) are allowed to use the copyrighted material freely for their own private purposes.

Permission is granted to quote short passages and reproduce figures and tables from and ACES Journal issue provided the source is cited. Copies of ACES Journal articles may be made in accordance with usage permitted by Sections 107 or 108 of the U.S. Copyright Law. This consent does not extend to other kinds of copying, such as for general distribution, for advertising or promotional purposes, for creating new collective works, or for resale. The reproduction of multiple copies and the use of articles or extracts for commercial purposes require the consent of the author and specific permission from ACES. Institutional members are allowed to copy any ACES Journal issue for their internal distribution only.

**PUBLICATION CHARGES**

All authors are allowed for 8 printed pages per paper without charge. Mandatory page charges of $75 a page apply to all pages in excess of 8 printed pages. Authors are entitled to one, free of charge, copy of the printed journal issue in which their paper was published. Additional reprints are available for $ 50. Requests for additional re-prints should be submitted to the managing editor or ACES Secretary.

Corresponding author is required to complete the online form for the over page charge payment right after the initial acceptance of the paper is conveyed to the corresponding author by email.

**ACES Journal is abstracted in INSPEC, in Engineering Index, DTIC, Science Citation Index Expanded, the Research Alert, and to Current Contents/Engineering, Computing & Technology.**